2374 S

STELLINGEN

behorende bij het proefschrift

Geomaterial Models and Numerical Analysis of Softening

R.B.J. Brinkgreve, Delft, mei 1994

1. De beschrijving van niet-lineair elastisch materiaalgedrag met behulp van een elastische potentiaal, waarin de secant stijfheid een machtsfunktie is van het spanningsniveau, degenereert in het algemeen als de exponent gelijk aan 1 wordt genomen, zoals o.a. te zien is in de modellen van Vermeer (1980) en Molenkamp (1988). Het model beschreven in paragraaf 2.4 van dit proefschrift, dat nauw aansluit bij het model van Molenkamp, vormt een uitzondering op deze regel.

   Vermeer P.A (1980), Formulation and Analysis of Sand Deformation Problems. Proefschrift. Technische Universiteit Delft.

   Molenkamp F. (1988), A simple model for isotropic non-linear elasticity of frictional materials. Int. J. Num. Anal. Meth. Geomech. Vol. 12, pp. 467-475.

2. Bij numerieke analyses van geotechnische constructies leidt het gebruik van gecompliceerde materiaalmodellen die het gedrag van grond zeer goed beschrijven niet altijd tot betere resultaten dan het gebruik van eenvoudige modellen die het grondgedrag minder goed benaderen. De analyse met een gecompliceerd model is alleen effectief als er grondonderzoek van bijpassende omvang en precisie wordt uitgevoerd.

3. Bij toepassing van het Modified Cam-Clay model wordt de helling van de Critical State Line M in het algemeen bepaald op basis van de inwendige wrijving van het te modelleren materiaal. Een dergelijke keuze van M leidt bij simulaties van ééndimensionale samendrukking tot een te hoge coëfficiënt van laterale gronddruk.

4. Met name in situaties waarin het spanningsverloop in plaats of tijd sterk van karakter verschilt, of in het geval van pseudo-ééndimensionale samendrukking, leidt het gebruik van cap-hardening modellen tot een betere voorspelling van deformaties dan elastisch perfect-plastische modellen.

5. In de numerieke mechanica heeft de volledige Newton-Raphson methode voor het oplossen van een stelsel van niet-lineaire vergelijkingen op basis van een tangentstijfheidsmatrix een aanzienlijk kleinere convergentieradius dan een gemodificeerde Newton-Raphson methode op basis van een elastische stijfheidsmatrix. Het gebruik van laatstgenoemde methode verdient derhalve de voorkeur bij praktische toepassingen.

   Stricklin J.A., Haisler W.E. (1977), Formulations and solution procedures for nonlinear structural analysis. Computers & Structures, Vol. 7, pp. 125-136.

6. Het toepassen van conventionele softening modellen in numerieke analyses leidt niet alleen tot mesh-afhankelijke resultaten, maar ook tot slechte convergentie van het evenwicht-iteratieproces.

7. De gedachte dat een non-local formulering van constitutieve relaties zich niet leent voor wiskundige bewerkingen en analytische oplossingen, is onjuist.

   Hoofdstuk 8 van dit proefschrift.

8. Bij het verrichten van wetenschappelijk onderzoek is het noodzakelijk om de praktische toepasbaarheid van de onderzoekresultaten voor ogen te houden en vroegtijdig aandacht te besteden aan de operationalisatie.

9. Het psychologische effect dat uitgaat van veiligheid-verhogende technieken in automobielen, zoals ABS en airbag, leidt bij sommige automobilisten tot een verhoging van de gemiddelde rijsnelheid, waardoor het beoogde veiligheidseffect wordt geneutraliseerd.

10. Met name in de ochtendspits vertoont de snelheid van het verkeer op een continu trajekt van een autosnelweg veelal lokaal een sterke terugval. Verreweg de belangrijkste oorzaak van dit lokalizatie-fenomeen is een in-het-oog-springende aktiviteit op de aanliggende vluchtstrook. De oplossing hiervan dient gezocht te worden in de sfeer van verkeersregularizatie.

11. De gemiddelde bezetting van een rijdende personenauto bedraagt op dit moment 1.63 personen. In de ochtendspits is de bezetting echter beduidend lager. Het optimaliseren van de vervoerscapaciteit door carpooling is derhalve een zeer efficiënte oplossing van het fileprobleem, welke is te prefereren boven infrastructurele maatregelen.

    Bron: CBS, februari 1994.

12. Het roken van tabaksartikelen zou moeten worden beperkt tot speciale daarvoor aangewezen hermetisch afgesloten ruimten.

TR diss
2374

GEOMATERIAL MODELS AND NUMERICAL ANALYSIS OF SOFTENING

GEOMATERIAL MODELS AND NUMERICAL ANALYSIS OF SOFTENING

PROEFSCHRIFT

ter verkrijging van de graad van doctor
aan de Technische Universiteit Delft,
op gezag van de Rector Magnificus Prof.ir. K.F. Wakker,
in het openbaar te verdedigen ten overstaan van een commissie,
door het College van Dekanen aangewezen,
op dinsdag 24 mei 1994 te 13.30 uur

door

Ronald Bastiaan Johan BRINKGREVE

civiel ingenieur
geboren te Doetinchem

Dit proefschrift is goedgekeurd door de promotoren:

Prof.dr.ir. A. Verruijt
Prof.dr.ir. P.A. Vermeer

CIP-GEGEVENS KONINKLIJKE BIBLIOTHEEK, DEN HAAG

Brinkgreve, Ronald Bastiaan Johan

Geomaterial models and numerical analysis of softening /
Ronald Bastiaan Johan Brinkgreve. - [S.l. : s.n.]. - Ill.
Thesis Technische Universiteit Delft. - With ref. - With
summary in Dutch.
ISBN 90-9007034-6
NUGI 816
Subject headings: geotechnics.

Omslagontwerp: Peter van der Horst

ACKNOWLEDGEMENTS

The research described in this thesis has been carried out at the Geotechnical Laboratory of the Faculty of Civil Engineering of Delft University of Technology, under the supervision of Prof. P.A. Vermeer.

I gratefully acknowledge the stimulating discussions with Prof. Vermeer and other collegues. Most models and numerical procedures described in this thesis were implemented in the Plaxis finite element code. I like to express my appreciation for the fruitful cooperation within the Plaxis Research and Development Team. Moreover, I enjoyed the pleasant working atmosphere in the Geotechnical Laboratory.

The research was financially supported by the Technology Foundation (STW), and co-sponsored by the Road and Hydraulic Engineering Division (DWW) of the Dutch Ministry of Transport, Public Works and Water Management (Rijkswaterstaat) and by Shell Research, Rijswijk (KSEPL). This support is gratefully acknowledged.

CONTENTS

1. INTRODUCTION 1
   - 1.1 Aims and scope of this research project 1
   - 1.2 Outline of the thesis 2

2. ELASTIC AND PSEUDO-ELASTIC SOIL MODELS 5
   - 2.1 Preliminaries of constitutive modelling 5
   - 2.2 Pseudo-elastic power law model 8
   - 2.3 Elastic power law model by Vermeer 9
   - 2.4 Elastic power law model by Molenkamp 15
   - 2.5 Hyperbolic Duncan-Chang model 19

3. ELASTIC PERFECTLY-PLASTIC SOIL MODELS 23
   - 3.1 The Drucker-Prager model 23
   - 3.2 The Mohr-Coulomb model 26
   - 3.3 Improvements to the Mohr-Coulomb model 29
   - 3.4 Matching Drucker-Prager and Mohr-Coulomb for plane strain 33

4. HARDENING PLASTICITY 37
   - 4.1 The Modified Cam-Clay model 37
   - 4.2 The coefficient of later earth pressure for normally consolidated soil 42
   - 4.3 The Plaxis Cap model 46
   - 4.4 Comparison of tangential shear moduli for different stress paths 49
   - 4.5 Overconsolidated stress states 51

5. FORMULATION AND SOLUTION OF THE BOUNDARY VALUE PROBLEM 53
   - 5.1 General equations of continuum theory 53
   - 5.2 Finite element discretization 55
   - 5.3 Implicit integration of differential plasticity models 56
   - 5.4 Solving non-linear stress-strain relations 58
     - 5.4.1 The non-linear elastic part 59
     - 5.4.2 The cap hardening 60
     - 5.4.3 The point of combined yielding 67
   - 5.5 Global iterative procedures 70
   - Appendix 73

6. APPLICATIONS OF THE PLAXIS CAP MODEL 75
- 6.1 Plate loading test 75
- 6.2 Almere trial embankment 80
- 6.3 Brienenoord road widening project 85

7. LOCAL SOFTENING PLASTICITY 91
- 7.1 The Advanced Cam-Clay model 92
- 7.2 A Drucker-Prager softening model 94
- 7.3 A Von Mises softening model 95
- 7.4 Breakdown of the classical approach of local softening plasticity 97
  - 7.4.1 Biaxial test problem 97
  - 7.4.2 Steep embankment slope 101
- 7.5 Conclusions on local softening plasticity 104

8. REGULARIZATION TECHNIQUES FOR SOFTENING MODELS 105
- 8.1 Overview of existing regularization techniques 105
- 8.2 The existing non-local softening plasticity model 109
- 8.3 A modified non-local softening plasticity model 111
- 8.4 Analytical solution for the modified non-local model 113
- 8.5 Discussion of the analytical solution 116
- 8.6 Comparison with the strain-gradient theory 117
- 8.7 One-dimensional numerical implementation 118
- 8.8 Numerical versus analytical solution 121

9. IMPLEMENTATION OF REGULARIZATION TECHNIQUE 125
- 9.1 A Drucker-Prager non-local softening model 125
- 9.2 Numerical integration and implementation of the non-local model 127
- 9.3 Shear-banding in purely cohesive material 129
- 9.4 Shear-banding in rock-like material 131
- 9.5 Softening scaling to improve practical applicability 134
- 9.6 Non-local softening and scaling in slope stability problem 136

10. CONCLUSIONS AND RECOMMENDATIONS 139

REFERENCES 143

SYMBOLS AND SIGN CONVENTION 149

SUMMARY IN DUTCH (Samenvatting) 151

1 INTRODUCTION

Since 1960, researchers have been working on constitutive models for geomaterials, i.e. soil and rock. In later years such models have been applied in finite element codes, in particular the simple elastoplastic Mohr-Coulomb model. More refined models exist, but they are not easily applied in practical geotechnical engineering. Even well-known Cam-Clay type models are, as yet, not generally applied for clays, and are subject to criticism. From a practical point of view, the criticism concerns among other things the prediction of lateral stresses in soil layers. From a theoretical point of view, the quite general use of non-conservative elasticity laws is not justified. In fact, a proper potential for the elastic strain-energy is missing. This study is among other things aimed at improving this situation, and some improvements of existing constitutive models are proposed.

Another quite different part of this study concerns a new topic of geomechanics, namely non-local material softening. Dense clays and rock show material softening, i.e. negativeness of the second-order work, but classical softening models lead to ill-posed formulations. Numerical calculations with such models produce unreliable results. Recently, some researchers have put forward new ideas for arriving at well-posedness of boundary value problems. Stimulated by some pioneering work in this field, a so-called non-local approach is put into operation.

1.1 Aims and scope of this research project

In this study it is aimed to analyse constitutive models for geomaterials from the viewpoint of practical applicability and to formulate a robust method for the numerical analysis of softening behaviour.

In order to describe the behaviour of geomaterials in a constitutive model, a distinction can be made between elasticity, perfect-plasticity, hardening and softening behaviour. A very detailed geomaterial model will contain all these aspects, but simpler models can be formulated by adopting only elasticity or by simple combinations of elasticity and plasticity. Such models are reviewed with the aim of analysing shortcomings and limitations and of finding improvements.

On considering elasticity, it is clear that non-linearity is required, but for elastic clay behaviour in particular, proper strain-energy functions would appear to be missing. For this reason, attention will be focused on strain-energy functions. Another topic in this study is the use of hardening plasticity, in particular cap-hardening, of which the Modified Cam-Clay model is a well-known example. Although Cam-Clay type models are, in principle, appropriate for practical applications, there is the shortcoming that these models do not give the correct lateral stress in one-dimensional compression. Therefore this will be studied here. A proper numerical integration of the Cam-Clay model was recently proposed by Borja & Lee (1990), but the numerical treatment of yield vertices has not yet obtained full attention. Yield vertices become important when implementing, for instance, the Advanced Cam-Clay model, as described by Atkinson & Bransby (1978). In this model, a yield vertex is present at the intersection of the Hvorslev surface and the yield cap. For this reason the topic of numerical modelling will be given attention.

Cam-Clay models do not only involve hardening plasticity, but softening plasticity as well. Unfortunately, softening models cannot be used straightforwardly in numerical simulations because of mesh-sensitivity. Near failure, all deformation tends to concentrate in the narrowest shear-band that can be resolved by the mesh, i.e. a shear-band thickness of about one element. Hence, upon mesh refinement, shear-bands become narrower and computed load-displacement curves will change considerably. From an engineering point of view, element size dependency is solved by using a technique as proposed by Pietruszczak & Mroz (1981), in which the softening is scaled according to the element size and the desired shear-band thickness. However, an influence of mesh alignment remains. Moreover, scaling techniques as proposed by Pietruszczak & Mroz do not solve the problem of numerical instability, as associated with classical softening models. New fundamental methods, which are called regularizations, were introduced to solve the problems related to the use of softening models. One type of regularization involves non-local theories, for which pioneering work has been done by Bazant et al. (1984). Another regularization, which can be seen as a derivation from non-local theories, is the strain-gradient theory. Extensive contributions in this area were recently made by De Borst and co-workers (1991, 1992). In 1986, Mühlhaus was among the first researchers who successfully applied the old Cosserat theory as a regularization for shear-banding problems. In the field of complex regularization methods, which are generally not easy to apply in practice, this study is aimed to develop one of the basic theories in order to obtain a robust regularization method with a high degree of practical applicability.

1.2 Outline of the thesis

As mentioned above, this thesis can be divided into two parts. The first part is on well-known fields of geotechnical research, i.e. constitutive modelling and non-linear finite element analyses. The second part concerns a new topic of geomechanics, namely, the non-local approach to the modelling of softening phenomena.

Chapter 2 deals with elastic and pseudo-elastic soil models. An analysis is carried out into the extent to which some non-linear models can be used to simulate the (elastic) behaviour of geomaterials. Special attention is given here to strain-energy functions. The complementary strain-energy function as presented by Molenkamp (1988) is extended to account for a linear relationship between stiffnesses and stress level. Chapter 3 gives a description of perfectly-plastic models. Aspects of vertex yielding are discussed in relation to the Mohr-Coulomb model and simple extensions of this model are proposed for practical applications. In plane strain situations, an elaboration is given as to how Drucker-Prager model parameters for dilatant materials should be related to well-known soil properties in order to arrive at the more accurate Mohr-Coulomb failure level. Chapter 4 deals with a particular form of hardening plasticity: Cap hardening. As an example of cap hardening, the Modified Cam-Clay model is described. For this model the relation is analysed between model parameters and the development of lateral stresses in one-dimensional compression and it is concluded that K_0-values tend to be overpredicted. In order to account for this shortcoming of the Modified Cam-Clay model, a slightly different model is introduced, named the Plaxis Cap model. An analysis is made of how the stiffness behaviour in cap models varies for different stress paths. Chapter 5 contains the general equations for the solution of the boundary value problem by means of the finite element method. A detailed description is given of various aspects of stress integration with respect to time, including the numerical treatment of yield vertices in the Plaxis Cap model. In Chapter 6 this model is used for some practical applications. In each application a comparison is made between the new model and a well known perfectly-plastic model. This is done in order to investigate under which conditions the use of hardening plasticity is required.

Chapter 7 deals with softening plasticity. After some softening models have been described according to the classical (local) plasticity theory, it is shown that such models suffer from specific problems when used in numerical applications. Apart from mesh-dependency, as reported by several other researchers, the phenomenon of poor convergence is discussed, which was not mentioned in former studies. Chapter 8 gives a description of so-called regularization techniques, which were developed to overcome the numerical problems related to the use of softening models. A new non-local regularization method is introduced, named the Modified Non-local Method. In one-dimensional form, this model allows for an analytical solution for necking in a tension bar. The analytical solution proves the effectiveness of the current non-local method and, at the same time, the non-effectiveness of existing non-local models for one-dimensional applications. Numerical calculations are performed in order to validate the new theory. In Chapter 9 the modified non-local method is extended to general three-dimensional situations and applied to previously formulated softening models. Verification of proper functioning is done by a recalculation of the numerical applications of Chapter 7. A practical solution is presented to avoid the use of extremely small elements.

The final chapter, Chapter 10, contains the general conclusions that were drawn from the work described in this thesis, and some recommendations and topics for further research are proposed.

2 ELASTIC AND PSEUDO-ELASTIC SOIL MODELS

In this chapter a selection of elastic and pseudo-elastic models is considered. Elasticity is associated with reversibility of strains upon unloading. A truly elastic model, or hyper-elastic model, is defined as a model that does not allow for generation or dissipation of energy in closed stress loops. Such models involve a so-called *strain-energy function*, as for instance considered by Fung (1965). Pseudo-elastic models are models based on elasticity theory, but they do not satisfy the basic criterion of reversibility. Moreover, the pseudo-elastic models will most generally not satisfy the above energy criterion. The latter type of models is more interesting for practical applications rather than for scientific purposes. However, because the aim of this study is to form a balance between science and practical applicability, both types are considered here. The beginning of this chapter is devoted to some preliminary relations, which are used throughout the thesis.

2.1 Preliminaries of constitutive modelling

In the relationship between rates of stress and rates of strain, as considered in this study, restriction is made to either a truly linear relation or a multi-linear relation. A truly linear relation is, for example, obtained for truly elastic materials. For elastoplastic models the relationship is usually bilinear to distinguish between loading and unloading, but other forms of multi-linearity exist (Koiter, 1953). Another bilinear relationship is implied by the pseudo-elastic Duncan-Chang model (Duncan & Chang, 1970) as considered in Section 2.5. The multi-linear relationship between rates of stress and rates of strain is written in the form:

$$\underline{\dot{\varepsilon}} = \underline{\underline{C}}\,\underline{\dot{\sigma}} \qquad \text{or} \qquad \underline{\dot{\sigma}} = \underline{\underline{M}}\,\underline{\dot{\varepsilon}} \tag{2.1}$$

In this equation the stress and strain tensor are written in vector notation, which involves all the six Cartesian components:

$$\underline{\varepsilon} = (\varepsilon_{xx}\,,\, \varepsilon_{yy}\,,\, \varepsilon_{zz}\,,\, \gamma_{xy}\,,\, \gamma_{yz}\,,\, \gamma_{zx})^T \tag{2.2a}$$

$$\underline{\sigma} = (\sigma_{xx}\,,\, \sigma_{yy}\,,\, \sigma_{zz}\,,\, \sigma_{xy}\,,\, \sigma_{yz}\,,\, \sigma_{zx})^T \tag{2.2b}$$

Positive normal stresses are considered to represent tension, whereas negative normal stresses relate to pressure. Similarly, positive normal strains relate to extension whereas negative normal strains relate to compression.

It is often useful to transform the Cartesian stress components into principal stresses. For the general three-dimensional case, three principal stresses $(\sigma_1 , \sigma_2 , \sigma_3)$ exist, which correspond to the three principal stress directions. The orthogonal basis formed by the three principal stress axes is referred to as the principal stress space. States of stress can be plotted as points in the principal stress space and changes of stress can be represented by stress paths.

Another way of representing stresses is by means of the invariants p, q and θ, defined as:

$$p = -\frac{1}{3} (\sigma_1 + \sigma_2 + \sigma_3) \tag{2.3a}$$

$$q = \sqrt{\frac{1}{2} \left((\sigma_1 - \sigma_2)^2 + (\sigma_2 - \sigma_3)^2 + (\sigma_3 - \sigma_1)^2 \right)} \tag{2.3b}$$

$$\theta = \frac{1}{3} \arcsin \left[-\frac{9}{2} \frac{(\sigma_1 + p)(\sigma_2 + p)(\sigma_3 + p)}{q^3} \right] \tag{2.3c}$$

In this form, p is the isotropic stress or mean stress, q is the equivalent shear stress, and θ is referred to as Lode's angle. The equivalent shear stress is a composition of deviatoric stress components. Under triaxial stress conditions where $\sigma_2 = \sigma_3$, q is just the principal stress difference: $q = | \sigma_1 - \sigma_3 |$.

Strains are often presented as principle strains $(\varepsilon_1 , \varepsilon_2 , \varepsilon_3)$ as well. Other strain measures that are frequently used in this study are the invariants ε_v and ε_s, defined respectively as:

$$\varepsilon_v = -(\varepsilon_1 + \varepsilon_2 + \varepsilon_3) \tag{2.4a}$$

$$\varepsilon_s = \sqrt{\frac{2}{9} \left((\varepsilon_1 - \varepsilon_2)^2 + (\varepsilon_2 - \varepsilon_3)^2 + (\varepsilon_3 - \varepsilon_1)^2 \right)} \tag{2.4b}$$

The volumetric strain ε_v is considered positive for compression. The equivalent shear strain ε_s is under triaxial strain conditions where $\varepsilon_2 = \varepsilon_3$, equal to two thirds of the principle strain difference: $\varepsilon_s = {}^2/_3 \ | \varepsilon_1 - \varepsilon_3 |$.

The matrix $\underline{\underline{C}}$ in Equation 2.1 is the material compliance matrix and $\underline{\underline{M}}$ is the material stiffness matrix. The coefficients of these matrices will generally be functions of the actual state of stress and strain to account for non-linear material behaviour. For elastoplastic models, the matrices $\underline{\underline{C}}$ and $\underline{\underline{M}}$ also depend on the increments of stress and strain. Indeed, in classical plasticity as, for instance, considered by Hill (1950), a distinction is made between loading and unloading. For loading, $\underline{\underline{M}}$ is an elastoplastic stiffness matrix and for unloading $\underline{\underline{M}}$ is a much stiffer elasticity matrix. Hence, the differential equation is not linear as suggested by Equation 2.1, but the relationship is bilinear. A further step in this direction is to distinguish between different types of loading and thus different types of plasticity (Koiter, 1953). In this manner one obtains a multi-linear differential equation.

The simplest form of the material stiffness matrix $\underline{\underline{M}}$ in Equation 2.1 is that given by the generalized form of Hooke's law, which represents isotropic linear elastic behaviour. Only two elastic parameters are required: In engineering practice mostly taken as Young's modulus E, and Poisson's ratio ν.

$$\begin{bmatrix} \dot\sigma_{xx} \\ \dot\sigma_{yy} \\ \dot\sigma_{zz} \\ \dot\sigma_{xy} \\ \dot\sigma_{yz} \\ \dot\sigma_{zx} \end{bmatrix} = \frac{E}{(1+\nu)(1-2\nu)} \begin{bmatrix} 1-\nu & \nu & \nu & 0 & 0 & 0 \\ \nu & 1-\nu & \nu & 0 & 0 & 0 \\ \nu & \nu & 1-\nu & 0 & 0 & 0 \\ 0 & 0 & 0 & \tfrac12-\nu & 0 & 0 \\ 0 & 0 & 0 & 0 & \tfrac12-\nu & 0 \\ 0 & 0 & 0 & 0 & 0 & \tfrac12-\nu \end{bmatrix} \begin{bmatrix} \dot\varepsilon_{xx} \\ \dot\varepsilon_{yy} \\ \dot\varepsilon_{zz} \\ \dot\gamma_{xy} \\ \dot\gamma_{yz} \\ \dot\gamma_{zx} \end{bmatrix} \tag{2.5}$$

The elastic material stiffness matrix according to Hooke's law is referred to as $\underline{\underline{D}}^e$. The equivalence of Equation 2.5 in terms of the invariants of stress and strain, as defined above, can simply be formulated as:

$$\begin{bmatrix} \dot p \\ \dot q \end{bmatrix} = \begin{bmatrix} K & 0 \\ 0 & 3G \end{bmatrix} \begin{bmatrix} \dot\varepsilon_v \\ \dot\varepsilon_s \end{bmatrix} \tag{2.6}$$

in which K is the bulk modulus and G is the shear modulus. In Hooke's law K, G and E are interchangeable:

$$K = \frac{E}{3\,(1-2\,\nu)} \qquad\qquad G = \frac{E}{2\,(1+\nu)} \tag{2.7}$$

Because of the non-linear soil behaviour it is difficult to choose a proper stiffness modulus in this model. In fact, the stiffness changes as a function of stress and strain. Moreover, a clear distinction should be made between drained conditions where parameters (E', ν') relate to effective stresses $\underline{\sigma}'$, and undrained conditions where parameters (E_u, ν_u) relate to total stresses $\underline{\sigma}$. The shear modulus G is unaffected by such conditions. It simply relates both sets of parameters in the following way:

$$\frac{E_u}{1+\nu_u} = 2\,G_u \equiv 2\,G' = \frac{E'}{1+\nu'} \tag{2.8}$$

Hence, $G_u = G'$. This is one of the reasons why it is preferred to use the shear modulus as a model parameter for soil rather than Young's modulus. In the remainder of this thesis the apostrophe (') will conveniently be omitted when considering effective model parameters and effective stresses.

2.2 Pseudo-elastic power law model

In addition to Terzaghi's logarithmic compression law (Terzaghi, 1925) it was Ohde (1939) who formulated the compressibility of materials in a general form by defining the stiffness modulus as a power function of the "load" p. In a later period, researchers such as Schultze and Moussa (1961) showed, by experimental studies, that a tangent modulus of one-dimensional compression E_{oed} for dry sandy materials can be written as a power function of the stress p:

$$E_{oed} = \frac{1}{m_v} = \alpha\, p^{m} \tag{2.9}$$

where α and m are model parameters which can be obtained from oedometer tests by plotting the logarithm of the axial stress against the logarithm of the axial strain. Schultze and Moussa (1961) found that the power m ranges from 0.3 for dense sand to 0.8 for loose sand.

For general states of stress, the idea of stress-dependency can be included in Hooke's law by formulating a tangential stiffness modulus as a stress-dependent quantity obeying a power law:

$$G_t = G^{ref} \left[\frac{p}{p^{ref}}\right]^{m} \tag{2.10}$$

Correspondingly, the tangent Young's modulus E_t or the tangent bulk modulus K_t can also be formulated by such a power law. The superscript *ref* denotes a particular reference value. The power m is supposed to be a material constant, ranging from 0.0 to 1.0. For sand and overconsolidated clay the average of the power is about 0.5, whereas for normally and near-normally consolidated clay it is approximately 1.0. In the latter case $(m = 1)$ the volumetric strain rate is given by:

$$\dot{\varepsilon}_v = \frac{1}{K_t}\dot{p} = \frac{p^{ref}}{K^{ref}}\frac{\dot{p}}{p} \tag{2.11}$$

Integration of this equation gives a logarithmic stress-strain relation, similar to Terzaghi's logarithmic compression law (Terzaghi, 1925).

$$\varepsilon_v - \varepsilon_v^0 = \frac{p^{ref}}{K^{ref}} \ln\left[\frac{p}{p^0}\right] \tag{2.12}$$

In this relation the ratio p^{ref} / K^{ref} can be considered as a compression index.

The current power law model is very easy to implement in numerical procedures. However, It should be noted that a straightforward use of a tangent shear modulus, as defined by Equation 2.10, does not lead to a truly elastic model in the sense that strains are fully recovered when returning to the initial stress level. Another anomaly relates to energy. A sound constitutive model should not allow for the generation of energy for any form of cyclic loading. In order to get a fully proper elasticity model the formulation must involve a strain-energy function, as mentioned in the introduction of this chapter.

2.3 Elastic power law model by Vermeer

On improving the previous elastic model, a complementary strain-energy function W_c is introduced. This implies that the strains and strain rates are respectively given by:

$$\underline{\varepsilon} = \frac{\partial W_c}{\partial \underline{\sigma}} \qquad\qquad \dot{\underline{\varepsilon}} = \frac{\partial^2 W_c}{\partial \underline{\sigma}^2}\dot{\underline{\sigma}} \tag{2.13}$$

Various strain-energy functions exist in literature. In this section a complementary strain-energy function according to Vermeer (1980) is analysed. Note that the formulation in Equation 2.14 is fully equivalent to the more complex formulation given by Vermeer.

$$W_c = \frac{3}{2}\,\frac{1}{2-m}\,\frac{1-2\nu_s}{1+\nu_s}\,\frac{\sigma^2}{G_s} \tag{2.14}$$

In this function ν_s is a constant secant Poisson's ratio, G_s is a non-constant secant shear modulus and σ is a particular stress measure as defined by Vermeer (1980).

$$\sigma = p \sqrt{1 + \frac{2}{9} \frac{1+\nu_s}{1-2\nu_s} \frac{q^2}{p^2}} \tag{2.15}$$

$$G_s = G^{ref} \left[\frac{\sigma}{p^{ref}} \right]^m \tag{2.16}$$

G^{ref} and m are model parameters. Similar to the tangent shear modulus as defined in Equation 2.10, the above secant modulus obeys a power law.

In the following, the above strain-energy function will be examined to assess its suitability for the modelling of soil behaviour. The model is subject to oedometer test conditions in order to evaluate the behaviour in constant stress ratio paths. In addition, the model is subject to triaxial test conditions for which the development of tangential moduli is evaluated. For constant strain ratio paths it is sufficient to derive the (full) strains, as defined by the first part of Equation 2.13. In order to evaluate tangential moduli one also needs the rates of strain, as defined by the second part of Equation 2.13.

In the current model the strains are given by:

$$\underline{\varepsilon} = \frac{1}{2\,G_s} \left[\underline{\sigma} - \frac{3\,\nu_s}{1+\nu_s}\, \underline{\delta}\, p \right] \tag{2.17}$$

where $\underline{\delta} = (1,\ 1,\ 1,\ 0,\ 0,\ 0)^{\mathrm{T}}$. Equation 2.17 is identical to Hooke's law for isotropic material behaviour and all non-linearity is contained in Equation 2.16 for the secant shear modulus. For the special case of $\nu_s = 0$ the rates of strain are given by:

$$\underline{\dot{\varepsilon}} = \frac{1}{2\,G_s} \left[\underline{\dot{\sigma}} - m \frac{\underline{\sigma}\, \underline{\sigma}^T\, \underline{\underline{I}}^*\, \underline{\dot{\sigma}}}{\underline{\sigma}^T\, \underline{\underline{I}}^*\, \underline{\sigma}} \right] \qquad (\nu_s = 0) \tag{2.18}$$

where $\underline{\underline{I}}^* = diag(1,\ 1,\ 1,\ 2,\ 2,\ 2)$. The behaviour of the model under special axi-symmetric conditions ($\sigma_2 = \sigma_3$, $\varepsilon_2 = \varepsilon_3$), as obtained in oedometer tests and triaxial tests, can easily be analysed by considering the invariants of stress and strain, as defined in Section 2.1. The invariants of strain can be elaborated as:

$$\varepsilon_v = \frac{\partial W_c}{\partial p} = \frac{3}{2}\,\frac{1-2\nu_s}{1+\nu_s}\,\frac{p}{G_s} \approx \frac{3}{2}\,\frac{1-2\nu_s}{1+\nu_s}\,\frac{(p^{ref})^m}{G^{ref}}\,p^{1-m} \tag{2.19a}$$

$$\varepsilon_s = \frac{\partial W_c}{\partial q} = \frac{1}{3}\,\frac{q}{G_s} \tag{2.19b}$$

The approximation in Equation 2.19a is exact for isotropic compression. More generally, for constant stress ratio paths $(q\,/\,p = constant)$, as for instance observed in an oedometer test on normally consolidated soil, the volumetric strain is proportional to p^{1-m}. Experimental evidence for this proportionality with respect to sandy material (m about 0.5) was already mentioned by Vermeer (1980). In the limiting case of $m = 1$, i.e. for normally consolidated clay, the volumetric strain becomes independent from the mean stress. This is associated with full incompressibility which is not relevant for effective soil behaviour. Moreover, full incompressibility leads to numerical problems when implementing such a model in a computer code. In order to use the current model to simulate the behaviour of clay, the power m might be taken slightly below 1.0.

On taking the quotient of Equations 2.19a and 2.19b, it can be seen that a constant stress ratio path results in a constant strain ratio path. Herewith, the model complies with one of the basic model requirements. On imposing the conditions for oedometer testing $(\varepsilon_v\,/\,\varepsilon_s = 3\,/\,2)$ one can evaluate the stress ratio $(q\,/\,p)_0$. The relation with the coefficient of lateral earth pressure for normally consolidated soils, K_0, is given by:

$$\left[\frac{q}{p}\right]_0 = \frac{3\,(1 - K_0)}{1 + 2K_0} \qquad (\sigma_2 = \sigma_3) \tag{2.20}$$

Substitution of this relation and elaboration leads to the usual expression:

$$K_0 = \frac{\nu_s}{1 - \nu_s} \tag{2.21}$$

Note that this relationship is only valid in the absence of plastic strain, i.e. when modelling soil as purely elastic material or when extending the model to include perfect plasticity as described in Chapter 3. Hence, only when using the current elasticity model as a solitary model or when using it in combination with perfect plasticity, the value of K_0 only depends on the secant Poisson's ratio ν_s. In order to produce realistic values of K_0, say around 0.5 as usual in normally consolidated soil, ν_s should be about 1/3. In combination with hardening plasticity, as for instance covered in Chapter 4, K_0 is dominated by plasticity parameters. In that case the value of ν_s hardly influences K_0.

For a further examination of the model, attention is focused on a stress path for a standard drained triaxial loading test. The soil sample is assumed to collapse at a vertical stress of four times the confining pressure p^0. Hence, the stress state ranges from $p = p^0$ and $q = 0$ to $p = 2\,p^0$ and $q = 3\,p^0$. From Equations 2.15 and 2.16 it can be evaluated that during loading the secant shear modulus increases by a factor 1.57 for $\nu_s = 0$ and $m = 0.5$ and by a factor 2.45 for $\nu_s = 0$ and $m = 1$. If the current model were to be used solitarily or in combination with perfect plasticity, the stiffness behaviour would be in contradiction with what is generally observed in triaxial loading tests. Hardening plasticity can improve this anomaly. For unloading behaviour, the development of the stiffness is qualitatively correct.

Attention is now focused on the evolution of the tangent Poisson's ratio. Considering standard triaxial test conditions with $\sigma_2 = \sigma_3$ and $\dot{\sigma}_2 = \dot{\sigma}_3 = 0$, it can be derived that:

$$\nu_t = -\frac{\dot{\varepsilon}_3}{\dot{\varepsilon}_1} = -\frac{\dot{\varepsilon}_v / \dot{\varepsilon}_s - \frac{3}{2}}{\dot{\varepsilon}_v / \dot{\varepsilon}_s + 3} \tag{2.22}$$

The rates of the strain invariants are given by:

$$\dot{\varepsilon}_v = \frac{\partial \varepsilon_v}{\partial p}\,\dot{p} + \frac{\partial \varepsilon_v}{\partial q}\,\dot{q} = \frac{1}{3\,G_s}\,\frac{p^2}{\sigma^2}\left[\frac{9}{2}\,\frac{1-2\nu_s}{1+\nu_s}\left(\frac{\sigma^2}{p^2} - m\right)\dot{p} - m\,\frac{q}{p}\,\dot{q}\right] \tag{2.23a}$$

$$\dot{\varepsilon}_s = \frac{\partial \varepsilon_s}{\partial p}\,\dot{p} + \frac{\partial \varepsilon_s}{\partial q}\,\dot{q} = \frac{1}{3\,G_s}\,\frac{p^2}{\sigma^2}\left[-m\,\frac{q}{p}\,\dot{p} + \left((1-m)\,\frac{\sigma^2}{p^2} + m\right)\dot{q}\right] \tag{2.23b}$$

or in matrix form:

$$\begin{bmatrix} \dot{\varepsilon}_v \\ \dot{\varepsilon}_s \end{bmatrix} = \frac{1}{3\,G_s}\,\frac{p^2}{\sigma^2}\begin{bmatrix} \frac{9}{2}\,\frac{1-2\nu_s}{1+\nu_s}\left(\frac{\sigma^2}{p^2} - m\right) & -m\,\frac{q}{p} \\ -m\,\frac{q}{p} & (1-m)\,\frac{\sigma^2}{p^2} + m \end{bmatrix}\begin{bmatrix} \dot{p} \\ \dot{q} \end{bmatrix} \tag{2.24}$$

It can be seen that for isotropic stress states ($q = 0$ and $\sigma = p$) and $m = 1$ the determinant of the above material matrix is zero, which means that the matrix has become singular. Hence, the case $m = 1$ cannot be used in incremental numerical procedures, because of possible matrix singularity. Singularity certainly does not occur for $m < 1$ because $\sigma \geq p$.

The strain ratio as required in Equation 2.22 for the tangent Poisson's ratio yields:

$$\frac{\dot{\varepsilon}_v}{\dot{\varepsilon}_s} = \frac{\frac{9}{2}\,\frac{1-2\nu_s}{1+\nu_s}\left[\frac{\sigma^2}{p^2} - m\right] - m\,\frac{q}{p}\,\frac{\dot{q}}{\dot{p}}}{-m\,\frac{q}{p} + \left[(1-m)\,\frac{\sigma^2}{p^2} + m\right]\frac{\dot{q}}{\dot{p}}} \tag{2.25}$$

In a standard drained triaxial test the stress ratio $\dot{q}\ /\ \dot{p}$ is equal to 3. Substitution of this ratio into the above relation and successively into Equation 2.22 yields for the tangent Poisson's ratio:

$$\nu_t = -\,\frac{(1-m)\,\frac{1-2\nu_s}{1+\nu_s} - 1 - \frac{m}{3}\,\frac{q}{p} + \frac{2}{9}\left[1 - (1-m)\,\frac{1+\nu_s}{1-2\nu_s}\right]\frac{q^2}{p^2}}{(1-m)\,\frac{1-2\nu_s}{1+\nu_s} + 2 - \frac{4}{3}\,m\,\frac{q}{p} + \frac{2}{9}\left[1 + 2(1-m)\,\frac{1+\nu_s}{1-2\nu_s}\right]\frac{q^2}{p^2}} \tag{2.26}$$

For the special case of $\nu_s = 0$ the above expression reduces to:

$$\nu_t = \frac{m\left[1 + \frac{1}{3}\,\frac{q}{p} - \frac{2}{9}\,\frac{q^2}{p^2}\right]}{(3-m) - \frac{4}{3}\,m\,\frac{q}{p} + \frac{2}{9}\,\frac{q^2}{p^2}\,(3-2m)} \qquad (\nu_s = 0) \tag{2.27}$$

On defining the principal stress ratio $R = \sigma_1\ /\ \sigma_3$, the ratio $q\ /\ p$ under axi-symmetric conditions can be formulated as:

$$\frac{q}{p} = \frac{3\,(R-1)}{R+2} \qquad (\sigma_2 = \sigma_3) \tag{2.28}$$

Substitution of this relation into Equation 2.27 gives a very simple expression for the tangent Poisson's ratio:

$$\nu_t = \frac{m}{(1-m)R + 2/R} \qquad (\nu_s = 0 \ , \ \sigma_2 = \sigma_3) \qquad (2.29)$$

Taking $m = 0.5$ as an average for sand, ν_t varies between 0.20 and 0.25. This agrees well with general findings for unloading / reloading, as for instance published by Lade (1977). Hence, this elastic model with $m = 0.5$ and $\nu_s = 0$ is of interest in combination with hardening plasticity; the elastic strains will be of import for unloading / reloading and the plastic strains will be of import for primary loading.

On using a value of ν_s larger than zero, as needed in combination with perfect plasticity to obtain a realistic K_0, the tangent Poisson's ratio yields relatively large values which are not realistic.

Taking m slightly below 1 to simulate the behaviour of normally consolidated clay and ν_s equal to zero, then it is found that $\nu_t \approx$ R / 2, as can be seen from Equation 2.29. This means that soon after the onset of loading the current model shows an increasing amount of dilatancy, which is highly unrealistic for loading behaviour of normally consolidated clay. On using a value of ν_s larger than zero, the dilatancy effect is even larger.

From the above considerations it can be concluded that the power law model with a complementary strain-energy function as defined in this section is well applicable to model the behaviour of sand in the elastic range using a power m of about 0.5 and ν_s equal to zero. In order to simulate the behaviour of sand in different stress paths accurately, the model should be used in combination with hardening plasticity, as done for instance by Vermeer (1980). If the model is combined with perfect plasticity, the secant Poisson's ratio should be based on K_0, which will give a value of ν_s between 0.3 and 0.4. However, in this case the behaviour as observed in triaxial loading tests is not accurately predicted.

Using a power of exactly 1 may lead to singularity of the material matrix. Therefore the model cannot be used for modelling normally consolidated clays with $m = 1$. On taking m slightly below 1, the model gives dilatancy in triaxial loading tests, which is unrealistic for normally consolidated clay. Moreover, for unloading / reloading under oedometer test conditions, the model predicts highly unrealistic stress paths.

2.4 Elastic power law model by Molenkamp

In this section another non-linear elastic model is evaluated. An essential difference with the previous model is that the non-linearity is not only contained in the secant shear modulus, but in other parts of the model as well. Notwithstanding the non-linearity, a Hookean structure is still present in the relationship between stresses and strains. The model was originally proposed by Molenkamp (1988). However, model parameters are chosen here to be basically different from the proposal by Molenkamp for reasons discussed later in this section. The model is given here by the following complementary strain-energy function:

$$W_c = \frac{1}{G_s} \left[\frac{S\ p^2}{(1-m)\ (2-m)} + \frac{q^2}{6} \right] \qquad (2.30)$$

In this function G_s is again a secant shear modulus which obeys a power law:

$$G_s = G^{ref} \left[\frac{p}{p^{ref}} \right]^m \qquad (2.31)$$

This power law with reference stiffness G^{ref}, reference pressure p^{ref} and power m is similar to that in the previous model. However, in the current model the secant stiffness only depends on the mean stress p and not on q. The parameter S in the above complementary strain-energy function represents the tangential stiffness ratio, defined as:

$$S = \frac{G_t}{K_t} \qquad (2.32)$$

For isotropic stress conditions $(q = 0)$ the parameter S relates to the tangent Poisson's ratio ν_t:

$$S = \frac{3}{2}\, \frac{1 - 2\,\nu_t}{1 + \nu_t} \qquad (q = 0) \qquad (2.33)$$

The current model will also be examined based on the invariants of stress and strain, as defined in Section 2.1, under special axi-symmetric conditions $(\sigma_2 = \sigma_3)$. Special attention is given to the case of m equal to 1 to simulate the behaviour of normally consolidated clay. The strain invariants ε_v and ε_s are evaluated from the above complementary strain-energy function according to the first part of Equation 2.13:

$$\varepsilon_v = \frac{p}{K_s} \qquad \frac{1}{K_s} = \frac{1}{G_s}\left[\frac{S}{1-m} - \frac{m}{6}\frac{q^2}{p^2}\right] \tag{2.34a}$$

$$\varepsilon_s = \frac{1}{3}\frac{q}{G_s} \tag{2.34b}$$

On taking the quotient of Equation 2.34a and 2.34b it follows that a constant stress ratio path results in a constant strain ratio path. Hence, the model complies with one of the basic model requirements.

Imposing the conditions for oedometer testing $(\varepsilon_v \,/\, \varepsilon_s = 3/2)$ and using Equation 2.20 for the relation between the stress ratio $q\,/\,p$ and K_0, leads to a quadratic expression for the coefficient of lateral earth pressure K_0:

$$A\,K_0^2 + B\,K_0 + C = 0 \tag{2.35}$$

in which the factors A, B and C are given by:

$$A = 8\,S + 3\,(1-m)\,(2-m) \tag{2.36a}$$

$$B = 8\,S - 3\,(1-m)\,(1-2m) \tag{2.36b}$$

$$C = 2\,S - 3\,(1-m)\,(1+m) \tag{2.36c}$$

On using the current model solitarily or in combination with perfect plasticity, K_0 is influenced by the parameter S as well as by the power m. Taking $m = 0.5$ to simulate the behaviour of sand, S should be taken of the order of 0.2 in order to find a realistic value of K_0 around 0.5. For a given K_0, the required value of S can be obtained by reformulating Equation 2.35:

$$S = \frac{3}{2}\,(1-m)\,\frac{(1-K_0)\,(1+2K_0+m-mK_0)}{(1+2K_0)^2} \tag{2.37}$$

On taking m equal to 1 to simulate the behaviour of normally consolidated clay, the resulting K_0 is always equal to -0.5, independent from the value of S, which is highly unrealistic. However, on combining the current strain-energy function with hardening plasticity, the value of S and m hardly influence K_0.

From Equations 2.30 and 2.34a it can be seen that the complementary strain-energy function and the volumetric strain are not even defined for the particular case $m = 1$. However, with the particular choice of model parameters as made in this study, the model does not degenerate when considering the stress-strain relation in rate form. Note that the formulation by Molenkamp (1988) is not defined at all for $m = 1$. Evaluation of the rates of the strain invariants from the complementary strain-energy function gives:

$$\dot{\varepsilon}_v = \frac{1}{3\,G_s}\left[\left[3\,S + \frac{m}{2}\,(1+m)\,\frac{q^2}{p^2}\right]\dot{p} - m\,\frac{q}{p}\,\dot{q}\right] \tag{2.38a}$$

$$\dot{\varepsilon}_s = \frac{1}{3\,G_s}\left[-m\,\frac{q}{p}\,\dot{p} + \dot{q}\right] \tag{2.38b}$$

From these relations it can be seen that even for the case $m = 1$ the material matrix remains regular under all stress conditions. Hence, when implementing the current model in incremental form, there is no numerical objection to using $m = 1$.

Considering a drained triaxial test in which the soil sample is supposed to collapse at a vertical stress of four times the confining pressure, it follows from Equation 2.31 that the secant stiffness increases by a factor 1.41 for $m = 0.5$ and by a factor 2 for $m = 1$. Hence, the increase of stiffness is less than in the previous model, which is considered to be a slight advantage.

The tangent Poisson's ratio is evaluated from Equation 2.22 on the conditions of a standard drained triaxial test. From Equations 2.38 it follows that the strain ratio $\dot{\varepsilon}_v \,/\, \dot{\varepsilon}_s$ is given by:

$$\frac{\dot{\varepsilon}_v}{\dot{\varepsilon}_s} = \frac{3\,S + \frac{m}{2}\,(1+m)\,\frac{q^2}{p^2} - m\,\frac{q}{p}\,\frac{\dot{q}}{\dot{p}}}{-\,m\,\frac{q}{p} + \frac{\dot{q}}{\dot{p}}} \tag{2.39}$$

Taking the ratio of invariant stress rates $\dot{q} \,/\, \dot{p}$ equal to 3 and substitution of Equation 2.39 into 2.22 leads to:

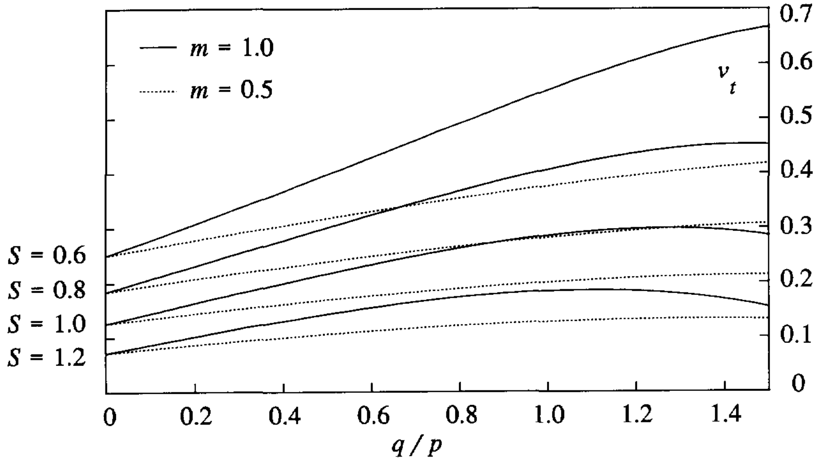

Figure 2.1 Tangent Poisson's ratio as a function of the stress ratio $q\ /\ p$

$$\nu_t = -\frac{2\,S - 3 - m\,\frac{q}{p} + \frac{m}{3}\,(1+m)\,\frac{q^2}{p^2}}{2\,S + 6 - 4\,m\,\frac{q}{p} + \frac{m}{3}\,(1+m)\,\frac{q^2}{p^2}} \tag{2.40}$$

The tangent Poisson's ratio is plotted in Figure 2.1 as a function of the stress ratio $q\ /\ p$ for different values of S and m. At the beginning of a triaxial test, the stress state is isotropic. As a result, the tangent Poisson's ratio relates here to the stiffness ratio S as formulated in Equation 2.33. During loading, ν_t gradually increases and finally decreases when the stress ratio $q\ /\ p$ approaches 1.5. The power m has a minor influence on the results and realistic values for ν_t of the order of 0.2 can be obtained for $m = 0.5$ as well as for $m = 1$ by choosing S around 1.0.

From the above considerations it can be concluded that the current power law model can very well be used to simulate the behaviour of sand in the elastic range using a power m of 0.5 and a value of S of about 1.0. When combining the model with perfect plasticity, the parameter S should be based on K_0, which will give a value of S around 0.2. The proper value can be evaluated from Equation 2.37.

For the simulation of the behaviour of normally consolidated clay in incremental numerical applications, the case $m = 1$ can be used exactly. This is due to the particular choice of model parameters in the current formulation. The case $m = 1$ is impossible in the original proposal by Molenkamp. The value of S should be just above 1.0 in order to find realistic stress paths for unloading / reloading both in triaxial tests and in oedometer tests. However, when using the current model solitarily or in combination with perfect-plasticity and taking $m = 1$ it is impossible to simulate a correct stress path for primary loading in oedometer tests. Hence, for clay it is highly recommended that the model be used in combination with hardening plasticity.

2.5 Hyperbolic Duncan-Chang model

The third type of non-linear elastic model is the adoption of a hyperbolic representation of stress-strain curves as obtained from triaxial tests. The original idea to approximate such curves by a hyperbola stems from Kondner (1963). Based on results from undrained triaxial tests he proposed an equation of the form:

$$|\sigma_1 - \sigma_3| = \frac{\varepsilon_1}{\dfrac{\varepsilon_1}{q_{ult}} - \dfrac{1}{E^0}} \tag{2.41}$$

In this equation E^0 represents the initial stiffness of the primary loading curve, which corresponds to the initial Young's modulus. Kondner already mentioned that in standard drained triaxial tests the initial stiffness modulus depends on several conditions among which the confining pressure. This idea was extended by Duncan and Chang (1970). Under the convention that the principal stresses are ordered in such a way that $\sigma_1 \leq \sigma_2 \leq \sigma_3$, they formulated the initial Young's modulus E^0 as a power function of σ_3, in accordance with the idea of Ohde (1939).

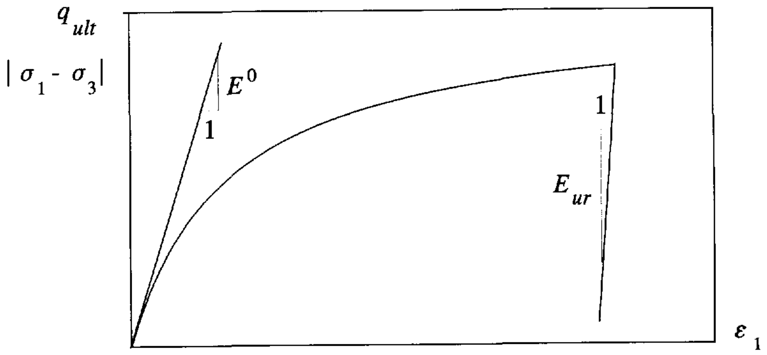

Figure 2.2 Hyperbolic approximation of a standard drained triaxial test

$$E^0 = E^{ref}\left[\frac{|\sigma_3|}{p_a}\right]^m \tag{2.42}$$

It should be noted that σ_3 is, in an absolute sense, the minimum principal stress, which equals the confining pressure in the case of a standard drained triaxial loading test. E^{ref} is a reference Young's modulus corresponding to the atmospheric pressure p_a. In Equation 2.41 q_{ult} represents the asymptotic value of the principle stress difference. This value can be expressed in terms of a friction angle and a cohesion according to Coulomb's friction law.

$$q_{ult} = \frac{1}{R_f}\,\frac{2\ c\ \cos\varphi\ -\ 2\ \sigma_3\ \sin\varphi}{1\ -\ \sin\varphi} \tag{2.43}$$

R_f is the failure ratio. Duncan and Chang report that for a number of different soils, values of R_f were found in the range from 0.75 to 1.00.

In order to apply the hyperbolic model in incremental form, a tangent stiffness modulus must be utilized. From Hooke's law one can formulate the tangent Young's modulus E_t as:

$$\frac{1}{E_t} = \frac{\partial\varepsilon_1}{\partial\sigma_1} \tag{2.44}$$

Reformulation of Equation 2.41 and elaboration gives:

$$E_t = E^{ref}\left[\frac{|\sigma_3|}{p_a}\right]^m \left[\frac{|\sigma_1 - \sigma_3| - q_{ult}}{q_{ult}}\right]^2 \tag{2.45}$$

The tangent Young's modulus, as defined in Equation 2.45, is applicable to general states of stress, provided that the ordering of principal stresses is taken into account.

For unloading and reloading, the stiffness is supposed to depend only on the minimum principle stress and not on the principle stress difference. This results in linear elastic behaviour for unloading and reloading in a standard drained triaxial test.

$$E_{ur} = E_{ur}^{ref}\left[\frac{|\sigma_3|}{p_a}\right]^m \tag{2.46}$$

The unloading / reloading Young's modulus E_{ur}, as defined in Equation 2.46, is similar to Equation 2.42 for the initial Young's modulus in primary loading. The only difference is in the reference stiffness, which is substantially higher for unloading / reloading than for primary loading.

The hyperbolic model is capable of describing specific soil characteristics such as the effect of stress-dependent stiffness, typical unloading / reloading behaviour and failure. However, there are still some major drawbacks.

The first point of discussion, as already indicated by Duncan and Chang themselves, is the role of Poisson's ratio, which is taken as a constant. They evaluated the tangent Poisson's ratio for a standard drained triaxial test on dense silica sand and found a range from 0.11 to 0.65. The large value of 0.65 represents the effect of dilatancy, which is often observed in dense sands beyond the elastic range. However, on using Hooke's law in incremental form as a basis of this non-linear elastic model, Poisson's ratio has an upper limit of 0.5. As a result, the model is not capable of describing effects like dilatancy.

The second drawback of the hyperbolic model is the inconsistency with respect to neutral loading. For loading, a low stiffness modulus E_t is used, whereas a much higher modulus E_{ur} is used for unloading. Loading is defined by the condition $d(\sigma_1/\sigma_3) > 0$ and unloading is defined as $d(\sigma_1/\sigma_3) < 0$. Hence, neutral loading is defined as a constant stress ratio path without change of σ_1 / σ_3. This type of stress path is, for instance, obtained in an oedometer test where $\sigma_1 / \sigma_3 = 1 / K_0$. For such stress paths, the hyperbolic model is inconsistent. Indeed, E_t might be used for $d(\sigma_1/\sigma_3) = 0$, but a near-constant stress ratio path with $d(\sigma_1/\sigma_3)$ just slightly negative would get the high E_{ur} modulus. Hence two nearly identical stress paths will give an entirely different strain response.

3 ELASTIC PERFECTLY-PLASTIC SOIL MODELS

In this chapter two basic elastic perfectly-plastic models are considered to set out the basis of plasticity theory. Some extensions of the well-known Mohr-Coulomb model are proposed for practical applicatibity. Finally it is shown how the Drucker-Prager model can match the Mohr-Coulomb model for dilating materials in plane strain situations.

3.1 The Drucker-Prager model

The Drucker-Prager model (Drucker & Prager, 1952) is well-known in soil mechanics and is operational in several computer codes. The basic idea of the model is adopted in other soil models. It is presented here as an introduction to more complex models and to establish the basis of plasticity theory.

The basic principle of elastoplastic models is that strains and strain rates are divided into an elastic part and a plastic part (Hill, 1950).

$$\underline{\varepsilon} = \underline{\varepsilon}^e + \underline{\varepsilon}^p \qquad\qquad \underline{\dot{\varepsilon}} = \underline{\dot{\varepsilon}}^e + \underline{\dot{\varepsilon}}^p \tag{3.1}$$

Hooke's law (Equation 2.5) is used to relate the stress rates to the elastic strain rates. Together with Equation 3.1 this gives:

$$\underline{\dot{\sigma}} = \underline{\underline{D}}^e \, \underline{\dot{\varepsilon}}^e = \underline{\underline{D}}^e \, (\underline{\dot{\varepsilon}} - \underline{\dot{\varepsilon}}^p) \tag{3.2}$$

The elastic parameters G and ν, as used in the matrix $\underline{\underline{D}}^e$, are taken as constants. A yield function f indicates whether or not plastic strain rates occur. The yield function for the Drucker-Prager model can conveniently be formulated in terms of p and q:

$$f = q - \alpha \, (p + c \cot\varphi) \tag{3.3}$$

This yield function represents a cone in principle stress space as shown in Figure 3.1. The term $c \cot\varphi$ is related with the distance from the apex of the cone to the origin of the principle stress space. The coefficient α relates to the friction angle φ, and determines the steepness of the cone. In the particular case of zero friction the term $\alpha \, p$ vanishes, but the term $\alpha \, c \cot\varphi$ does not vanish. In this case the Drucker-Prager model reduces to the Von Mises model, which is often used in metal plasticity.

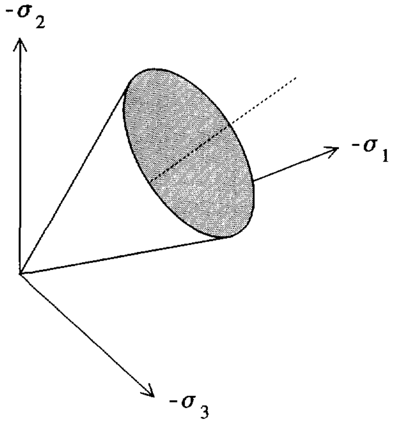

Figure 3.1 Drucker-Prager yield surface in principle stress space

According to the classical theory of plasticity (Hill, 1950), the plastic strain rates are proportional to the derivative of the yield function with respect to the stresses. This means that the plastic strain rates can be represented as a vector perpendicular to the yield surface. This classical definition of plastic strain rates is referred to as associated plasticity. However, for geomaterials, the classical definition leads to an overprediction of dilatancy. Therefore, in addition to the yield function, a plastic potential function g is introduced. The plastic potential function can also be represented as a surface in principal stress space. The case $g \neq f$ is denoted as non-associated plasticity. For the Drucker-Prager model the plastic potential function can be defined as:

$$g = q - \beta p \tag{3.4}$$

The coefficient β relates to the dilation angle ψ, and determines the direction of the plastic strain rates. In general, β is smaller than α, which implies non-associated plasticity. The plastic strain rates can be written as:

$$\underline{\dot{\varepsilon}}^p = \dot{\lambda} \frac{\partial g}{\partial \underline{\sigma}} \tag{3.5}$$

In which $\dot{\lambda}$ is the rate form of the so-called plastic multiplier. This is just a multiplier that does not have a direct physical meaning. In the case of purely elastic behaviour $\dot{\lambda}$ is zero whereas in the case of plastic behaviour $\dot{\lambda}$ is positive.

$$\dot{\lambda} = 0 \qquad \text{for} \qquad f < 0 \qquad \text{or} \qquad \frac{\partial f}{\partial \underline{\sigma}}^T \underline{\underline{D}}^e \, \dot{\underline{\varepsilon}} \leq 0 \qquad \text{(Elasticity)} \tag{3.6a}$$

$$\dot{\lambda} > 0 \qquad \text{for} \qquad f = 0 \qquad \text{and} \qquad \frac{\partial f}{\partial \underline{\sigma}}^T \underline{\underline{D}}^e \, \dot{\underline{\varepsilon}} > 0 \qquad \text{(Plasticity)} \tag{3.6b}$$

In order to evaluate the rate of the plastic multiplier, Prager's consistency condition for plastic flow is utilized, which reflects the principle that a material point remains in plastic state. Considering only perfect plasticity this condition can be formulated as:

$$\frac{\partial f}{\partial \underline{\sigma}}^T \dot{\underline{\sigma}} = 0 \tag{3.7}$$

Substitution of Equations 3.2 and 3.5 into Equation 3.7 enables solution of the rate of the plastic multiplier in terms of the (total) strain rate.

$$\dot{\lambda} = \frac{1}{d} \frac{\partial f}{\partial \underline{\sigma}}^T \underline{\underline{D}}^e \, \dot{\underline{\varepsilon}} \tag{3.8}$$

where

$$d = \frac{\partial f}{\partial \underline{\sigma}}^T \underline{\underline{D}}^e \frac{\partial g}{\partial \underline{\sigma}} \tag{3.9}$$

Back-substitution of this expression gives the general elastoplastic relation between stress rates and (total) strain rates. The second term in brackets in Equation 3.10 is absent in the case of elastic behaviour as defined in 3.6a.

$$\dot{\underline{\sigma}} = \left(\underline{\underline{D}}^e - \frac{1}{d} \, \underline{a} \, \underline{b}^T \right) \dot{\underline{\varepsilon}} \tag{3.10}$$

where

$$\underline{a} = \underline{\underline{D}}^e \frac{\partial g}{\partial \underline{\sigma}} \qquad\qquad \underline{b}^T = \frac{\partial f}{\partial \underline{\sigma}}^T \underline{\underline{D}}^e \tag{3.11}$$

The Drucker-Prager model is mathematically simple and easy to implement in a computer code. However, the model is not accurate for general stress paths, especially for highly frictional soil. A better elastoplastic model is to be considered in the next section.

3.2 The Mohr-Coulomb model

The most widely used elastic perfectly-plastic model for soil is the Mohr-Coulomb model (see among others Smith & Griffith, 1982). In addition to two elasticity parameters, it requires three plasticity parameters, namely the cohesion c, the friction angle φ, and the dilation angle ψ. The latter parameter is less well known in engineering practice than the friction angle and the cohesion, but it can easily be determined from standard drained triaxial test results.

The Mohr-Coulomb yield condition is an extension of Coulomb's friction law to general states of stress. In fact, this condition ensures that Coulomb's friction law is obeyed in any plane within a continuum. The full Mohr-Coulomb yield condition can conveniently be formulated in terms of principle stresses and involves three yield functions:

$$f_1 = \frac{1}{2} \left|\sigma_2 - \sigma_3\right| + \frac{1}{2} (\sigma_2 + \sigma_3) \sin\varphi - c \cos\varphi \tag{3.12a}$$

$$f_2 = \frac{1}{2} \left|\sigma_3 - \sigma_1\right| + \frac{1}{2} (\sigma_3 + \sigma_1) \sin\varphi - c \cos\varphi \tag{3.12b}$$

$$f_3 = \frac{1}{2} \left|\sigma_1 - \sigma_2\right| + \frac{1}{2} (\sigma_1 + \sigma_2) \sin\varphi - c \cos\varphi \tag{3.12c}$$

All yield functions together represent a hexagonal cone in principal stress space as shown in Figure 3.2. In the presence of cohesion, the distance between the apex of the cone and the origin of the principal stress space is equal to $\sqrt{3}\, c \cot\varphi$.

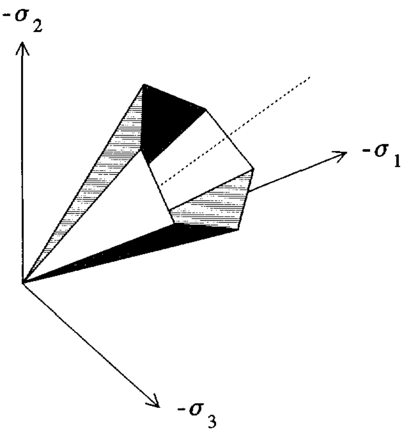

Figure 3.2 Mohr-Coulomb yield surface in principle stress space

Crossing the Mohr-Coulomb yield surface with a π-plane ($\sigma_1 + \sigma_2 + \sigma_3 = \text{constant}$) gives a hexagon. For a zero friction angle the hexagon is regular. This particular case is also known as the Tresca yield condition. For larger friction angles, the shape of the hexagon is heading towards a triangle. A regular triangle is obtained for the hypothetical case of $\varphi = 90°$. Researchers have indicated by means of true-triaxial tests that stress combinations causing failure in real soil samples agree quite well with the hexagonal shape of the Mohr-Coulomb yield surface (Goldscheider, 1984).

Plasticity models that involve more than one yield function require a special treatment of the so-called yield vertices, i.e. the crossing area of yield surfaces. According to Koiter's singular surface plasticity theory (1960) and Mandel's generalization (1965), the plastic strain rate can in general be written as the sum of contributions from all yield functions.

$$\underline{\dot{\varepsilon}}^p = \dot{\lambda}_1 \frac{\partial g_1}{\partial \underline{\sigma}} + \dot{\lambda}_2 \frac{\partial g_2}{\partial \underline{\sigma}} + \dot{\lambda}_3 \frac{\partial g_3}{\partial \underline{\sigma}} \tag{3.13}$$

The direction of the plastic strain rate is a linear combination of the vectors perpendicular to the corresponding plastic potential surfaces. For yield functions that do not contribute to plasticity as defined in 3.6b, the corresponding rates of plastic multipliers are zero according to the definition in 3.6a. The remaining unknown rates of plastic multipliers can be solved by applying Prager's consistency condition to all yield functions that do contribute to plastic straining. Should all three yield functions give plasticity, one obtains three equations with three unknowns:

$$\frac{\partial f_j}{\partial \underline{\sigma}}^T \underline{\underline{D}}^e \left[\underline{\dot{\varepsilon}} - \sum_{i=1}^{3} \dot{\lambda}_i \frac{\partial g_i}{\partial \underline{\sigma}} \right] = 0 \qquad (\text{ for } j = 1, 2, 3 \text{ }) \tag{3.14}$$

The solution can be written in the form:

$$\dot{\lambda}_i = \underline{\underline{A}}^{-1} \frac{\partial f_j}{\partial \underline{\sigma}}^T \underline{\underline{D}}^e \underline{\dot{\varepsilon}} \qquad (\text{ for } i = 1, 2, 3 \text{ and } j = 1, 2, 3 \text{ }) \tag{3.15}$$

where $\underline{\underline{A}}$ contains all combinations of d_{ij}:

$$\underline{\underline{A}} = \begin{bmatrix} d_{11} & d_{12} & d_{13} \\ d_{21} & d_{22} & d_{23} \\ d_{31} & d_{32} & d_{33} \end{bmatrix} \qquad d_{ij} = \frac{\partial f_i}{\partial \underline{\sigma}}^T \underline{\underline{D}}^e \frac{\partial g_j}{\partial \underline{\sigma}} \tag{3.16}$$

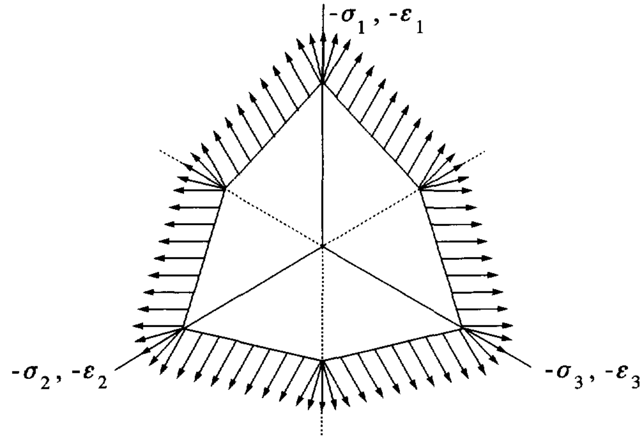

$-\sigma_1$, $-\varepsilon_1$
$-\sigma_2$, $-\varepsilon_2$
$-\sigma_3$, $-\varepsilon_3$

Figure 3.3 Projection of plastic strain vectors on a π-plane ($\varphi = 30°$; $\psi = 0°$)

The singular surface plasticity theory results in a fan of possible plastic strain vectors starting in the yield vertices. For the Mohr-Coulomb model the orientation of plastic strain vectors can very well be visualized by projection on a π-plane as shown in Figure 3.3.

The usual procedure for deriving the elastoplastic stress-strain relation is to solve the set of three equations analytically. Implementation of such an approach in a computer code requires, in general, a distinct treatment for different combinations of yield functions that contribute to plastic straining. A more convenient approach is presented below for establishing the full elastoplastic stress-strain relation by means of a repetitive procedure, which can easily be implemented in a computer code. The example is demonstrated for the case that all three yield functions of the Mohr-Coulomb model contribute to plasticity. However, the procedure can be used for any case where one or more yield functions contribute to plastic straining.

First an auxiliary strain tensor is defined as:

$$\underline{\dot{\varepsilon}}_j = \underline{\dot{\varepsilon}} - \sum_{i=1}^{j} \dot{\lambda}_i \frac{\partial g_i}{\partial \underline{\sigma}} \qquad (3.17)$$

For $j = 3$ one get $\underline{\dot{\varepsilon}}_3 = \underline{\dot{\varepsilon}}^e$ and for $j = 0$ $\underline{\dot{\varepsilon}}_0 = \underline{\dot{\varepsilon}}$. Similarly, an auxiliary matrix $\underline{\underline{M}}_j$ is introduced in such a way that $\underline{\dot{\sigma}} = \underline{\underline{M}}_j \, \underline{\dot{\varepsilon}}_j$. Hence, $\underline{\underline{M}}_3 = \underline{\underline{D}}^e$ and $\underline{\underline{M}}_0 = \underline{\underline{M}}$. Starting with $j = 3$ the normal procedure, as given in Section 3.1, can be followed.

$$\dot{\underline{\sigma}} = \underline{\underline{M}}_3 \, \dot{\underline{\varepsilon}}_3 = \underline{\underline{M}}_3 \left[\dot{\underline{\varepsilon}}_2 - \dot{\lambda}_3 \frac{\partial g_3}{\partial \underline{\sigma}} \right] \tag{3.18}$$

Prager's consistency condition for $j = 3$ yields:

$$\frac{\partial f_3}{\partial \underline{\sigma}}^T \underline{\underline{M}}_3 \left[\dot{\underline{\varepsilon}}_2 - \dot{\lambda}_3 \frac{\partial g_3}{\partial \underline{\sigma}} \right] = 0 \quad \Rightarrow \quad \dot{\lambda}_3 = \frac{1}{d_{33}} \frac{\partial f_3}{\partial \underline{\sigma}}^T \underline{\underline{M}}_3 \, \dot{\underline{\varepsilon}}_2 \tag{3.19}$$

where

$$d_{33} = \frac{\partial f_3}{\partial \underline{\sigma}}^T \underline{\underline{M}}_3 \frac{\partial g_3}{\partial \underline{\sigma}} \tag{3.20}$$

Back-substitution of Equation 3.19 into Equation 3.18 gives:

$$\dot{\underline{\sigma}} = \left[\underline{\underline{M}}_3 - \frac{1}{d_{33}} \underline{\underline{M}}_3 \frac{\partial g_3}{\partial \underline{\sigma}} \frac{\partial f_3}{\partial \underline{\sigma}}^T \underline{\underline{M}}_3 \right] \dot{\underline{\varepsilon}}_2 = \underline{\underline{M}}_2 \, \dot{\underline{\varepsilon}}_2 \tag{3.21}$$

Hence, $\underline{\underline{M}}_2$ can simply be obtained from $\underline{\underline{M}}_3$ by means of the usual procedure for one yield function. Continuing with $j = 2$, $\underline{\underline{M}}_1$ can be obtained from $\underline{\underline{M}}_2$ and finally for $j = 1$ one obtains $\underline{\underline{M}}_0$ from $\underline{\underline{M}}_1$. $\underline{\underline{M}}_0$ is the required elastoplastic material stiffness matrix $\underline{\underline{M}}$.

3.3 Improvements to the Mohr-Coulomb model

From an engineering point of view, the Mohr-Coulomb model is reasonably well suited to simulate the behaviour of most geomaterials. However, because of the stress-dependency in true soil behaviour, special attention should be paid to the determination of the (constant) elastic stiffness parameter in the Mohr-Coulomb model. Another point of discussion is the fact that the tensile strength is overpredicted for highly cohesive materials. Moreover, it should be realized that after large distortion the material arrives in a state of maximum porosity where dilatancy has come to an end. The final point of discussion is the absence of a yield surface for compressive stress paths. Using the Mohr-Coulomb model, compression does not lead to irrecoverable strain, which is particularly unrealistic for soft materials such as normally consolidated clay and peat.

The basic Mohr-Coulomb model can be extended to improve some of the limitations as formulated before. A first improvement is the introduction of a stress-dependent stiffness relation. This can be achieved by formulating a tangent shear modulus as a power function of the stress level (Section 2.2) or by using a secant shear modulus in combination with a strain-energy function (Section 2.3 or 2.4). Instead of just using the mean stress p as a stress level, it is realistic to include a cohesion term as well. In the simplest case of a tangent shear modulus this gives:

$$G_t = G^{ref} \left[\frac{p^*}{p^{ref}} \right]^m \tag{3.22}$$

where

$$p^* = -\frac{1}{3}(\sigma_1 + \sigma_2 + \sigma_3) + c \cot\varphi \tag{3.23}$$

In the absence of the cohesion terms, the stiffness becomes zero at the surface level of a non-loaded soil body where $p = 0$. In reality, materials that either show effective or apparent cohesion still have strength and stiffness for $p = 0$, so inclusion of the cohesion term seems logical. The value $c \cot\varphi$ relates to the distance from the apex of the Mohr-Coulomb yield surface to the origin of the principle stress space.

A second improvement is the limitation of the tensile strength by means of a so-called tension cut-off. Therefore, three additional yield surfaces are introduced,

$$f_4 = \sigma_1 - \sigma_t \tag{3.24a}$$

$$f_5 = \sigma_2 - \sigma_t \tag{3.24b}$$

$$f_6 = \sigma_3 - \sigma_t \tag{3.24c}$$

in which σ_t is the tensile strength of the material, usually taken zero. For the additional yield functions as defined in Equation 3.24 it is sufficient to adopt an associated flow rule. The new vertices that arise can be treated according to the singular surface plasticity theory as explained in the previous section.

Another improvement to the Mohr-Coulomb model is achieved by a dilatancy cut-off. To this end the initial dilation angle ψ_{init}, the initial void ratio e_{init}, and the maximum void ratio e_{max} of the material are entered as model parameters. As soon as the volume change results in a state of maximum void, the dilation angle ψ is automatically set back to zero.

$$\psi = \psi_{init} \qquad \text{for} \qquad e < e_{max} \tag{3.25a}$$

$$\psi = 0 \qquad \text{for} \qquad e = e_{max} \tag{3.25b}$$

The void ratio is related to the volumetric strain by:

$$\varepsilon_v^0 - \varepsilon_v = \ln\left[\frac{1+e}{1+e^0}\right] \approx \frac{e - e^0}{1 + e} \tag{3.26}$$

or in rate form:

$$\dot{\varepsilon}_v = -\frac{\dot{e}}{1+e} \tag{3.27}$$

The Mohr-Coulomb model with the extensions as described in this section is referred to as the Advanced Mohr-Coulomb model.

The importance of the dilatancy cut-off is limited to some special applications in engineering practice. As an example, the tension pile problem of Figure 3.4 is considered, which is based on a scale model test by Boulon & Foray (1986). A model pile was installed in a cylindrical container before it was filled with sand. The container has a diameter of 1.5 m and a depth of 2.0 m. The pile has a length of 1.6 m and a diameter of 55 mm. The model test was performed with dense and loose sand. In the present analysis only the case with dense sand is considered. In contrast to the model test where the pile was pulled by cyclic loading, the present analysis concerns one-way loading.

An axi-symmetric finite element mesh, containing 30 15-noded cubic strain elements with 12-point Gaussian integration, was used to model the geometry. This type of element performs particularly well in failure analyses of axi-symmetric configurations (Sloan & Randolph, 1982). Special compatible 10-noded interface elements (Van Langen, 1991) were used to model the soil-structure interaction, indicated with dashed lines in Figure 3.4. The Advanced Mohr-Coulomb model was used to model the sand behaviour in the volume elements as well as in the interface elements. The behaviour of the pile was modelled by Hooke's law of elasticity. The model parameters of the sand are based on data as given by Boulon & Foray (1986).

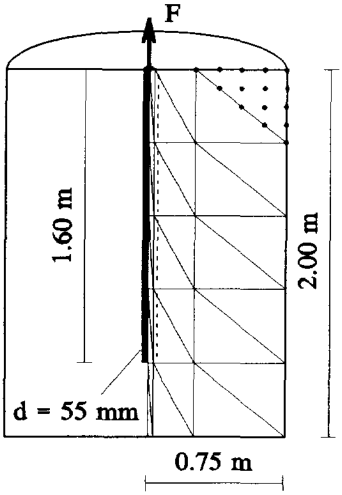

Sand		
Soil weight	γ	= 16.7 kN/m^3
Shear modulus	G^{ref}	= 15000 kPa
	(p^{ref}	= 100 kPa)
Power	m	= 0.5
Poisson's ratio	ν	= 0.3
Cohesion	c	= 1 kPa
Friction angle	φ	= 45°
Dilation angle	ψ	= 15°
Initial void ratio	e_{init}	= 0.59
Max. void ratio	e_{max}	= 0.72
Interface		
Friction angle	φ_i	= 39°
Dilation angle	ψ_i	= 9°

Figure 3.4 Tension pile geometry, finite element schematization and model parameters

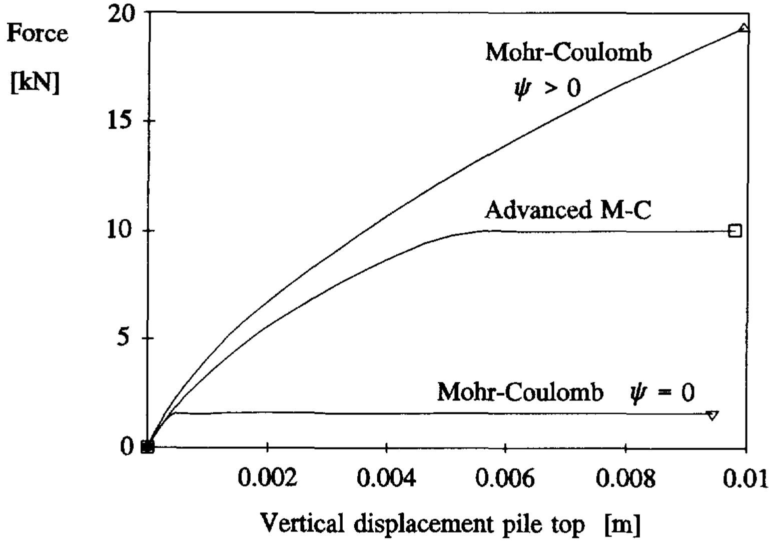

Figure 3.5 Force-displacement curves from tension pile problem

After installation of the initial stresses in the soil mass, a small vertical load of 1 kPa was applied on top of the sand to initialize the proper contact forces between the sand and the pile. In addition, the tension force at the top of the pile was applied until the pile was pulled out of the sand. The same calculation was repeated for the case that the sand was modelled with the conventional Mohr-Coulomb model, both with and without dilatancy. In these cases the constant shear modulus was chosen to be 7500 kPa. The force-displacement curves that followed from the three calculations are given in Figure 3.5.

It can be seen from Figure 3.5 that the conventional Mohr-Coulomb model without the dilatancy cut-off does not show an ultimate force. The continuously increasing dilatancy promotes the lateral stress in the sand, which gives a continuously increasing shear strength along the pile. In the case without dilatancy, the ultimate force is relatively low and the horizontal stress in the sand hardly increases. The curve from the Advanced Mohr-Coulomb model indeed shows a failure load as soon as the material along the pile has arrived in a state of maximum void. The ultimate force is about 10 kN, which agrees quite well with the observations from the model test. It should be mentioned that the ultimate force is very sensitive with respect to the width of the shear zone along the pile, i.e. the interface thickness. In the present calculation the (virtual) interface thickness was taken as 3 mm.

The influence of the stress-dependent stiffness is difficult to examine from the force-displacement curves. The mean stress increases because of the increasing lateral stress in the sand. This will increase the elastic stiffness according to Equation 3.22. However, the stiffening effect is eliminated by the weakening effect of points that lose their dilatancy.

3.4 Matching Drucker-Prager and Mohr-Coulomb for plane strain

The major point of discussion on using the Drucker-Prager model is the determination of a proper value for the friction parameter α. If α is chosen such that the model correctly reflects the material strength for triaxial compression states of stress $(\sigma_1 \leq \sigma_2 = \sigma_3)$ then it overpredicts the strength for other stress states (Chen, 1975; Owen & Hinton, 1980). It should be realized that different stress states can occur simultaneously in a three-dimensional soil body, which makes it difficult to choose a proper value for α. In the particular case of a plane strain configuration $(\varepsilon_{zz} = \varepsilon_{yz} = \varepsilon_{zx} = 0)$ a realistic choice of α can be made, as will be demonstrated below. In the derivation it is assumed that the principle stresses are ordered such that $\sigma_1 < \sigma_2 < \sigma_3$, where the intermediate principle stress is supposed to be the out-of-plane stress $(\sigma_2 = \sigma_{zz})$. From the plane strain condition it follows that:

$$\dot{\varepsilon}^p_{zz} = \dot{\lambda} \frac{\partial g}{\partial \sigma_2} = 0 \tag{3.28}$$

On substituting the derivative of the Drucker-Prager plastic potential function towards σ_2 and assuming that the rate of the plastic multiplier is non-zero, one obtains:

$$\sigma_2 = \frac{1}{2} \sigma_1 + \frac{1}{2} \sigma_3 - \frac{1}{3} q \beta \tag{3.29}$$

Elaboration of p and q gives:

$$p = -\frac{1}{2} (\sigma_1 + \sigma_3) + \frac{1}{2} (\sigma_1 - \sigma_3) \omega \frac{\beta}{9} \tag{3.30a}$$

$$q = \frac{1}{2} (\sigma_1 - \sigma_3) \omega \tag{3.30b}$$

where

$$\omega = \frac{\sqrt{3}}{\sqrt{1 - \frac{1}{9} \beta^2}} \tag{3.31}$$

Note that $(\sigma_1 + \sigma_3) / 2$ is the centre of Mohr's stress circle and $-(\sigma_1 - \sigma_3) / 2$ is the radius of Mohr's stress circle. On substituting the above expression in the Drucker-Prager yield condition (Equation 3.3 ; $f = 0$) one obtains:

$$\frac{1}{2} (\sigma_1 - \sigma_3) - \frac{1}{2} (\sigma_1 + \sigma_3) \frac{\alpha / \omega}{1 - \frac{\alpha \beta}{9}} + c \cot\varphi \frac{\alpha / \omega}{1 - \frac{\alpha \beta}{9}} = 0 \tag{3.32}$$

Equation 3.32 is formally identical to the Mohr-Coulomb yield condition (3.12b). Both yield conditions become fully identical when using

$$\alpha = \frac{\omega \sin\varphi}{1 + \frac{\beta}{9} \omega \sin\varphi} \tag{3.33}$$

Note that the value of α also depends on the dilatancy parameter β. For a dilation angle of zero ($\psi = 0$; $\beta = 0$; $\omega = \sqrt{3}$) the above expression reduces to the formula given by Chen (1975). The general case of $\psi \neq 0$ cannot be found in literature and will be further elaborated below.

Dilatancy is related to the plastic strain rates, as defined below for plane strain conditions:

$$\sin\psi = \frac{\dot{\varepsilon}_3^p + \dot{\varepsilon}_1^p}{\dot{\varepsilon}_3^p - \dot{\varepsilon}_1^p} \tag{3.34}$$

The required plastic strain rates, as obtained from the Drucker-Prager model, are:

$$\dot{\varepsilon}_1^p = \dot{\lambda} \left[\frac{2\,\sigma_1 - \sigma_2 - \sigma_3}{2\,q} + \frac{1}{3}\,\beta \right] \tag{3.35a}$$

$$\dot{\varepsilon}_3^p = \dot{\lambda} \left[\frac{-\,\sigma_1 - \sigma_2 + 2\,\sigma_3}{2\,q} + \frac{1}{3}\,\beta \right] \tag{3.35b}$$

Substitution into Equation 3.34 and elaboration gives:

$$\sin\psi = \frac{2\,q\,\beta}{3\,(\sigma_1 - \sigma_3)} = \frac{\frac{1}{3}\sqrt{3}\;\beta}{\sqrt{1 - \frac{1}{9}\,\beta^2}} \tag{3.36}$$

Reformulation of the latter identity in Equation 3.36 gives an expression for β in terms of the dilation angle ψ.

$$\beta = \frac{\sqrt{3}\,\sin\psi}{\sqrt{1 + \frac{1}{3}\,\sin^2\psi}} \tag{3.37}$$

Based on the friction angle φ and the dilation angle ψ and with help of Equations 3.31, 3.33 and 3.37, the Drucker-Prager model can predict realistic failure behaviour for plane strain configurations. However, as mentioned before, for general states of stress in a three-dimensional continuum the Drucker-Prager model does not predict failure accurately.

4 HARDENING PLASTICITY

In contrast to perfect plasticity, the yield surface for hardening and softening plasticity models has no fixed position in stress space. Hardening is associated with an expanding yield surface, whereas softening is associated with a shrinking yield surface. As an example of hardening models, the Modified Cam-Clay model is discussed in this chapter. Attention is given to parameters that determine the coefficient of lateral earth pressure in one-dimensional compression. A simple cap model is presented based on the Modified Cam-Clay model. The stiffness behaviour of the model is analysed for different stress paths.

4.1 The Modified Cam-Clay model

The Cam-Clay model was developed in the sixties at Cambridge University (Schofield & Wroth, 1968). This so-called Critical State model was originally meant to simulate the behaviour of (near-) normally consolidated clays under triaxial compression test conditions (Roscoe & Burland, 1968). Shortly after the introduction of the original Cam-Clay model (Roscoe, Schofield & Thurairajah, 1965), a modified flow rule was proposed by Burland (1965, 1967). Accordingly, the yield function changed from a logarithmic expression to a function that represents an ellipse in (p,q)-plane. The latter model is well known under the name Modified Cam-Clay. Roscoe and Burland (1968) showed how this model could be applied to general three-dimensional states of stress and strain. In the Cam-Clay model (both the original and modified form) it was primarily assumed that volumetric strains could be divided into an elastic and a plastic part, whereas deviatoric strains were assumed to be fully plastic. In later publications (Wroth & Zytynski, 1978) the generalized form of Hooke's law was used for stress paths in the elastic domain. So far most attention was paid to the *wet side* of the model (the hardening part). Considering the *dry side* of the model (the softening part), which is of interest for overconsolidated clays, it was observed that the softening behaviour was strongly overpredicted. Improvement on this point was achieved by the introduction of another yield surface for the dry side, known as the Hvorslev surface (Atkinson & Bransby, 1978). Since the introduction of Cam-Clay, many researchers have used this model as a basis for more complicated soil models (e.g. Adachi & Oka, 1982).

One of the basic assumptions of the Modified Cam-Clay model is that there is a logarithmic relation between the mean stress p and the void ratio e for isotropic stress paths. This relation is visualized by the solid line on the bottom plane in Figure 4.1, which is called the Normal Consolidation Line (NCL). The ultimate stress level ever reached on this line is called the isotropic preconsolidation stress p_c. During unloading and reloading up to the preconsolidation stress, a different line is followed.

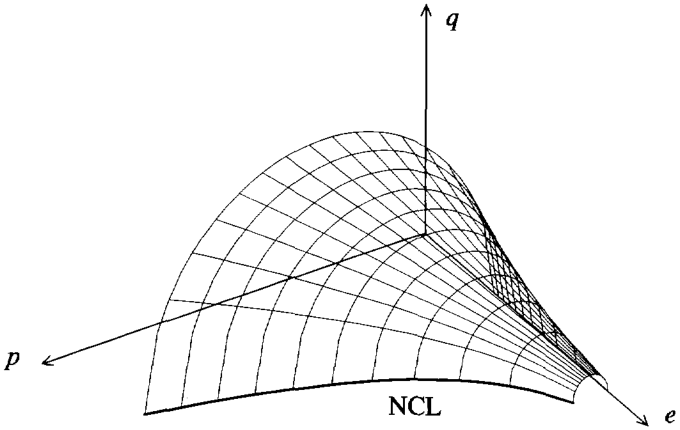

Figure 4.1 State boundary surface

When using a logarithmic scale for the p-axis, the NCL is a straight line with inclination λ, whereas the unloading / reloading line is a straight line with inclination κ. In fact, an infinite number of parallel unloading / reloading lines exist in (p,e)-plane, each corresponding to a particular value of p_c.

$$e - e^0 = -\lambda \ln\left[\frac{p}{p^0}\right] = -\lambda \ln\left[\frac{p_c}{p_c^0}\right] \qquad \text{virgin isotropic compression} \qquad (4.1a)$$

$$e - e^0 = -\kappa \ln\left[\frac{p}{p^0}\right] \qquad \text{isotropic unloading / reloading} \qquad (4.1b)$$

The parameters λ and κ are denoted as the compression index and the swelling index respectively. Differences in void ratio can be related to differences in volumetric strain, as already formulated in Equation 3.26. In general, changes in void ratio are quite small. In this study it is assumed that $\lambda / (1+e)$ is a constant, named λ^* (modified compression index). Indeed, there is some experimental evidence that λ^* is a constant, as many compression tests on clay show a linear relation between the logarithm of the stress and the relative settlement as a percentage of the original sample height. Similarly, for unloading / reloading the modified swelling index κ^* is introduced. Obviously, the ratio λ^*/κ^* is equal to the compression ratio λ/κ as used in some textbooks on critical state soil mechanics. On using the constants λ^* and κ^*, Equations 4.1 can be rewritten as:

$$\varepsilon_v - \varepsilon_v^0 = \lambda^* \ln\left[\frac{p}{p^0}\right] = \lambda^* \ln\left[\frac{p_c}{p_c^0}\right] \qquad \text{virgin isotropic compression} \qquad (4.2a)$$

$$\varepsilon_v^e - \varepsilon_v^{e0} = \kappa^* \ln\left[\frac{p}{p^0}\right] \qquad \text{isotropic unloading / reloading} \qquad (4.2b)$$

Unloading / reloading is considered as elastic behaviour, which explains the superscript e on the volumetric strains in Equation 4.2b. In rate form the above relationships yield:

$$\dot{\varepsilon}_v = \lambda^* \frac{\dot{p}}{p} \qquad \text{virgin isotropic compression} \qquad (4.3a)$$

$$\dot{\varepsilon}_v^e = \kappa^* \frac{\dot{p}}{p} \qquad \text{isotropic unloading / reloading} \qquad (4.3b)$$

The flow rule of the Modified Cam-Clay model is based on Burland's assumption that the ratio of the deviatoric plastic strain rate and the volumetric plastic strain rate in triaxial testing follows the rule (Burland, 1965):

$$\frac{\dot{\varepsilon}_s^p}{\dot{\varepsilon}_v^p} = \frac{2\, q/p}{M^2 - (q/p)^2} \qquad (4.4)$$

According to plasticity theory, plastic strain rates are written as:

$$\dot{\varepsilon}_v^p = \dot{\lambda} \frac{\partial g}{\partial p} \qquad (4.5a)$$

$$\dot{\varepsilon}_s^p = \dot{\lambda} \frac{\partial g}{\partial q} \qquad (4.5b)$$

where $\dot{\lambda}$ is the rate of the plastic multiplier, which should not be confused with the compression index λ or with the modified compression index λ^*, and g is the plastic potential function. Burland assumed the concept of associated plasticity. Hence, the yield function of the Modified Cam-Clay model is equal to the plastic potential function. In order to arrive at the flow rule of Equation 4.4, f and g are defined as:

$$f = g = \frac{q^2}{M^2} + p\,(p - p_c) \qquad (4.6)$$

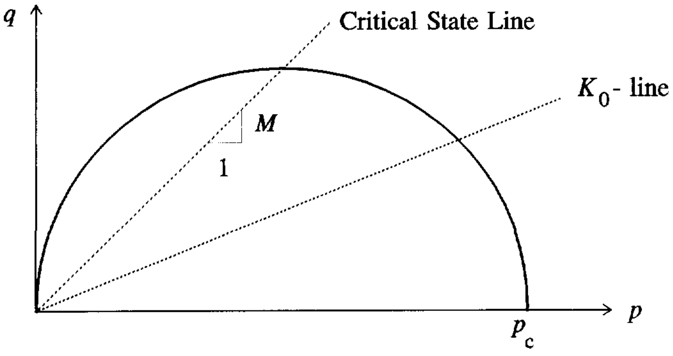

Figure 4.2 Yield surface of the Modified Cam-Clay model in (p,q)-plane

The yield surface $(f = 0)$ represents an ellipse in (p,q)-plane as visualised in Figure 4.2. In fact, an infinite number of ellipses exist, each corresponding to a particular value of p_c. All combinations of ultimate stress states, as defined by the yield surface, and related void ratios, form the so-called state boundary surface as represented in Figure 4.1.

In (p,q)-plane the tops of all ellipses form a line with inclination M through the origin. This line is denoted as the Critical State Line (CSL). The constant M determines the shape of the ellipse. In critical state conditions M is the ratio q over p and can thus be regarded as a friction constant.

The magnitude of the ellipse is determined by the isotropic preconsolidation stress p_c. The value of p_c is affected by plastic straining and follows from the hardening relation:

$$\varepsilon_v^p - \varepsilon_v^{p0} = (\lambda^* - \kappa^*) \ln \left[\frac{p_c}{p_c^0} \right] \tag{4.7}$$

In rate form:

$$\dot{\varepsilon}_v^p = (\lambda^* - \kappa^*) \frac{\dot{p}_c}{p_c} \qquad \text{or} \qquad \dot{p}_c = \frac{p_c}{\lambda^* - \kappa^*} \dot{\varepsilon}_v^p \tag{4.8}$$

According to the basic principle of elastoplasticity, strain rates are divided into an elastic part and a plastic part. For general states of stress, the relation between stress rates and elastic strain rates is assumed to be given by Hooke's law of elasticity, as formulated in Equation

2.5. Herewith, one arrives at the stress-strain relation as formulated in Equation 3.2, which is still valid in the case of hardening plasticity:

$$\dot{\underline{\sigma}} = \underline{\underline{D}}^e \, (\dot{\underline{\varepsilon}} - \dot{\underline{\varepsilon}}^p) \tag{3.2}$$

For the Modified Cam-Clay model, the elastic stiffness modulus G, occurring in the matrix $\underline{\underline{D}}^e$, is a tangential value that can be related to the swelling index κ^*:

$$G_t = \frac{3}{2} \, \frac{1-2\nu}{1+\nu} \, \frac{p}{\kappa^*} \tag{4.9}$$

The second elastic parameter in $\underline{\underline{D}}^e$, Poisson's ratio ν, is assumed to be a constant. Wroth and Houlsby (1985) report ν-values for clays in the range from 0.12 to 0.35.

As the flow rule in the Modified Cam-Clay model is associated, the plastic strain rates can be written as:

$$\dot{\underline{\varepsilon}}^p = \dot{\lambda} \, \frac{\partial f}{\partial \underline{\sigma}} \tag{4.10}$$

In the case of fully elastic behaviour, the rate of the plastic multiplier $\dot{\lambda}$ is zero. In the case of plastic behaviour, as defined in Equation 3.6b, $\dot{\lambda}$ is evaluated by applying Prager's consistency condition. For hardening models relation 3.7 is not sufficient. For the Modified Cam-Clay model the consistency condition can be formulated as:

$$\frac{\partial f}{\partial \underline{\sigma}}^T \dot{\underline{\sigma}} + \frac{\partial f}{\partial p_c} \dot{p}_c = 0 \tag{4.11}$$

Substitution of the hardening relation 4.8 with help of Equation 4.5a gives, after elaboration, an expression for the rate of the plastic multiplier:

$$\dot{\lambda} = \frac{1}{d+h} \, \frac{\partial f}{\partial \underline{\sigma}}^T \underline{\underline{D}}^e \, \dot{\underline{\varepsilon}} \qquad\qquad d = \frac{\partial f}{\partial \underline{\sigma}}^T \underline{\underline{D}}^e \, \frac{\partial f}{\partial \underline{\sigma}} \tag{4.12}$$

Note that the scalar d is not a constant such as in the Drucker-Prager model and the Mohr-Coulomb model, but a stress-dependent quantity. The hardening modulus h is in the current model defined as:

$$h = \frac{p_c}{\lambda^* - \kappa^*} \frac{\partial f}{\partial p} \frac{\partial f}{\partial p_c} \tag{4.13}$$

Back-substitution of Equation 4.12 into Equation 4.10 and successively into Equation 3.2 gives the full stress-strain relation:

$$\dot{\underline{\sigma}} = \left[\underline{\underline{D}}^e - \frac{1}{d+h} \underline{a}\, \underline{b}^T \right] \dot{\underline{\varepsilon}} \tag{4.14}$$

where

$$\underline{a} = \underline{\underline{D}}^e \frac{\partial f}{\partial \underline{\sigma}} \qquad\qquad \underline{b}^T = \frac{\partial f^T}{\partial \underline{\sigma}} \underline{\underline{D}}^e \tag{4.15}$$

4.2 The coefficient of lateral earth pressure for normally consolidated soil

The coefficient of earth pressure at rest, K_0, is mainly determined by the friction angle of the soil and by the amount of overconsolidation. For a normally consolidated soil, K_0 can well be approximated by the experimental formula: $K_0^{nc} = 1 - \sin\varphi$ (Jaky, 1944). Simulation of a one-dimensional compression test (oedometer test) using the Modified Cam-Clay model shows that K_0^{nc} is indeed highly influenced by the friction constant M. However, on choosing a value of M that gives the correct shearing resistance, the value of K_0^{nc} will exceed the value resulting from Jaky's formula. In order to arrive at an appropriate value, the friction constant should be increased substantially, but in that case the shearing strength is overpredicted (Brinkgreve & Vermeer, 1992). This is one of the discrepancies of the Modified Cam-Clay model. In the remainder of this section the superscript nc is omitted when considering normally consolidated K_0-values.

In order to establish a relation between the friction constant M and the value of K_0, the conditions for an oedometer test are further examined. The basic condition is:

$$\dot{\varepsilon}_{zz} = \dot{\varepsilon}_{xx} = 0 \qquad\qquad \dot{\gamma}_{xy} = 0 \tag{4.16}$$

Moreover, from the model it follows that:

$$\dot{\sigma}_{xx} = \dot{\sigma}_{zz} = K_0\ \dot{\sigma}_{yy} \qquad \dot{\sigma}_{xy} = 0 \tag{4.17a}$$

$$\dot{\varepsilon}^e_{xx} = \dot{\varepsilon}^e_{zz} \qquad \dot{\gamma}^e_{xy} = 0 \tag{4.17b}$$

$$\dot{\varepsilon}^p_{xx} = \dot{\varepsilon}^p_{zz} \qquad \dot{\gamma}^p_{xy} = 0 \tag{4.17c}$$

Only two relevant stress components, σ_{xx} and σ_{yy}, and two relevant strain components, ε_{xx} and ε_{yy}, remain. According to Hooke's law, the elastic strain components can be written as:

$$\dot{\varepsilon}^e_{xx} = \frac{1}{E}\left[(1-\nu)\ \dot{\sigma}_{xx} - \nu\ \dot{\sigma}_{yy}\right] \tag{4.18a}$$

$$\dot{\varepsilon}^e_{yy} = \frac{1}{E}\left[-2\ \nu\ \dot{\sigma}_{xx} + \dot{\sigma}_{yy}\right] \tag{4.18b}$$

Using Equation 4.17a, the horizontal elastic strain rate can be related to the vertical elastic strain rate:

$$\dot{\varepsilon}^e_{xx} = \frac{K_0\ (1-\nu) - \nu}{1 - 2\,\nu K_0}\ \dot{\varepsilon}^e_{yy} \tag{4.19}$$

On the conditions as defined in Equations 4.16 and 4.17 and from Equations 4.3 it follows respectively that:

$$\frac{\dot{\varepsilon}_v}{\dot{\varepsilon}^e_v} = \frac{\dot{\varepsilon}_{yy}}{2\,\dot{\varepsilon}^e_{xx} + \dot{\varepsilon}^e_{yy}} = \frac{1-2\,\nu K_0}{(1-2\nu)(1+2K_0)}\ \frac{\dot{\varepsilon}_{yy}}{\dot{\varepsilon}^e_{yy}} \qquad \frac{\dot{\varepsilon}_v}{\dot{\varepsilon}^e_v} = \frac{\lambda^*}{\kappa^*} \tag{4.20}$$

From the above relations and from the basic principle of elastoplasticity to split strain rates into an elastic and a plastic component, it follows that:

$$\dot{\varepsilon}_{yy} = \frac{(1-2\nu)(1+2K_0)}{1-2\,\nu K_0}\ \frac{\lambda^*}{\kappa^*}\ \dot{\varepsilon}^e_{yy} \tag{4.21}$$

$$\dot{\varepsilon}^p_{yy} = \left[\frac{(1-2\nu)(1+2K_0)}{1-2\,\nu K_0}\ \frac{\lambda^*}{\kappa^*} - 1\right]\dot{\varepsilon}^e_{yy} \tag{4.22}$$

$$\dot{\varepsilon}^p_{xx} = -\dot{\varepsilon}^e_{xx} = -\frac{K_0\ (1-\nu) - \nu}{1 - 2\,\nu K_0}\ \dot{\varepsilon}^e_{yy} \tag{4.23}$$

Using Equations 4.22 and 4.23, all elastic and plastic strain rate components can be related to the vertical elastic strain rate. Reformulation in terms of the strain rates as used in the flow rule 4.4 gives:

$$\dot{\varepsilon}_s^p = \tfrac{2}{3}(\dot{\varepsilon}_{xx}^p - \dot{\varepsilon}_{yy}^p) = -\tfrac{2}{3}\left[\frac{(1-2\nu)(1+2K_0)\lambda^*/\kappa^* - (1+\nu)(1-K_0)}{1-2\nu K_0}\right]\dot{\varepsilon}_{yy}^e \tag{4.24a}$$

$$\dot{\varepsilon}_v^p = -2\,\dot{\varepsilon}_{xx}^p - \dot{\varepsilon}_{yy}^p = -\left[\frac{(1-2\nu)(1+2K_0)(\lambda^*/\kappa^* - 1)}{1-2\nu K_0}\right]\dot{\varepsilon}_{yy}^e \tag{4.24b}$$

Elaboration of the flow rule requires the stress ratio q over p, which can be formulated under the current conditions as:

$$q/p = \frac{3\,(1-K_0)}{1+2K_0} \tag{4.25}$$

Substitution of Equations 4.24 and 4.25 into the flow rule gives after elaboration:

$$M = 3\sqrt{\frac{(1-K_0)^2}{(1+2K_0)^2} + \frac{(1-K_0)\,(1-2\nu)\,(\lambda^*/\kappa^* - 1)}{(1+2K_0)(1-2\nu)\lambda^*/\kappa^* - (1-K_0)(1+\nu)}} \tag{4.26}$$

Apart from the M-value, K_0 also depends on the compression ratio λ^*/κ^* and on Poisson's ratio ν. Conversely, in order to simulate the proper K_0-value, the compression ratio and Poisson's ratio influence the choice of M. Figures 4.3 show the value of M according to Equation 4.26 for K_0-values ranging from 0.3 to 0.9 and for values of λ^*/κ^* ranging from 1.5 to 9.5. From these plots it can be seen that the influence of K_0 on M is dominant.

In a previous study, Brinkgreve and Vermeer (1992) proposed a non-linear approximation for the relation between K_0 and M, namely $M = (1.6\text{-}K_0) / (0.2+K_0)$. However, from Figures 4.3 it can be seen that, especially in the area of most common values, i.e. for $0.4 \le K_0 \le 0.6$ and $3.0 \le \lambda^*/\kappa^* \le 6.0$, the relation between M and K_0 is nearly linear. In this thesis a new approximation is proposed, which is even more simple and at least just as accurate as the previous approximation:

$$M \approx 3.0 - 2.8\,K_0 \tag{4.27}$$

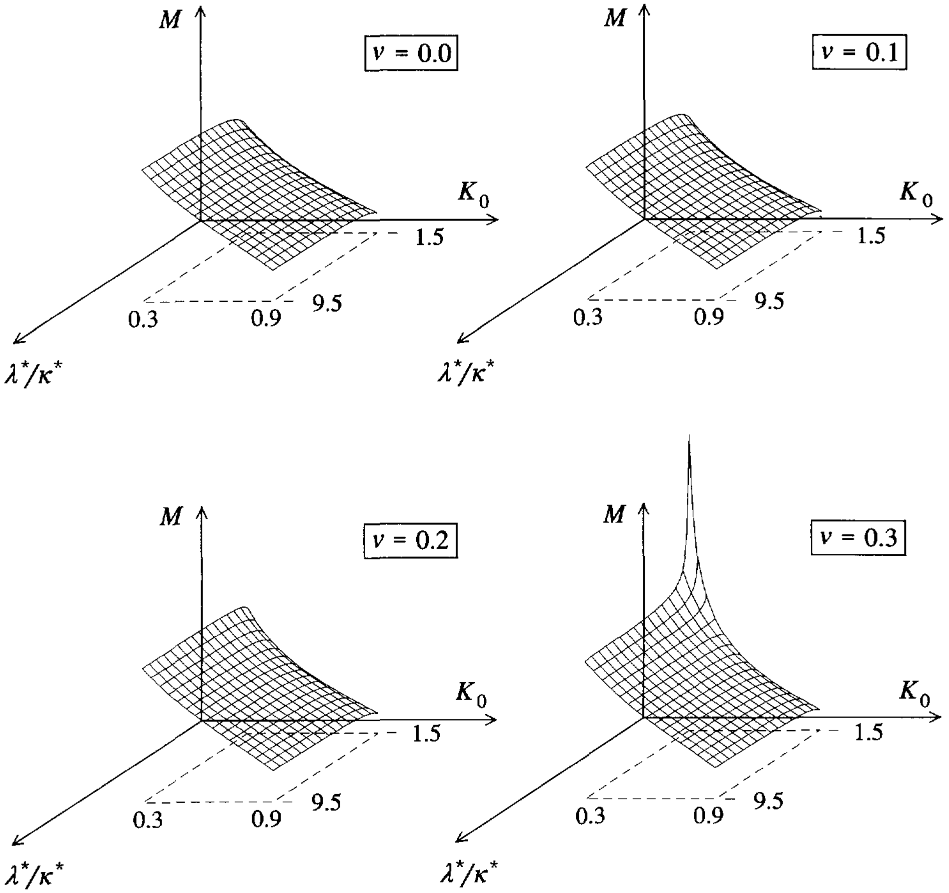

Figure 4.3 Visualisation of M as a function of K_0 and λ^*/κ^* for different ν's
For $\lambda^*/\kappa^* = 5$: $M_{min} = 0.5$, $M_{max} = 2.3$

The error in M, i.e. the difference between Equation 4.27 and Equation 4.26, is shown in Figure 4.4 for $\nu = 0.2$. From this plot it can be seen that for low values of K_0 the M-value is underestimated and thus the resulting K_0 is too large. For low values of λ^*/κ^* the M-value is overestimated and thus the resulting K_0 is too small. In the area of most common values, the maximum error in M is 0.1 and the maximum difference in K_0 is 0.03. From these values it can be concluded that the approximation 4.27 is reasonably accurate.

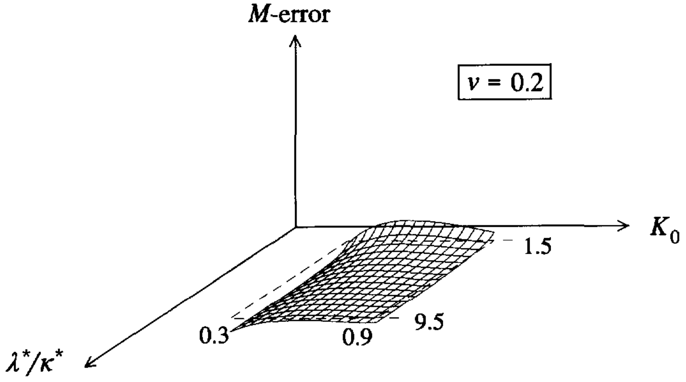

Figure 4.4 Error in M when using the approximation 4.27
Minimum M-error = -0.2, Maximum M-error = 0.3

Consider a material with a friction angle of 20°, λ^*/κ^* equal to 5.0 and Poisson's ratio 0.2. According to Jaky's formula, K_0 is estimated at 0.66. Equation 4.26 yields an M-value of 1.15. In order to simulate failure in a triaxial compression stress path correctly, the value of M should be $6 \sin\varphi$ / $(3-\sin\varphi)$, which gives $M = 0.77$. With this M-value the resulting K_0 is 0.80 and not 0.66 as suggested by the empirical formula. In fact, the Modified Cam-Clay model predicts relatively large K_0-values. Better K_0-values would be obtained when using relatively large values of M, but this would result in much too high shearing strengths. Indeed, it is not possible to simulate both an oedometer stress path and a full triaxial compression stress path with good accuracy using the same value of M.

4.3 The Plaxis Cap model

The anomaly as described in the previous section can simply be improved by the introduction of an additional yield function for describing failure. The Modified Cam-Clay yield surface is retained, but only used as a cap on the failure surface. The shape of the cap, given by the M-value, is such that the model predicts a correct K_0-path, whereas the failure surface ensures a correct shearing strength. In the current model, named the Plaxis Cap model, the two yield functions are formulated as:

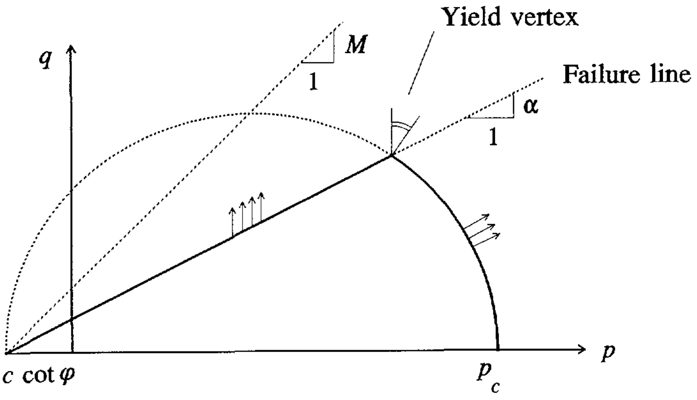

Figure 4.5 Yield surface of the Plaxis Cap model in (p,q)-plane

$$f_1 = \frac{q^2}{M^2} + p^* (p^* - p_c^*) \qquad \text{(hardening cap)} \tag{4.28a}$$

$$f_2 = q - \alpha p^* \qquad \text{(failure cone)} \tag{4.28b}$$

where

$$p^* = p + c \cot\varphi \qquad p_c^* = p_c + c \cot\varphi \tag{4.29}$$

The full yield criterion in (p,q)-plane is visualised in Figure 4.5. The M-line must be steeper than the α-line, which corresponds with the general finding as discussed in the previous section.

The flow rule for cap yielding remains associated, whereas a non-associated flow rule is adopted for failure. The plastic potential functions are defined as respectively:

$$g_1 = f_1 \tag{4.30a}$$

$$g_2 = q - \beta p^* \tag{4.30b}$$

The parameter β in the latter function is a dilatancy coefficient. For a particular value of p_c the two yield functions intersect in the point:

$$(p\,,q) \;=\; \left[\frac{p_c \,-\, (\alpha^2 / M^2)\; c\; \cot\varphi}{1 \,+\, \alpha^2 / M^2} \;,\; \frac{\alpha\; (p_c \,+\, c\; \cot\varphi)}{1 \,+\, \alpha^2 / M^2} \right] \tag{4.31}$$

It should be noted that the inclusion of a cohesion term $(c > 0)$ does not lead to a constant stress ratio $q\,/\,p$ in one-dimensional compression, but to a constant ratio $q\,/\,p^*$ instead.

Besides the introduction of a second yield function, the logarithmic swelling law is generalized to a power law as introduced in Section 2.2. Therefore, the formulation of the tangential stiffness modulus, as expressed in Equation 2.10, is utilized and repeated here for convenience in terms of the bulk modulus:

$$K_t \;=\; K^{ref} \left[\frac{p^*}{p^{ref}} \right]^m \tag{4.32}$$

In this expression K^{ref} is a reference bulk modulus for a particular stress level p^{ref} (usually 100 kPa). For a power m equal to 1.0, the logarithmic compression law is retrieved. In that case:

$$\frac{K^{ref}}{p^{ref}} \;=\; \frac{1}{\kappa^*} \qquad\qquad (m \,=\, 1.0) \tag{4.33}$$

In any other case $(m \neq 1)$ the meaning of κ^* is lost. However, the compression ratio λ^*/κ^* has still a physical meaning, as it reflects the ratio of total volumetric strain over reversible volumetric strain in isotropic compression.

The hardening relation of the Plaxis Cap model is defined in rate form by:

$$\dot{\varepsilon}_v^p \;=\; \frac{\lambda^* / \kappa^* \;-\; 1}{K^{ref}} \left[\frac{p^{ref}}{p_c^*} \right]^m \dot{p}_c \tag{4.34}$$

In the special case of $m \,=\, 1$ and $c \,=\, 0,$ the current hardening relation is equal to that of the Modified Cam-Clay model, as defined in Equation 4.8.

For a further treatment of the model, the reader is referred to Section 5.4, where the time integration is extensively discussed, and to Chapter 6, where the model is applied to practical problems. In the following section, the stiffness behaviour is analysed for different stress paths.

4.4 Comparison of tangential shear moduli for different stress paths

In order to evaluate the stiffness behaviour of the Plaxis Cap model for a normally K_0-consolidated material in different stress paths, a tangential shear modulus is introduced, defined as (Brinkgreve et al., 1994):

$$G_t^* = \frac{1}{2} \frac{|\dot{\sigma}_1 - \dot{\sigma}_3|}{|\dot{\varepsilon}_1 - \dot{\varepsilon}_3|} \tag{4.35}$$

Note that the current tangential shear modulus is not an elastic parameter such as defined in Equation 4.9, but an equivalent elastoplastic shear modulus. For the material as introduced at the end of the Section 4.2, the value of G_t^* is evaluated for six different stress paths, which are listed below and plotted in Figure 4.6a. A complete set of model parameters is listed in Table 4.1. Except for the cohesion, the model parameters are based on the practical application as described in Section 6.3.

1.	Oedometer loading	$\dot{\varepsilon}_2 = \dot{\varepsilon}_3 = 0$	$G_t^* = 110$ kPa
2.	Drained axial loading	$\dot{\sigma}_2 = \dot{\sigma}_3 = 0$	$G_t^* = 270$ kPa
3.	Undrained axial loading	$\dot{\varepsilon}_v = 0$	$G_t^* = 902$ kPa
4.	Constant stress ratio unloading	$d(\sigma_1/\sigma_3) = 0$	$G_t^* = 1933$ kPa
5.	Drained axial unloading	$\dot{\sigma}_2 = \dot{\sigma}_3 = 0$	$G_t^* = 1933$ kPa
6.	Radial loading	$\dot{\sigma}_1 = 0$	$G_t^* = 1933$ kPa

Table 4.1. Model parameters of material under consideration

Parameter	Symbol	Value	Unit
Soil weight	γ	14.0	kN/m^3
Swelling index	κ^*	0.03	-
Compression index	λ^*	0.15	-
Poisson's ratio	ν	0.2	-
Friction angle	φ	20	°
Cohesion	c	1.0	kPa
Coef. lateral earth press.	K_0	0.66	-
Tangent of CSL	M	1.1	-

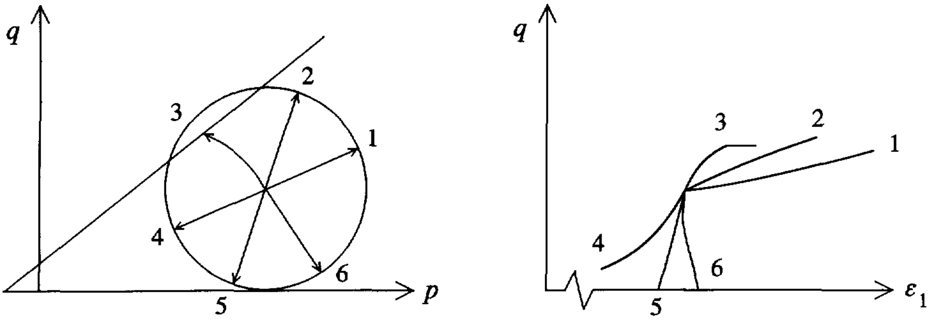

Figure 4.6 Continuing stress paths from K_0 consolidated material
a. Stress paths b. Stress-strain curves

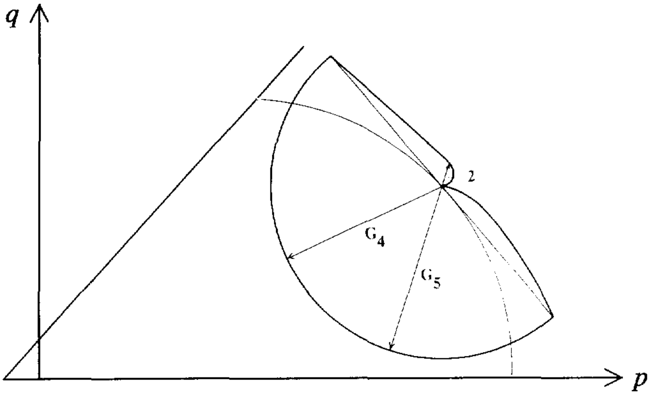

Figure 4.7 Stress-path dependent tangential shear moduli obtained from Plaxis Cap model

The development of the stiffness along the stress paths can be seen from Figure 4.6b. A full fan of tangential shear moduli is presented in Figure 4.7. In this graph G_t^* is plotted radially from the starting stress point in (p,q)-plane. From this plot it can be concluded that the stiffness differences can be very large. In general, compressive stress paths give a lower stiffness than deviatoric stress paths. For all stress paths into the elastic domain, the tangential stiffness is the same.

From the analysis it is concluded that the Plaxis Cap model, or a hardening model in general, shows a stiffness behaviour that is very different from, for example, elastic models (Section 2.2 to 2.4) or the Duncan-Chang model (Section 2.5) or the Mohr-Coulomb model (Section 3.2), at least when considering a normally consolidated material. A non-cap-hardening model may show a stress-dependent stiffness behaviour, such as in the Duncan-Chang model, but for a given stress state the stiffness is constant and independent of the stress path that is followed. Using a hardening model, the stiffness can vary a lot for a given stress state, depending on the stress path that is followed.

4.5 Overconsolidated stress states

The amount of overconsolidation is the difference between the preconsolidation stress and the current stress state. In geotechnical engineering practice it is more appropriate to use the vertical preconsolidation stress σ_c than the isotropic preconsolidation stress p_c. For the Modified Cam-Clay model or the Plaxis Cap model without cohesion, the relation between these two types of preconsolidation stress is easy to derive, assuming that at the stress level of preconsolidation the soil is normally K_0 consolidated. In that case p_c can be evaluated from the condition $f = 0$ (Equation 4.6), which gives:

$$p_c = p + \frac{q^2}{M^2\, p} \tag{4.36}$$

At the preconsolidation stress level the stresses can be formulated as:

$$\sigma_{yy} = \sigma_c \qquad \sigma_{xx} = \sigma_{zz} = K_0\, \sigma_c \tag{4.37}$$

Or in terms of p and q:

$$p = -\tfrac{1}{3}\,(1 + 2K_0)\,\sigma_c \qquad q = -(1 - K_0)\,\sigma_c \tag{4.38}$$

Substitution into Equation 4.36 and elaboration gives the required relation:

$$\sigma_c = -\frac{M^2\,(1 + 2K_0)}{\frac{1}{3}\,M^2\,(1 + 2K_0)^2 + 3\,(1 - K_0)^2}\; p_c \tag{4.39}$$

In overconsolidated soils the coefficient of lateral earth pressure is larger than for normally consolidated soils. This effect can well be simulated with Cam-Clay type models. Consider an oedometer test, preloaded to $\sigma_{yy} = \sigma_c$ and subsequently unloaded to $\sigma_{yy} = \sigma_{yy}{}^0$. During unloading the sample behaves elastically and the incremental stress ratio is, according to Hooke's law, given by:

$$\frac{\Delta\sigma_{xx}}{\Delta\sigma_{yy}} = \frac{K_0\ \sigma_c - \sigma_{xx}^0}{\sigma_c - \sigma_{yy}^0} = \frac{K_0\ OCR\ \sigma_{yy}^0 - \sigma_{xx}^0}{(OCR - 1)\ \sigma_{yy}^0} = \frac{\nu}{1-\nu} \tag{4.40}$$

where K_0 is the stress ratio in normal consolidation and OCR is the overconsolidation ratio, defined as:

$$OCR = \sigma_c \ / \ \sigma_{yy}^0 \tag{4.41}$$

Hence, the stress ratio of the overconsolidated soil sample is given by:

$$\frac{\sigma_{xx}^0}{\sigma_{yy}^0} = K_0\ OCR - \frac{\nu}{1-\nu}\ (OCR - 1) \tag{4.42}$$

Note that Equation 4.42 is only valid in the elastic domain, because the formula was derived from elasticity theory. If a soil sample is drastically unloaded, resulting in a high degree of overconsolidation, the stress ratio will be influenced by plasticity. Other formulas for the stress ratio in overconsolidated soils were proposed in the past based on experimental results, such as the empirical formula by Schmidt (1966):

$$\frac{\sigma_{xx}^0}{\sigma_{yy}^0} = K_0\ \ OCR^m \tag{4.43}$$

On reviewing this formula, Ladd et al. (1977) report values of m of about 0.4. Comparison of formulas 4.42 and 4.43 with $m = 0.4$ shows that similar overconsolidated stress ratios are obtained when using a Poisson's ratio ν of the order of 0.3. A small variation is obtained in the sense that a larger friction angle (and thus a smaller K_0) or a smaller overconsolidation ratio gives a slightly smaller Poisson's ratio, and vice versa. The order of 0.3 is relatively large when considering the range $0.12 < \nu < 0.35$ as put forward by Wroth & Houlsby (1985). Further data on this matter would be needed in order to arrive at definite conclusions with respect to the most appropriate value of ν.

5 FORMULATION AND SOLUTION OF THE BOUNDARY VALUE PROBLEM

In this chapter the basic equations for the quasi-static deformation of a soil body are formulated according to the theory of continuum mechanics. A restriction is made in the sense that deformations are considered to be small. This enables a description with reference to the original undeformed geometry. The continuum description is discretized according to the finite element method. The major part of this chapter is devoted to the integration of stress rates with respect to time.

5.1 General equations of continuum theory

The static equilibrium of a continuum can be formulated as:

$$\underline{\underline{L}}^T \, \underline{\sigma} + \underline{p} = \underline{0} \tag{5.1}$$

This equation relates the spatial derivatives of the six stress components, assembled in vector $\underline{\sigma}$, to the three components of the body forces, assembled in vector $\underline{p}$. $\underline{\underline{L}}^T$ is the transpose of a differential operator, defined as:

$$\underline{\underline{L}}^T = \begin{bmatrix} \frac{\partial}{\partial x} & 0 & 0 & \frac{\partial}{\partial y} & 0 & \frac{\partial}{\partial z} \\ 0 & \frac{\partial}{\partial y} & 0 & \frac{\partial}{\partial x} & \frac{\partial}{\partial z} & 0 \\ 0 & 0 & \frac{\partial}{\partial z} & 0 & \frac{\partial}{\partial y} & \frac{\partial}{\partial x} \end{bmatrix} \tag{5.2}$$

In addition to the equilibrium equation, the kinematic relation can be formulated as:

$$\underline{\varepsilon} = \underline{\underline{L}} \, \underline{u} \tag{5.3}$$

This equation expresses the six strain components, assembled in vector $\underline{\varepsilon}$, as the spatial derivatives of the three displacement components, assembled in vector $\underline{u}$, using the previously defined differential operator $\underline{\underline{L}}$. The link between Equation 5.1 and 5.3 is formed by a constitutive relation representing the material behaviour. Constitutive relations, i.e. relations between rates of stress and strain, were extensively discussed in Chapters 2 to 4. The general relation is repeated here for completeness.

$$\dot{\underline{\sigma}} = \underline{\underline{M}}\,\dot{\underline{\varepsilon}} \tag{5.4}$$

The combination of Equations 5.1, 5.3 and 5.4 would lead to a second-order partial differential equation in the displacements $\underline{u}$. However, instead of a direct combination, the equilibrium equation is reformulated in a weak form according to Galerkin's variation principle (see among others Zienkiewicz, 1971).

$$\int \delta\underline{u}^T\,(\underline{\underline{L}}^T\,\underline{\sigma} + \underline{p})\,dV = \underline{0} \tag{5.5}$$

In this formulation $\delta\underline{u}$ represents a kinematically admissible variation of displacements. Applying Green's theorem for partial integration on the first term in Equation 5.5 leads to:

$$\int \delta\underline{\varepsilon}^T\,\underline{\sigma}\,dV = \int \delta\underline{u}^T\,\underline{p}\,dV + \oint \delta\underline{u}^T\,\underline{t}\,dS \tag{5.6}$$

This introduces a boundary integral in which the boundary traction appears. The three components of the boundary traction are assembled in the vector $\underline{t}$. Equation 5.6 is referred to as the virtual work equation.

The development of the stress state $\underline{\sigma}$ can be regarded as an incremental process:

$$\underline{\sigma}^i = \underline{\sigma}^{i-1} + \Delta\underline{\sigma} \qquad\qquad \Delta\underline{\sigma} = \int \dot{\underline{\sigma}}\,d\tau \tag{5.7}$$

In this relation $\underline{\sigma}^i$ represents the actual state of stress which is unknown and $\underline{\sigma}^{i-1}$ represents the previous state of stress which is known. The stress increment $\Delta\underline{\sigma}$ is the stress rate integrated over a small time increment.

If Equation 5.6 is considered for the actual state i, the unknown stresses $\underline{\sigma}^i$ can be eliminated using Equation 5.7:

$$\int \delta\underline{\varepsilon}^T\,\Delta\underline{\sigma}\,dV = \int \delta\underline{u}^T\,\underline{p}^i\,dV + \oint \delta\underline{u}^T\,\underline{t}^i\,dS - \int \delta\underline{\varepsilon}^T\,\underline{\sigma}^{i-1}\,dV \tag{5.8}$$

It should be noted that all quantities appearing in the Equations 5.1 to 5.8 are functions of the position in three-dimensional space.

5.2 Finite element discretization

According to the finite element method a continuum is divided into a number of (volume) elements. Each element consists of a number of nodes. Each node has a number of degrees-of-freedom that correspond to discrete values of the unknowns in the boundary value problem to be solved. In the present case of deformation theory the degrees-of-freedom correspond to the displacement components. Within an element the displacement field $\underline{u}$ is obtained from the discrete nodal values in a vector $\underline{v}$ using interpolation functions assembled in matrix $\underline{\underline{N}}$:

$$\underline{u} = \underline{\underline{N}}\, \underline{v} \tag{5.9}$$

The interpolation functions in matrix $\underline{\underline{N}}$ are often denoted as shape functions. Substitution of Equation 5.9 in the kinematic relation 5.3 gives:

$$\underline{\varepsilon} = \underline{\underline{L}}\, \underline{\underline{N}}\, \underline{v} = \underline{\underline{B}}\, \underline{v} \tag{5.10}$$

In this relation $\underline{\underline{B}}$ is the strain interpolation matrix and contains the spatial derivatives of the interpolation functions. Equations 5.9 and 5.10 can be used in variational, incremental and rate form as well.

Equation 5.8 can now be reformulated in discretized form as:

$$\int (\underline{\underline{B}}\, \delta\underline{v})^T \Delta\underline{\sigma}\, dV = \int (\underline{\underline{N}}\, \delta\underline{v})^T \underline{p}^i\, dV + \oint (\underline{\underline{N}}\, \delta\underline{v})^T \underline{t}^i\, dS - \int (\underline{\underline{B}}\, \delta\underline{v})^T \underline{\sigma}^{i-1}\, dV \tag{5.11}$$

The discrete displacements can be placed outside the integral:

$$\delta\underline{v}^T \int \underline{\underline{B}}^T \Delta\underline{\sigma}\, dV = \delta\underline{v}^T \int \underline{\underline{N}}^T \underline{p}^i\, dV + \delta\underline{v}^T \oint \underline{\underline{N}}^T \underline{t}^i\, dS - \delta\underline{v}^T \int \underline{\underline{B}}^T \underline{\sigma}^{i-1}\, dV \tag{5.12}$$

Provided that Equation 5.12 holds for any kinematically admissible displacement variation $\delta\underline{v}^T$, the equation can be written as:

$$\int \underline{\underline{B}}^T \Delta\underline{\sigma}\, dV = \int \underline{\underline{N}}^T \underline{p}^i\, dV + \oint \underline{\underline{N}}^T \underline{t}^i\, dS - \int \underline{\underline{B}}^T \underline{\sigma}^{i-1}\, dV \tag{5.13}$$

The above equation is the elaborated equilibrium condition in discretized form. The first term at the right-hand side together with the second term represent the current external force vector and the last term represents the internal reaction vector from the previous step. A difference between the external force vector and the internal reaction vector should be balanced by a stress increment $\Delta\underline{\sigma}$.

The relation between stress increments and strain increments is usually non-linear. As a result, strain increments can generally not be calculated directly, and global iterative procedures are required to satisfy the equilibrium condition 5.13 for all material points. Global iterative procedures are described later in Section 5.5, but the attention is first focused on the (local) integration of stresses.

5.3 Implicit integration of differential plasticity models

The stress increments $\Delta\underline{\sigma}$ are obtained by integration of the stress rates according to Equation 5.7. For differential plasticity models the stress increments can generally be written as:

$$\Delta\underline{\sigma} = \underline{\underline{D}}^e \left(\Delta\underline{\varepsilon} - \Delta\underline{\varepsilon}^p\right) \tag{5.14}$$

In this relation $\underline{\underline{D}}^e$ represents the elastic material matrix for the current stress increment. For material models containing a non-linear elastic part, such as described in Section 2.2 to 2.4, the matrix $\underline{\underline{D}}^e$ depends on the new, and yet unknown, stress state. As a result, the stress increment cannot directly be obtained from the strain increment, as suggested by Equation 5.14, and involves a more extended procedure. The stress integration of non-linear elastic models is treated in more detail in the Section 5.4.1.

The strain increments $\Delta\underline{\varepsilon}$ in the above relation are obtained from the displacement increments $\Delta\underline{v}$ using the strain interpolation matrix $\underline{\underline{B}}$, similar to Equation 5.10. For elastic material behaviour as defined by Equation 3.6a, the plastic strain increment $\Delta\underline{\varepsilon}^p$ is zero. For plastic material behaviour, as defined by Equation 3.6b, the plastic strain increment can be written, according to Vermeer (1979), as:

$$\Delta\underline{\varepsilon}^p = \Delta\lambda \left[(1 - \omega) \left[\frac{\partial g}{\partial \underline{\sigma}}\right]^{i-1} + \omega \left[\frac{\partial g}{\partial \underline{\sigma}}\right]^{i} \right] \tag{5.15}$$

In this equation $\Delta\lambda$ is the increment of the plastic multiplier and ω is a parameter indicating the type of time integration. For $\omega = 0$ the integration is called explicit and for $\omega = 1$ the integration is called implicit.

Vermeer (1979) has shown that the use of implicit integration $(\omega = 1)$ has some major advantages, as it overcomes the requirement to update the stress to the yield surface in the case of a transition from elastic to elastoplastic behaviour. Moreover, it can be proven that implicit integration, under certain conditions, leads to a symmetric and positive differential matrix $\partial \underline{\varepsilon} / \partial \underline{\sigma}$, which has a positive influence on iterative procedures. Because of these major advantages, restriction is made in this study to implicit integration and no attention is given to other types of time integration.

Hence, for $\omega = 1$ Equation 5.15 reduces to:

$$\Delta \underline{\varepsilon}^p = \Delta\lambda \left[\frac{\partial g}{\partial \underline{\sigma}} \right]^i \tag{5.16}$$

Substitution of Equation 5.16 into 5.14 and successively into Equation 5.7 gives:

$$\underline{\sigma}^i = \underline{\sigma}^{tr} - \Delta\lambda \, \underline{\underline{D}}^e \left[\frac{\partial g}{\partial \underline{\sigma}} \right]^i \qquad \underline{\sigma}^{tr} = \underline{\sigma}^{i-1} + \underline{\underline{D}}^e \, \Delta \underline{\varepsilon} \tag{5.17}$$

In this relation $\underline{\sigma}^{tr}$ is an auxiliary stress vector, referred to as the *elastic stresses* or *trial stresses*, which is the new stress state when considering purely linear elastic material behaviour.

The increment of the plastic multiplier $\Delta\lambda$, as used in Equation 5.17, can be solved from the condition that the new stress state has to satisfy the yield condition:

$$f(\underline{\sigma}^i) = 0 \tag{5.18}$$

For perfectly-plastic and linear hardening models the increment of the plastic multiplier can be written as:

$$\Delta\lambda = \frac{f(\underline{\sigma}^{tr})}{d + h} \tag{5.19}$$

where

$$d = \left[\frac{\partial f}{\partial \underline{\sigma}} \right]^{\underline{\sigma}^{tr}} \underline{\underline{D}}^e \left[\frac{\partial g}{\partial \underline{\sigma}} \right]^i \tag{5.20}$$

The symbol h denotes the hardening parameter, which is zero for perfectly-plastic models and constant for linear hardening models. In the latter case the new stress state can be formulated as:

$$\underline{\sigma}^{i} = \underline{\sigma}^{tr} - \frac{\left\langle f(\underline{\sigma}^{tr}) \right\rangle}{d + h} \, \underline{\underline{D}}^{e} \left[\frac{\partial g}{\partial \underline{\sigma}} \right]^{i} \tag{5.21}$$

The $\langle \, \rangle$ -brackets are referred to as McCauley brackets, which have the following convention:

$\langle x \rangle = 0$ for $x \leq 0$

$\langle x \rangle = x$ for $x > 0$

Note that for general non-linear hardening models the scalars d and h are stress-dependent. In that case evaluation of Equation 5.19 based on the trial stresses gives only an approximated value for the increment of the plastic multiplier. A proper solution is obtained by performing a local iteration process on $\Delta\lambda$ in order to satisfy the yield condition according to Equation 5.18. Such a process is described in Section 5.4.2.

5.4 Solving non-linear stress-strain relations

The solution of highly non-linear stress-strain relations, as for instance formulated in the Plaxis Cap model, involves extensions of the general procedure as described in the previous section. In the following sub-sections some aspects of stress integration for such models are considered. The description is based on the Plaxis Cap model, but the procedures can be used for some other models as well. Distinction is made between the non-linear elastic part, the non-linear hardening part and the point of combined yielding, i.e. the yield vertex that appears when both yield functions contribute to plastic straining.

In the Plaxis Cap model, the isotropic stress components include a cohesion term $c \cot\varphi$, indicated with the superscript $*$. For clarity the $*$ is omitted in the remainder of this chapter. It should be noted that any reference to p or p_c is intended to include the term $c \cot\varphi$ as well.

5.4.1 The non-linear elastic part

The elastic stiffness in the Plaxis Cap model depends on the mean stress p. The time integration of the mean stress can be formulated as:

$$\int \dot{p} \, d\tau = \int K_t \, \dot{\varepsilon}_v^e \, d\tau \tag{5.22}$$

In case of elasticity the elastic strain rates are equal to the total strain rates. Substitution of the tangential (stress dependent) bulk modulus as defined in Equation 4.32 and reformulation leads to:

$$\int \frac{\dot{p}}{p^m} \, d\tau = \int \frac{K^{ref}}{(p^{ref})^m} \, \dot{\varepsilon}_v \, d\tau \tag{5.23}$$

Evaluation of the integrals for time-step i and elaboration gives:

$$p^i = \left[(p^{i-1})^{1-m} + (1-m) \, \frac{K^{ref}}{(p^{ref})^m} \, \Delta\varepsilon_v \right]^{\frac{1}{1-m}} \tag{5.24}$$

Reformulated in terms of the strain increment gives:

$$\Delta\varepsilon_v = \frac{1}{1-m} \, \frac{(p^{ref})^m}{K^{ref}} \left[(p^i)^{1-m} - (p^{i-1})^{1-m} \right] \tag{5.25}$$

In the limiting case of $m = 1$ the above relation turns into the logarithmic expression of Equation 2.12. From Equation 5.24 or 5.25 (or in case $m = 1$ the corresponding logarithmic expressions) a representative bulk modulus can be formulated:

$$K^* = \frac{p^i - p^{i-1}}{\Delta\varepsilon_v} \tag{5.26}$$

This bulk modulus, which differs from the tangential bulk modulus K_t, is to be used in the elastic material matrix $\underline{\underline{D}}^e$ to calculate the new Cartesian stresses.

Only one of the formulations 5.24 or 5.25 will actually be used. Equation 5.24 relates to the initial stress method where the strain increment is iteratively adapted to the stress. Equation 5.25 relates to the initial strain method where the stress is adapted to the strain increment.

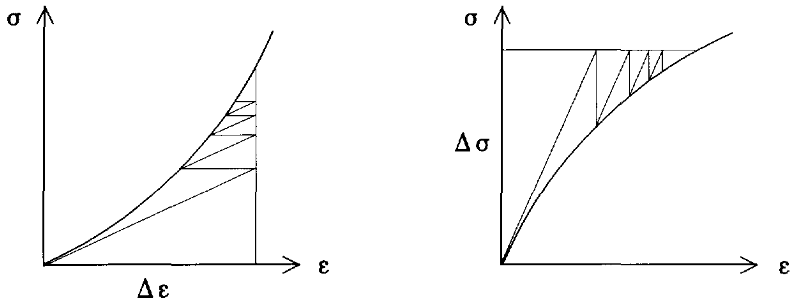

Figure 5.1 Initial strain method versus initial stress method
a. Initial strain b. Initial stress

In case of increasing material stiffness, e.g. for elastic compression problems, the initial strain method is preferred because a better control of the iteration process is obtained than in case of the initial stress method. For a similar reason, in case of decreasing material stiffness, e.g. for unloading problems, the initial stress method is preferable to the initial strain method. Both methods are schematically represented in Figure 5.1.

5.4.2 The cap hardening

The integration of the hardening part of the Plaxis cap model can conveniently be formulated in terms of the mean stress p and the deviatoric stress q, starting from the simplified form of Hooke's law as formulated in Equation 2.6. The tangential elastic stiffness parameters K_t and G_t, as updated at the beginning of a time-step, are considered to be constant in that step. In that case the integration of stresses in time-step i can be written as:

$$p^i = p^{i-1} + K_t\,(\Delta\varepsilon_v - \Delta\varepsilon_v^p) = p^{tr} - K_t\,\Delta\varepsilon_v^p \tag{5.27a}$$

$$q^i = q^{i-1} + 3\,G_t\,(\Delta\varepsilon_s - \Delta\varepsilon_s^p) = q^{tr} - 3\,G_t\,\Delta\varepsilon_s^p \tag{5.27b}$$

In this equation p^{tr} and q^{tr} are the trial stresses, calculated according to Equations 2.3 from the Cartesian trial stresses $\underline{\sigma}^{tr}$ as formulated in Equation 5.17. Adopting an implicit integration scheme, the direction of the plastic strain increments is evaluated at the end of time-step i, i.e. for the new (unknown) stress state:

$$\Delta \varepsilon_v^p = \Delta\lambda \left[\frac{\partial f}{\partial p}\right]^i = \Delta\lambda \; (2\, p^i - p_c^i) \tag{5.28a}$$

$$\Delta \varepsilon_s^p = \Delta\lambda \left[\frac{\partial f}{\partial q}\right]^i = \Delta\lambda \; \frac{2\, q^i}{M^2} \tag{5.28b}$$

Substitution of Equations 5.28 into Equations 5.27 and elaboration leads to:

$$p^i = \frac{p^{tr} + \Delta\lambda \; K_t \, p_c^i}{1 + 2 \; \Delta\lambda \; K_t} \tag{5.29a}$$

$$q^i = \frac{q^{tr}}{1 + 6 \; \Delta\lambda \; G_t \; / \; M^2} \tag{5.29b}$$

The new stresses are formulated in terms of known quantities and the unknown increment of the plastic multiplier $\Delta\lambda$. The new preconsolidation stress p_c^i is evaluated from the hardening relation 4.34. Integration of this relation gives:

$$\Delta \varepsilon_v^p = \frac{1}{\theta \; (1-m)} \left[\frac{(p_c^i)^{1-m}}{(p_c^{i-1})^{1-m}} - 1 \right] \tag{5.30}$$

where θ is supposed to be a constant within a time-step. This auxiliary parameter is defined as:

$$\theta = \frac{(p_c^{i-1})^{m-1}}{\lambda^* / \kappa^* - 1} \; \frac{K^{ref}}{(p^{ref})^m} \tag{5.31}$$

On substituting the volumetric plastic strain increment, as formulated in Equation 5.28a, into Equation 5.30, one obtains an expression from which p_c^i can only be solved iteratively for arbitrary values of m, provided that $\Delta\lambda$ and p^i are known. Such an iteration process will make the stress integration procedure time-consuming.

Instead of the exact hardening relation 4.34, an approximation is introduced here, given by:

$$\dot{\varepsilon}_v^p = \frac{\lambda^* / \kappa^* - 1}{K^{ref}} \; \frac{(p^{ref})^m}{(p_c^{i-1})^{m-1} \; p_c^i} \; \dot{p}_c = \frac{1}{\theta} \; \frac{\dot{p}_c}{p_c^i} \tag{5.32}$$

For $m = 1$, Equation 5.32 is equal to the exact hardening relation 4.34 and similar to the hardening relation of the Modified Cam-Clay model (Equation 4.8). In that case θ is just $1 / (\lambda^* - \kappa^*)$. In any other case $(m < 1)$ the approximation is still quite good as long as p_c^i is close to p_c^{i-1}, i.e. when the step-size is relatively small.

Analytical integration of the approximation of the hardening rule as formulated in Equation 5.32 leads to the following expression:

$$p_c^i = p_c^{i-1} \exp(\theta \, \Delta\varepsilon_v^p) = p_c^{i-1} \exp\left(\Delta\lambda \, \theta \, (2p^i - p_c^i)\right) \tag{5.33}$$

Again, this equation can only be solved iteratively. As an alternative, Equation 5.32 is integrated by means of numerical trapezoidal integration. The original idea comes from Borja and Lee (1990) who applied trapezoidal integration to the hardening relation of the Modified Cam-Clay model.

$$\int \dot{p}_c \, d\tau = \int \theta \, p_c \, \dot{\varepsilon}_v^p \, d\tau \tag{5.34}$$

$$p_c^i = p_c^{i-1} + (1-\omega) \, \theta \, p_c^{i-1} \, \Delta\varepsilon_v^p + \omega \, \theta \, p_c^i \, \Delta\varepsilon_v^p \tag{5.35}$$

$$p_c^i = \left[\frac{1 + (1-\omega) \, \theta \, \Delta\varepsilon_v^p}{1 - \omega \, \theta \, \Delta\varepsilon_v^p} \right] p_c^{i-1} \tag{5.36}$$

The type of numerical integration may vary from explicit $(\omega = 0)$ to implicit $(\omega = 1)$. Further on in this section the consequences of a particular choice of ω are discussed in more detail.

Substitution of the volumetric plastic strain increment as formulated in Equation 5.28a gives:

$$p_c^i = \left[\frac{1 + (1-\omega) \, \theta \, \Delta\lambda \, (2p^i - p_c^i)}{1 - \omega \, \theta \, \Delta\lambda \, (2p^i - p_c^i)} \right] p_c^{i-1} \tag{5.37}$$

Substitution of the expression for p^i (Equation 5.29a) leads to a quadratic relation for p_c^i based on the known quantities and the unknown increment of the plastic multiplier $\Delta\lambda$.

$$A \, (p_c^i)^2 + B \, p_c^i + C = 0 \tag{5.38}$$

with

$$A = \omega\ \theta\ \Delta\lambda \tag{5.39a}$$

$$B = 1 + 2\ \Delta\lambda\ K_t - 2\ \omega\ \theta\ \Delta\lambda\ p^{tr} + (1-\omega)\ \theta\ \Delta\lambda\ p_c^{i-1} \tag{5.39b}$$

$$C = -\ p_c^{i-1} \left(1 + 2\ \Delta\lambda\ K_t + 2\ (1-\omega)\ \theta\ \Delta\lambda\ p^{tr}\right) \tag{5.39c}$$

The solution of the above equation can simply be formulated as:

$$p_c^i = -\ \frac{B}{2\ A} + \frac{1}{2\ A} \sqrt{B^2 - 4\ A\ C} \tag{5.40}$$

It should be noted that a second solution (with a minus sign in front of the second term) is not relevant as it gives a value less than or equal to zero. Moreover, for $\omega = 0$ (explicit method) Equation 5.38 is no longer quadratic and the above solution cannot be used. In that case the solution is given by:

$$p_c^i = \left[\frac{1 + 2\ \Delta\lambda\ K_t + 2\ \Delta\lambda\ \theta\ p^{tr}}{1 + 2\ \Delta\lambda\ K_t + \Delta\lambda\ \theta\ p_c^{i-1}} \right] p_c^{i-1} \qquad (\omega = 0) \tag{5.41}$$

Four calculation methods for p_c, as discussed above, were implemented in a computer code and the performances were analysed for $m = 1$. The first method is the analytical integration of the approximation of the hardening rule (Equation 5.33), in which a Newton-Raphson iteration process is utilized. The second one is the explicit numerical method ($\omega = 0$) in which p_c is directly obtained from Equation 5.41. The third one is a midpoint rule ($\omega = 0.5$) and the fourth one is the implicit method ($\omega = 1$). From the analysis the following conclusions were drawn:

The analytical method is very slow compared with the other methods and is not interesting considering implementation in a finite element program. The number of iterations required for an accuracy of 10^{-10} was, in the present analysis, found to be rather small (only 4 iterations). The slow performance is also due to the evaluation of the exponential function, which is time-consuming compared with ordinary floating point operations. The accuracy of the analytical method is perfect. The explicit numerical method is the fastest of all four methods. In this case no square root needs to be evaluated. However, the accuracy is low; the value of p_c is generally too low. The midpoint rule is reasonably fast. The accuracy is much better than when using the explicit or the implicit method and approaches the analytical solution. The implicit method is about as fast as the midpoint rule. The accuracy is low; the value of p_c is generally too high. Based on this analysis the midpoint rule is considered to be the best method to calculate p_c. The results are summarized in Table 5.1.

Table 5.1 Results from analysis on calculation methods for p_c

	Analytical	Explicit	Midpoint	Implicit
Speed	— —	+ +	+	+
Accuracy	+ +	—	+	—

Now all new stresses (p^i, q^i and p_c^i) are formulated in terms of trial stresses and stresses at the end of the previous time-step. The only unknown is the increment of the plastic multiplier $\Delta\lambda$, which follows from the condition that the yield function is zero for the new state of stress. Because of the highly non-linear character of the equations, a local iteration process is inevitable.

Applying a Newton-Raphson iteration scheme, the iteration process can be formulated as:

$$\Delta\lambda^j = \Delta\lambda^{j-1} - \frac{f}{df / d(\Delta\lambda)} \tag{5.42}$$

The derivative of the yield function towards $\Delta\lambda$ can be split into derivatives towards the different stress components:

$$\frac{df}{d(\Delta\lambda)} = \frac{\partial f}{\partial p^i}\frac{dp^i}{d(\Delta\lambda)} + \frac{\partial f}{\partial q^i}\frac{dq^i}{d(\Delta\lambda)} + \frac{\partial f}{\partial p_c^i}\frac{dp_c^i}{d(\Delta\lambda)} \tag{5.43}$$

The derivatives of the yield function are straightforward. Elaboration of the derivatives of the stress measures towards the plastic multiplier is based on the expressions for p^i, q^i and p_c^i (Equation 5.29a, 5.29b and 5.40 respectively), which gives:

$$\frac{dp}{d(\Delta\lambda)} = \frac{K_t\,\Delta\lambda}{1 + 2\,K_t\,\Delta\lambda}\frac{dp_c}{d(\Delta\lambda)} - \frac{K_t\,(2\,p^i - p_c^i)}{1 + 2\,K_t\,\Delta\lambda} \tag{5.44a}$$

$$\frac{dq}{d(\Delta\lambda)} = -\frac{q^i}{\Delta\lambda + \dfrac{M^2}{6\,G}} \tag{5.44b}$$

$$\frac{dp_c}{d(\Delta\lambda)} = \frac{\frac{1}{2}\,\theta\,(2\,p^i - p_c^i)\,(p_c^i + p_c^{i-1})}{1 + 2\,K_t\,\Delta\lambda - \frac{1}{2}\,\theta\,\Delta\lambda\,(1 + 2\,K_t\,\Delta\lambda)\,(2p^i - p_c^i) + \frac{1}{2}\,\theta\,\Delta\lambda\,(p_c^i + p_c^{i-1})} \tag{5.44c}$$

In general, only a few iterations are required to make the yield function zero within a small tolerance.

Once the proper $\Delta\lambda$ has been obtained, the new stresses follow from Equation 5.29 and the new preconsolidation stress follows from Equation 5.40. Transformation of p and q back into Cartesian stress components can be done according to:

$$\underline{\sigma} = -p\,\underline{\delta} + q\sqrt{\frac{2}{3}}\;\underline{s} \tag{5.45}$$

where $\underline{\delta} = (1 \;\; 1 \;\; 1 \;\; 0 \;\; 0 \;\; 0)^T$ and $\underline{s}$ is a normalized stress direction vector based on the trial stresses:

$$\underline{s} = \frac{\sqrt{3/2}}{q^{tr}}\left[\sigma_{xx}^{tr} + p^{tr} \quad \sigma_{yy}^{tr} + p^{tr} \quad \sigma_{zz}^{tr} + p^{tr} \quad \sigma_{xy}^{tr} \quad \sigma_{yz}^{tr} \quad \sigma_{zx}^{tr}\right]^T \tag{5.46}$$

The full process for the determination of the new stresses at the yield cap is summarized in the scheme on the next page. The procedure is very robust. Note that for non-linear yield surfaces the use of implicit integration may lead to deviations in plastic strains when large load steps are taken. In that case, sub-stepping can be used to improve the results.

```
$\underline{\sigma}^{tr} = \underline{\sigma}^{i-1} + \underline{\underline{D}}^{e} \, \Delta\underline{\varepsilon}$
calculate $p^{tr}$, $q^{tr}$ and $\underline{s}$ from $\underline{\sigma}^{tr}$                    (Equation 2.3 / 5.46)
$p^{tr} = p^{tr} + c\cot\phi$
$p_c = p_c^{i-1} + c\cot\phi$
calculate $f(p^{tr}, q^{tr}, p_c)$                    (Equation 4.28a)
if $f > 0$ then
    $\Delta\lambda = 0$
    error = 2 * tolerance
    while error > tolerance
        calculate $f(p, q, p_c)$                    (Equation 4.28a)
        calculate $df / d(\Delta\lambda)$                    (Equation 5.43)
        $\Delta\lambda = \Delta\lambda - \dfrac{f}{df/d(\Delta\lambda)}$                    (Equation 5.42)
        calculate $p_c$                    (Equation 5.40)
        calculate $p$                    (Equation 5.29a)
        calculate $q$                    (Equation 5.29b)
        $p_c^f = p + \dfrac{q^2}{p\,M^2}$
        error $= \left| \dfrac{p_c^f - p_c}{p_c} \right|$
    end of while
end of if
$p^i = p^i - c\cot\varphi$
$p_c^i = p_c^i - c\cot\varphi$
calculate $\underline{\sigma}^i$ from $p^i$, $q^i$ and $\underline{s}$                    (Equation 5.45)
```

5.4.3 The point of combined yielding

The point of combined yielding in the Plaxis Cap model is the point where the Cam-Clay cap and the Drucker-Prager cone intersect. At this point the new stresses are such that both yield functions as defined in Equation 4.28 are zero:

$$\left[\frac{q^i}{M}\right]^2 + p^i\,(p^i - p_c^i) = 0 \tag{5.47a}$$

$$q^i - \alpha\, p^i = 0 \qquad\qquad q^i \,/\, p^i = \alpha \tag{5.47b}$$

Equation 5.47b gives a direct relation between the deviatoric stress and the mean stress. On combining both conditions, a relation between the preconsolidation stress and the mean stress can be obtained as well, which gives:

$$p_c^i = \left[1 + \frac{\alpha^2}{M^2}\right] p^i \tag{5.48}$$

Both yield functions contribute to plastic straining. In line with Equations 5.27 the new stresses can be formulated for this case as:

$$p^i = p^{tr} - K_t\,(\Delta\varepsilon_{v1}^p + \Delta\varepsilon_{v2}^p) \tag{5.49a}$$

$$q^i = q^{tr} - 3\,G_t\,(\Delta\varepsilon_{s1}^p + \Delta\varepsilon_{s2}^p) \tag{5.49b}$$

The subscript 1 relates to the cap yield function and the subscript 2 relates to the cone yield function. One of the characteristics of the Plaxis Cap model is that at the point of intersection the direction of plastic straining for each individual yield function, defined by the corresponding flow rules, is constant and predefined. Hence, a direct coupling between the individual deviatoric plastic strain increments and volumetric plastic strain increments can be made:

$$\Delta\varepsilon_{s1}^p = \frac{\partial\varepsilon_{s1}^p}{\partial\varepsilon_{v1}^p}\,\Delta\varepsilon_{v1}^p = \frac{2\,q^i/p^i}{M^2 - (q^i/p^i)^2}\,\Delta\varepsilon_{v1}^p = \frac{2\,\alpha}{M^2 - \alpha^2}\,\Delta\varepsilon_{v1}^p \tag{5.50a}$$

$$\Delta\varepsilon_{s2}^p = \frac{\partial\varepsilon_{s2}^p}{\partial\varepsilon_{v2}^p}\,\Delta\varepsilon_{v2}^p = -\,\frac{1}{\beta}\,\Delta\varepsilon_{v2}^p \tag{5.50b}$$

The latter part of Equation 5.50a is obtained by substitution of Equation 5.47b. The deviatoric stress is now reformulated in terms of volumetric plastic strain increments:

$$q^i = q^{tr} - 3\,G_t \left[\frac{2\,\alpha}{M^2 - \alpha^2}\,\Delta\varepsilon^p_{v1} - \frac{1}{\beta}\,\Delta\varepsilon^p_{v2} \right] \tag{5.51}$$

Substitution of the expressions for the new stresses (Equation 5.49a and Equation 5.51) into Equation 5.47b gives a linear relation between both volumetric plastic strain increments:

$$\Delta\varepsilon^p_{v1} \left[\alpha K_t - \frac{6\,\alpha\,G_t}{M^2 - \alpha^2} \right] + \Delta\varepsilon^p_{v2} \left[\alpha K_t + \frac{3\,G_t}{\beta} \right] + q^{tr} - \alpha p^{tr} = 0 \tag{5.52}$$

The preconsolidation stress p_c is obtained by integration of the hardening relation. In the case of combined yielding it is also very convenient to use the numerical trapezoidal integration scheme as proposed in the previous section (Equation 5.35), because this enables a direct solution as will be shown below. It should be noted that hardening is only related with plastic straining according to cap yielding. Hence, a change in the preconsolidation stress is only induced by a plastic strain increment that follows from the cap yield function. In line with Equation 5.36 it follows that:

$$p^i_c = \left[\frac{1 + (1-\omega)\,\theta\,\Delta\varepsilon^p_{v1}}{1 - \omega\,\theta\,\Delta\varepsilon^p_{v1}} \right] p^{i-1}_c \tag{5.53}$$

Combination of Equations 5.48, 5.49a, 5.52 and 5.53 gives after some manipulation a quadratic expression for the first volumetric plastic strain increment:

$$A\,(\Delta\varepsilon^p_{v1})^2 + B\,\Delta\varepsilon^p_{v1} + C = 0 \tag{5.54}$$

where

$$A = \omega\,\theta\,C_1\,C_2 \tag{5.55a}$$

$$B = -C_1\,C_2 - \omega\,\theta\,C_1\,C_3 - (1-\omega)\,\theta\,p^{i-1}_c \tag{5.55b}$$

$$C = C_1\,C_3 - p^{i-1}_c \tag{5.55c}$$

$$C_1 = 1 + \frac{\alpha^2}{M^2} \tag{5.55d}$$

$$C_2 = K_t - \frac{\beta\ K_t}{d_2} \left[\alpha\ K_t - \frac{6\ \alpha\ G_t}{M^2 - \alpha^2} \right] \tag{5.55e}$$

$$C_3 = \frac{3\ G_t}{d_2}\ p^{tr} + \frac{\beta\ K_t}{d_2}\ q^{tr} \tag{5.55f}$$

$$d_2 = \alpha\ \beta\ K_t + 3\ G_t \tag{5.55g}$$

The solution to Equation 5.54 is given by:

$$\Delta\varepsilon^p_{vI} = \frac{-B}{2A} - \frac{1}{2A}\sqrt{B^2 - 4AC} \qquad \text{for} \qquad K_t < \frac{6\ G_t}{M^2 - \alpha^2} \tag{5.56a}$$

$$\Delta\varepsilon^p_{vI} = \frac{-B}{2A} + \frac{1}{2A}\sqrt{B^2 - 4AC} \qquad \text{for} \qquad K_t > \frac{6\ G_t}{M^2 - \alpha^2} \tag{5.56b}$$

Having obtained the first volumetric plastic strain increment, the other plastic strain increments follow from Equations 5.52 and 5.50 respectively, after which the new stresses are obtained from Equations 5.49 and 5.53. Transformation of stresses into Cartesian components follows from the procedure as already formulated at the end of the previous section.

Hence, no local iterative procedure is required to calculate the new stresses in this particular case. Note that other ways of integrating the hardening rule lead to a highly non-linear relation that can only be solved iteratively, which is less attractive.

5.5 Global iterative procedures

Substitution of the relationship between stress increments and strain increments into the equilibrium equation 5.13 leads to:

$$\underline{\underline{K}}^i \, \Delta \underline{v}^i = \underline{f}^i_{ex} - \underline{f}^{i-1}_{in} \tag{5.57}$$

In this equation $\underline{\underline{K}}$ is a stiffness matrix, $\Delta \underline{v}$ is the incremental displacement vector, $\underline{f}_{ex}$ is the external force vector and $\underline{f}_{in}$ is the internal reaction vector. The superscript i refers to the step number. However, because the relation between stress increments and strain increments is generally non-linear, the stiffness matrix cannot be formulated exactly beforehand. Hence, a global iterative procedure is required to satisfy both the equilibrium condition and the constitutive relation. The global iteration process can be written as:

$$\underline{\underline{K}}^j \, \delta \underline{v}^j = \underline{f}^i_{ex} - \underline{f}^{j-1}_{in} \tag{5.58}$$

The superscript j refers to the iteration number. $\delta \underline{v}$ is a vector containing sub-incremental displacements, which contribute to the displacement increments of step i:

$$\Delta \underline{v}^i = \sum_{j=1}^{n} \delta \underline{v}^j \tag{5.59}$$

where n is the number of iterations within step i. The stiffness matrix $\underline{\underline{K}}$, as used in Equation 5.58, represents the material behaviour in an approximated manner. The more accurate the stiffness matrix, the fewer iterations are required to obtain equilibrium within a certain tolerance.

In its simplest form $\underline{\underline{K}}$ represents a linear-elastic response. In this case the stiffness matrix can be formulated as:

$$\underline{\underline{K}} = \int \underline{\underline{B}}^T \, \underline{\underline{D}}^e \, \underline{\underline{B}} \, dV \qquad \text{(elastic stiffness matrix)} \tag{5.60}$$

where $\underline{\underline{D}}^e$ is the elastic material matrix and $\underline{\underline{B}}$ is the strain interpolation matrix. The use of an elastic stiffness matrix in combination with the initial stress method as described in Section 5.4.1 gives a very robust iterative procedure as long as the material stiffness does not increase, even when using non-associated plasticity models. Special techniques such as arc-length control (Riks, 1979), over-relaxation and extrapolation (Vermeer & Van Langen, 1989) can be used to improve the iteration process. Moreover, the automatic step size procedure, as introduced by Van Langen & Vermeer (1990), can be used to improve the practical applicability. For material models with linear behaviour in the elastic domain, the use of an elastic stiffness matrix is particularly favourable, as the stiffness matrix needs only be formed and decomposed before the very first calculation step. For material models in which the elastic behaviour is non-linear, the current method is still competitive. A minor disadvantage is that the failure load may be slightly overpredicted, but the overprediction can be kept small by utilizing a small tolerated equilibrium error.

A stiffness matrix that resembles the material response more accurately is obtained by including plasticity. In this case the stiffness matrix can be formulated as:

$$\underline{\underline{K}} = \int \underline{\underline{B}}^T \, \underline{\underline{M}} \, \underline{\underline{B}} \, dV \qquad \text{(tangent stiffness matrix)} \qquad (5.61)$$

where $\underline{\underline{M}}$ is the elastoplastic material matrix based on the current state of stress:

$$\underline{\underline{M}} = \frac{\partial \underline{\sigma}}{\partial \underline{\varepsilon}} \qquad (5.62)$$

$\underline{\underline{M}}$ can be obtained from the procedure as described at the end of Section 3.2. The use of a tangent stiffness matrix reduces the number of iterations required for convergence, but according to the author's experience, the procedure is not as robust as using an elastic stiffness matrix, particularly when failure approaches. The range of load step for which proper convergence is obtained is much smaller than for an elastic stiffness matrix. On using a tangent stiffness matrix, distinction should be made between a Full Newton-Raphson procedure, where the matrix is updated each iteration, and a Modified Newton-Raphson procedure, where the matrix is updated only once per step. The latter case proved to be less robust than the former case, especially when relatively large stress rotations occur within a step.

The use of an implicit integration scheme, as formulated in Equation 5.17, leads to an additional term compared with the original constitutive relation when taking the time derivative:

$$\dot{\underline{\sigma}} = \underline{\underline{D}}^e \, \dot{\underline{\varepsilon}} - \dot{\lambda} \, \underline{\underline{D}}^e \left[\frac{\partial g}{\partial \underline{\sigma}} \right]^i - \Delta\lambda \, \underline{\underline{D}}^e \left[\frac{\partial^2 g}{\partial \underline{\sigma}^2} \right]^i \dot{\underline{\sigma}} \qquad (5.63)$$

The additional term can simply be transferred to the left-hand side. Hence, in order to obtain a tangent stiffness matrix that is consistent with the implicit integration scheme, the elastic material matrix $\underline{\underline{D}}^e$, that is used for the composition of $\underline{\underline{M}}$, should be exchanged by a matrix $\underline{\underline{D}}^*$ which is defined as:

$$\underline{\underline{D}}^* = \left[\underline{\underline{I}} + \Delta\lambda \, \underline{\underline{D}}^e \left(\frac{\partial^2 g}{\partial \underline{\sigma}^2} \right)^i \right]^{-1} \underline{\underline{D}}^e \qquad (5.64)$$

in which $\underline{\underline{I}}$ is the identity matrix. Note that the second derivative of the plastic potential function towards the stresses represents a symmetric matrix. For the Drucker-Prager model and the Modified Cam-Clay model the terms in this matrix are given in the appendix at the end of this chapter.

The resulting global matrix is a *consistent tangent stiffness matrix*, and was firstly formulated in this form by Crisfield (1987). In the current study it was observed that in general the convergence indeed improves compared with the conventional tangent stiffness matrix in a full Newton-Raphson procedure, but the robustness appeared to be less, particularly when failure approaches.

Another minor disadvantage of a tangent stiffness is the problem that it may become singular as soon as a failure mechanism is fully developed. However, this problem can simply be avoided by multiplying the plastic contribution in the elastoplastic material matrix with a reduction factor R slightly less than 1.0:

$$\underline{\underline{M}} = \underline{\underline{D}}^e - \frac{R}{d+h} \underline{\underline{D}}^e \frac{\partial g}{\partial \underline{\sigma}} \frac{\partial f}{\partial \underline{\sigma}}^T \underline{\underline{D}}^e \qquad (5.65)$$

By doing so, one should realize that the resulting matrix is no longer a full tangent stiffness matrix, and that the convergence speed of equilibrium iterations is reduced.

Appendix

Formulation of second derivatives of plastic potential function towards stress components for Drucker-Prager model and Modified Cam-Clay model. These terms are required in a consistent tangent stiffness matrix (see Equation 5.64).

Drucker-Prager:

$$\frac{\partial^2 g}{\partial \sigma_{xx}^2} = \frac{1}{q} - \frac{9}{4}\frac{(p + \sigma_{xx})^2}{q^3} \tag{A5.1a}$$

$$\frac{\partial^2 g}{\partial \sigma_{xx}\,\partial \sigma_{yy}} = -\frac{1}{2q} - \frac{9}{4}\frac{(p + \sigma_{xx})\,(p + \sigma_{yy})}{q^3} \tag{A5.1b}$$

$$\frac{\partial^2 g}{\partial \sigma_{xx}\,\partial \sigma_{zz}} = -\frac{1}{2q} - \frac{9}{4}\frac{(p + \sigma_{xx})\,(p + \sigma_{zz})}{q^3} \tag{A5.1c}$$

$$\frac{\partial^2 g}{\partial \sigma_{xx}\,\partial \sigma_{xy}} = -\frac{9}{2}\frac{(p + \sigma_{xx})\,\sigma_{xy}}{q^3} \tag{A5.1d}$$

etc.

$$\frac{\partial^2 g}{\partial \sigma_{xy}^2} = -\frac{3}{q} - 9\,\frac{\sigma_{xy}^2}{q^3} \tag{A5.1e}$$

$$\frac{\partial^2 g}{\partial \sigma_{xy}\,\partial \sigma_{yz}} = -9\,\frac{\sigma_{xy}\,\sigma_{yz}}{q^3} \tag{A5.1f}$$

etc.

Modified Cam-Clay:

$$\frac{\partial^2 g}{\partial \sigma_{xx}^2} = \frac{2}{9} + \frac{2}{M^2} \tag{A5.2a}$$

$$\frac{\partial^2 g}{\partial \sigma_{xx}\, \partial \sigma_{yy}} = \frac{2}{9} - \frac{1}{M^2} \tag{A5.2b}$$

$$\frac{\partial^2 g}{\partial \sigma_{xx}\, \partial \sigma_{zz}} = \frac{2}{9} - \frac{1}{M^2} \tag{A5.2c}$$

$$\frac{\partial^2 g}{\partial \sigma_{xx}\, \partial \sigma_{xy}} = 0 \tag{A5.2d}$$

etc.

$$\frac{\partial^2 g}{\partial \sigma_{xy}^2} = \frac{6}{M^2} \tag{A5.2e}$$

$$\frac{\partial^2 g}{\partial \sigma_{xy}\, \partial \sigma_{yz}} = 0 \tag{A5.2f}$$

etc.

6 APPLICATIONS OF THE PLAXIS CAP MODEL

In this chapter the Plaxis Cap model will be used in a few examples to assess the applicability of the model in practical situations. Comparison will be made with perfectly-plastic models in order to evaluate the need for hardening plasticity. It will be shown that some problems may as well be analysed by perfectly-plastic models, whereas other problems require hardening plasticity for good accuracy.

6.1 Plate loading test

In this section a comparison is made between the Plaxis Cap model and the perfectly-plastic Drucker-Prager model. The latter model was chosen because failure in the Drucker-Prager model is equivalent to failure in the Plaxis Cap model. For this application the Drucker-Prager model was extended with a power law on the elastic stiffness, similar to the Plaxis Cap model. The main difference between both models is the hardening plasticity.

The application is the back-analysis of a scale model test as schematically represented in Figure 6.1. The test concerns the indentation of a circular footing as reported by Labanieh (1984). The container in which the test was performed has a depth of 2 m and a diameter of 1.5 m. The diameter of the footing is 0.4 m. The material involved is loose Hostun sand with a medium grain size D_{50} of 0.63 mm, an initial void ratio e_0 of 0.74 and a dry weight of 15.3 kN/m^3.

Model parameters, as listed in Table 6.1, are mainly based on triaxial test results as plotted in Figure 6.2, in particular the triaxial test curves for $\sigma_3 = 100$ kPa and $\sigma_3 = 200$ kPa, because these pressures are representative for the plate loading test.

Table 6.1 Model parameters for plate loading test

Parameter	Symbol	Plaxis Cap	Drucker-Prager	Unit
Reference stiffness	G^{ref}	30000	5000	kPa
Power	m	0.5	0.5	-
Poisson's ratio	ν	0.1	0.33	-
Compression ratio	λ^* / κ^*	3.0	-	-
Friction parameter	α	1.15	1.15	-
Tangent of CSL	M	1.5	-	-
Coeff. lateral earth pres.	K_0	0.5	0.5	-

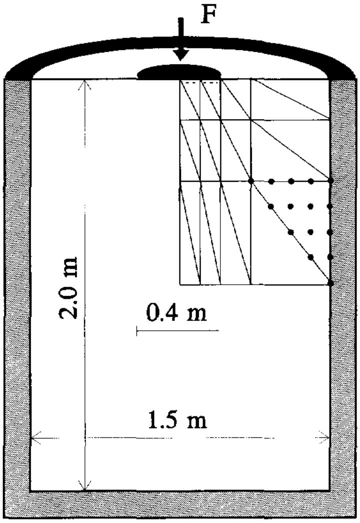

Figure 6.1 Geometry of plate loading test and finite element schematization

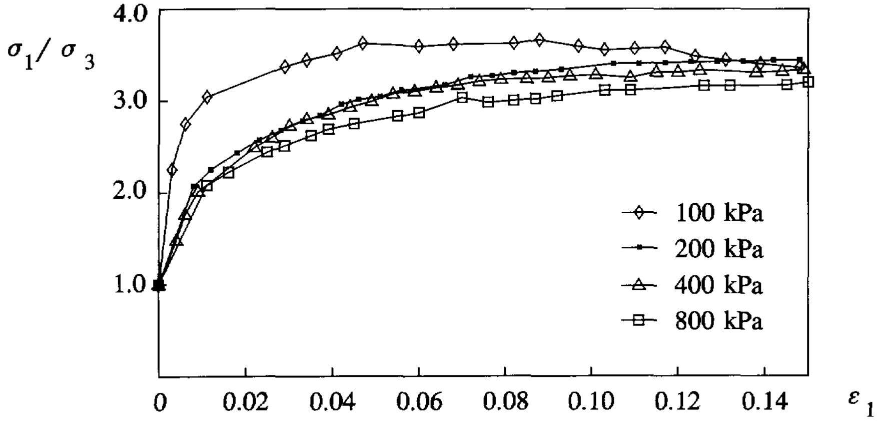

Figure 6.2 Triaxial test results for loose Hostun sand by Labanieh (1984)

As a rule for sand, the power m is taken as 0.5. Young's modulus is determined in a numerical simulation of triaxial tests by matching the curves of Figure 6.2. The result is an E^{ref} of 66000 kPa for $p^{ref} = 100$ kPa. Taking Poisson's ratio $\nu = 0.1$ gives a G^{ref} of 30000 kPa. The ratio λ^*/κ^*, i.e. the ratio of total volumetric strain over recoverable volumetric strain in isotropic compression, cannot be obtained from the available test data. Published test data on similar loose sands show that $\lambda^*/\kappa^* = 3.0$ is quite realistic.

The friction angle φ follows from the triaxial test results as plotted in Figure 6.2, which gives an average of 32°. The dilation angle can also be obtained from triaxial test results when plotting the vertical strain against the volumetric strain. However, such accurate data were not available. Therefore the dilation angle was chosen to be the friction angle minus 30°, which gives $\psi = 2°$. The coefficient of lateral earth pressure, K_0, for the initial stress state is estimated at 0.5. This value of K_0 can also be utilized to determine the constant M using Equation 4.26, which gives a value of 1.5.

The friction parameter α is related with the friction angle φ, as used in the Mohr-Coulomb model. From the condition that the failure load should be similar to that in the Mohr-Coulomb model, exact relations between α and φ can be obtained for states of stress in triaxial compression (A) and triaxial extension (B), as given by Chen (1975). A relation for plane strain situations (C) was derived in Section 3.4 (Equations 3.33 and 3.37). The relation as meant for (A), i.e. $\alpha = 6 \sin\varphi \,/\, (3-\sin\varphi)$ giving $\alpha = 1.29$, was used to simulate the triaxial tests. However, the plate loading test does not apply to any of the stress states (A), (B) or (C). A value between those for triaxial compression and plane strain seems most likely. The selected value for α is 1.15.

For the calculation with the Drucker-Prager model most parameters can be taken the same as for the Plaxis Cap model, except for the reference shear modulus and Poisson's ratio. Using a perfectly-plastic model in primary loading implies that the stiffness is much lower than the "elastic" stiffness as used in a hardening model, as it should partly account for plastic strains as well. A realistic approach is to take G^{ref} at 50% of the strength in a triaxial test and to take ν such that a proper value for K_0 is found in a one-dimensional compression test. In this case we find $G^{ref} = 5000$ kPa and $\nu = 1/3$.

The geometry is schematized by an axi-symmetric finite element mesh of 15-noded (cubic strain) elements with 12-point Gaussian integration. It has been shown that these elements tend to yield highly accurate solutions for axi-symmetric problems (Sloan & Randolph, 1982; De Borst & Vermeer, 1984). A pilot calculation showed that the deformation in the lower part of the geometry is extremely small compared with the deformations just below the footing, so that it is justified to model only the upper part of the geometry in a finite element mesh, as shown in Figure 6.1. Interface elements, indicated in the figure by dashed lines, are used to simulate the interaction between the plate and the soil. The interface friction angle is taken at 28°, a reduction of 15% compared with the soil friction angle. The boundary conditions are chosen such that the vertical mesh sides are fully smooth and the bottom of the mesh is fully rough. The top of the mesh is free to move in any direction, except for the part that is covered by the plate.

After generation of the initial stress state, the indentation of the footing is simulated by imposing prescribed vertical displacements on top of the mesh at the position of the plate. Two calculations are performed for each model. The first one is a calculation according to the generally applied small strain concept, which is a description with reference to the initial undeformed geometry. The second calculation is an Updated Lagrangean analysis, which includes changes of the geometry and in which Hill's objective stress formulation is obeyed (McMeeking & Rice, 1975). The results of the calculations are presented in Figures 6.3 to 6.5.

Comparison of Figure 6.3 and 6.4 shows that there is hardly any difference between the calculations with the Drucker-Prager model and the Plaxis Cap model. It should be realized that, in this application, the sand is only primarily loaded. If the test were to include unloading, there would be a considerable difference between the two models when using the same set of model parameters. However, in many applications only primary loading is of importance, but as yet it cannot be concluded that under such conditions perfectly-plastic models perform as well as hardening models. It appears that fitting of stiffnesses based on triaxial test data gives quite good results for both models. Note that for general applications the friction parameter α cannot be verified by simulating triaxial tests. It seems that in the current example α was correctly chosen. However, in particular for axi-symmetric or general three-dimensional applications the choice of α is still a point of discussion. Therefore it would be better to replace the Drucker-Prager yield criterion in the Plaxis Cap model by a Mohr-Coulomb type yield criterion.

For displacements over 10 mm, the curves from the small strain calculations deviate from the test data, but the curves from the updated Lagrangean analyses match the data quite well. The uplift of the soil beside the plate acts like an overburden load, which has a positive influence on the bearing capacity. This effect is not taken into account when performing calculations according to small strain theory.

Consider the situation with a force of 10 kN. This force gives an average footing pressure of 80 kPa. Just underneath the footing the stresses are mainly in a state far from failure, except at the edge. From this observation it can be concluded that there is hardly any sliding between the plate and the sand.

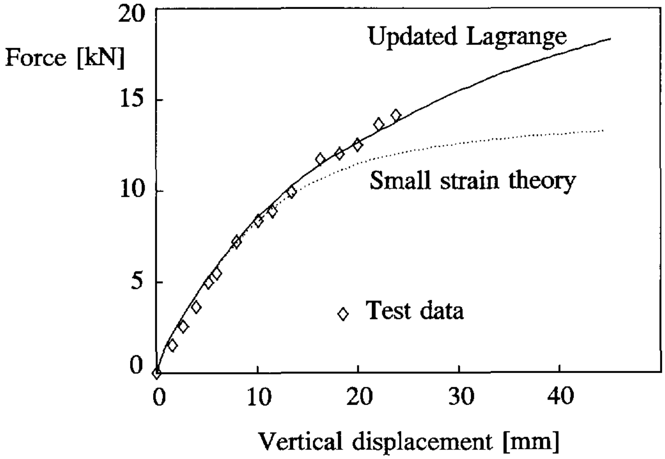

Figure 6.3 Force-Displacement curve for plate loading test using Plaxis Cap model

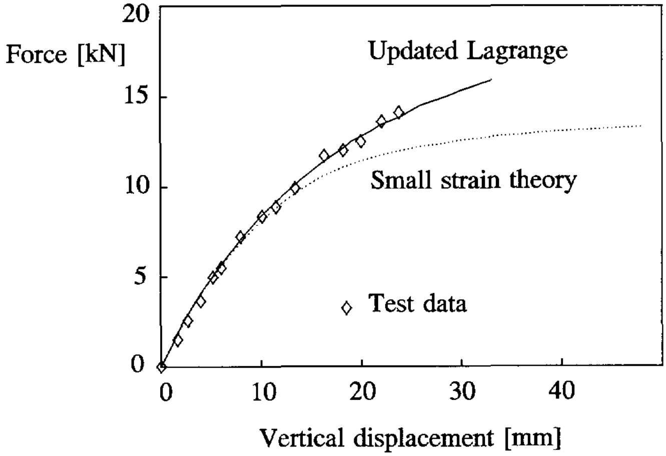

Figure 6.4 Force-Displacement curve for plate loading test using Drucker-Prager model

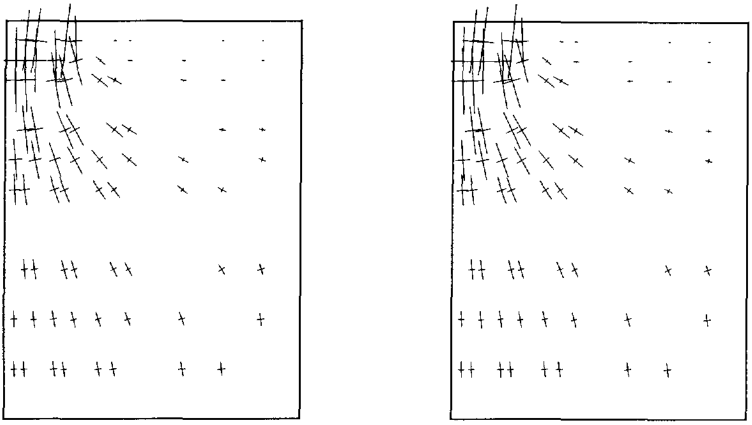

Figure 6.5 Principal stress distribution corresponding to a footing force of 10 kN. Maximum principal stress under the plate is about 110 kPa.
a. Plaxis Cap model b. Drucker-Prager model

At the bottom of the mesh, i.e. half the height of the sand container, the principal stress direction hardly differs from the initial principal stress direction, as can be evaluated from Figure 6.5. At this level the footing force has almost fully spread over the cross section. This application does not show advantages of the Plaxis Cap hardening model compared with a perfectly-plastic model with stress-dependent stiffness.

6.2 Almere trial embankment

On a location near Almere, The Netherlands, a large scale test was performed to investigate the influence of a geotextile reinforcement on the stability of an embankment (Brakel et al., 1982). Two trial embankments were constructed, one with a geotextile reinforcement and another without geotextile. The embankments were back-filled with sand until large deformations were observed. The height of the back-fill at which the large deformations occur is representative for the stability of the embankment. The geometry of the test is plotted in Figure 6.6.

The upper soil layer consists of a lightly overconsolidated clay. Below this layer there is a sand layer. For the reinforced case a geotextile is installed on the clay layer. The embankment is constructed on the clay layer up to a height of 2 m. The material involved

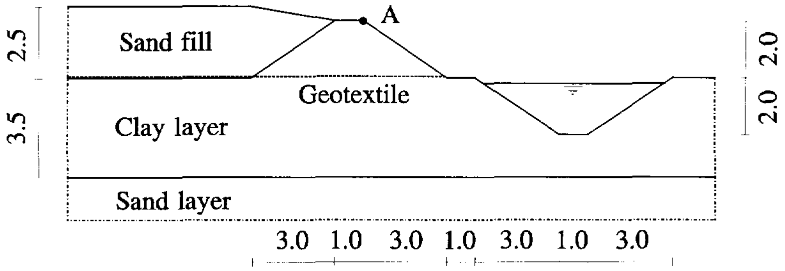

Figure 6.6 Geometry of reinforced trial embankment

is taken from the clay layer, so that a ditch is formed in front of the embankment. After construction, the embankment is back-filled with medium coarse sand.

In this section calculational results are presented for the reinforced trial embankment. In one calculation the clay layer is modelled by the Plaxis Cap model and another calculation is performed in which the clay is modelled by a non-linear elastic perfectly-plastic Drucker-Prager model, as already mentioned in the previous section. In the analysis, attention is focused on the deformations due to the undrained back-filling of the embankment followed by the decrease of excess pore pressures down to zero. The behaviour of the sand-fill is of minor interest. This material is modelled, in both calculations, by the Mohr-Coulomb model.

As a rule for clay, the power m in the Plaxis Cap model is taken as 1.0, which gives a logarithmic relation between the volumetric strain and the mean stress. The reference shear modulus is estimated as $G^{ref} = 6250$ kPa for a reference stress $p^{ref} = 100$ kPa. Poisson's ratio is chosen $\nu = 0.1$. From these data a corresponding swelling index $\kappa^* = 0.0175$ can be derived. The average undrained shear strength is $C_u = 10$ kPa, as obtained from cone penetration tests. In the current model, however, only effective properties can be given, so that C_u must be transformed into c and φ.

Undrained: $q_{\max} = \sqrt{3}\ C_u$ (plane strain) (6.1a)

Effective: $q_{\max} = \alpha\ (p + c \cot\varphi)$ (6.1b)

Combination of these two equations gives:

$$c = \frac{\sqrt{3}\ C_u - \alpha\ p}{\alpha\ \cot\varphi} \tag{6.2}$$

The friction angle is estimated at 25°. The friction constant α can be evaluated from Equation 3.33 ($\beta = 0$), which gives $\alpha = 0.73$. The average mean stress is initially 7 kPa. On using a Cam-Clay type model for normally consolidated clay, the mean stress reduces a little during undrained loading. However, in this application, the soil is lightly overconsolidated. Under these conditions the mean stress will barely change. Evaluation of Equation 6.2 gives an effective cohesion of 7.8 kPa.

The constant M is evaluated from Equation 4.26, in which, for the normally consolidated coefficient of lateral earth pressure K_0, Jaky's formula ($K_0 = 1 - \sin\varphi$) is substituted. In fact, the use of Equation 4.26 is not valid in this situation because of the relatively high cohesion, but it is used in the absence of an alternative. The K_0-value that is used to generate the initial stresses is taken somewhat higher than the value that follows from Jaky's formula, because the clay is lightly overconsolidated. A uniform overconsolidation ratio $OCR = 2.0$ is assumed. This results in elastic behaviour during the first part of loading.

For the calculation with the non-linear elastic Drucker-Prager model, the model parameters are taken equal to the parameters in the Plaxis Cap model. In order to match the behaviour during undrained loading of the lightly overconsolidated clay, the shear modulus G^{ref} and Poisson's ratio ν are also taken equal in both models. If the soil were not overconsolidated, however, it would be more realistic to choose a much smaller shear modulus and a higher Poisson's ratio.

An overview of all model parameters is given in Table 6.2. The undrained behaviour of the clay is simulated by using effective properties and adding a high bulk modulus for the water, which enables the calculation of excess pore pressures (Chan & Morgenstern, 1989; Vermeer, 1991).

The deformations in the underlaying sand layer are considered to be small compared with those in the clay layer. Therefore this layer is not included in the finite element mesh. A total of 46 triangular cubic strain elements are used to model the geometry. Initially, only the elements of the clay layer are active (1). After generation of initial stresses, the embankment is constructed and the ditch is dug by switching the elements involved on and off (2). The next stage is the back-filling of the embankment by switching on the remaining inactive elements (3), which corresponds to a situation just before failure. After this stage the clay is changed into a draining material and excess pore pressures are linearly decreased to zero (4). This is a simple way to evaluate the deformations after full consolidation. However, in general, care should be taken with this method, because the development of pore pressures is basically different from a real consolidation process. The four calculation stages are presented in Figure 6.7. For completeness it is reported that all calculations are limited to the small strain concept.

Table 6.2 Model parameters for Almere trial embankment

Parameter	Symbol	Plaxis Cap	Drucker-Prager	Unit
Soil weight	γ	13.5	13.5	kN/m^3
Reference stiffness	G^{ref}	6250	6250	kPa
Power	m	1.0	1.0	-
Poisson's ratio	ν	0.1	0.1	-
Compression ratio	λ^*/κ^*	4.0	-	-
Friction parameter	α	0.73	0.73	-
Tangent of CSL	M	1.35	-	-
Coeff. lateral earth pres.	K_0	0.7	0.7	-
Cohesion	c	7.8	7.8	kPa
Overconsolidation ratio	OCR	2.0	2.0	-

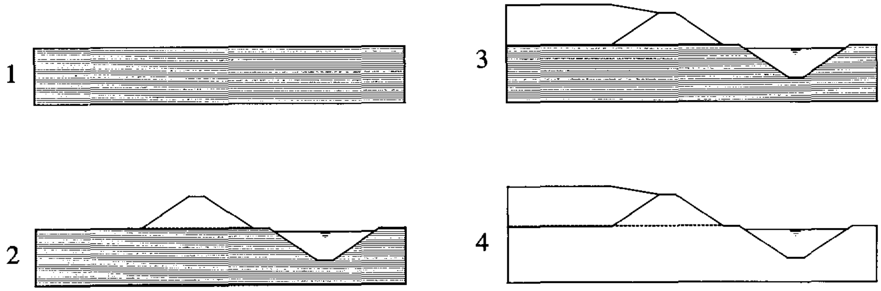

Figure 6.7 Calculation stages for Almere trial embankment

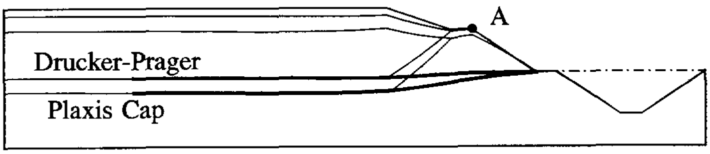

Figure 6.8 Final displacements of reinforced trial embankment using two different models. Deformations scale is much larger than geometry scale.

Figure 6.8 shows the deformed meshes of both calculations at the end of the calculation, i.e. after full consolidation. There is a remarkable difference between the results from the calculation performed with the Plaxis Cap model and the results from the Drucker-Prager model. The latter calculation predicts much smaller deformations. Unfortunately, no deformation measurements of the in situ test are available, so that a comparison between the calculational results and reality cannot be made.

Figure 6.9 shows a curve with the horizontal and vertical displacements of the embankment crest point A. The first branch (undrained loading) reflects the displacement during the back-filling of the embankment. For this part both models show approximately the same response. The second branch (consolidation) reflects the displacement during reduction of the excess pore pressures. For this part the responses deviate considerably.

In the first branch, the effective loading is primarily deviatoric because of the undrained behaviour. The overconsolidated material remains mainly elastic. Plasticity will only sporadically occur on the Drucker-Prager yield surface, which is present in both models. Because the model parameters are the same, the response should be the same as well. During the consolidation process the loading is basically similar to one-dimensional compression. In this case the Drucker-Prager model gives an elastic response in which the stiffness is dominated by G. The Plaxis Cap model gives cap yielding, i.e. hardening plasticity, as soon as the preconsolidation stress has been reached. From this point the stiffness is dominated by κ^*/λ^* times G, which gives a much weaker behaviour.

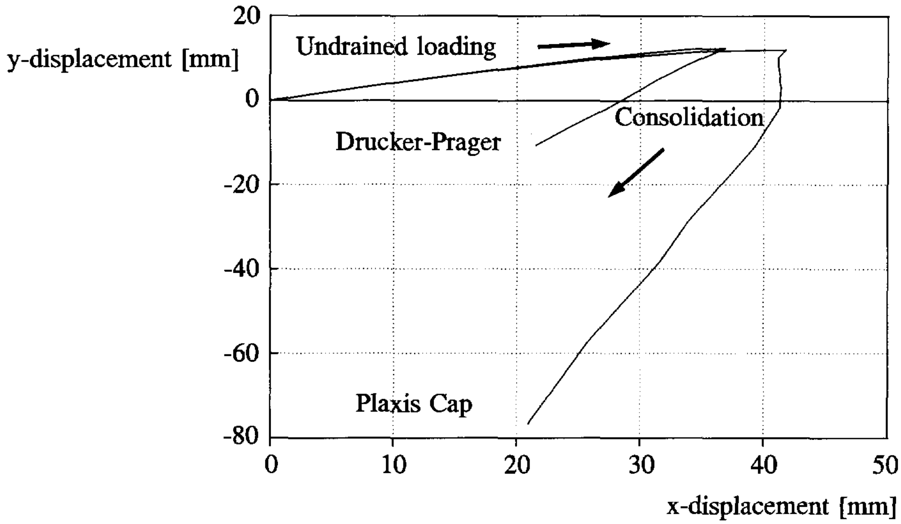

Figure 6.9 Horizontal versus vertical displacements of embankment crest point A

Instead of matching the first part of the calculation, the parameters in the Drucker-Prager model could also be chosen such that the deformations in the second part of the calculation would match. In that case the undrained loading would show very different results. Apart from the current example, it is a well-known phenomenon that for normally consolidated clay there is a remarkable difference in stiffness behaviour between deviatoric loading, as obtained with undrained soil behaviour, and compression, as obtained with consolidation. Using a non-hardening model, such as the Drucker-Prager model, one can match the behaviour for one particular type of loading, but it is not possible to simulate accurately the behaviour for both loading types, at least not when using a single set of parameters.

6.3 Brienenoord road widening project

In order to investigate new methods for the widening of existing road embankments on soft soil, some large scale test locations were appointed by the Dutch Ministry of Public Works. One of those was a test location along the A16 motorway near Rotterdam, which is known as the Brienenoord Corridor (BriCor). The widening of the road embankment was constructed in 1988. Settlements and horizontal deformations were measured during construction and soil samples were taken in order to investigate the soil types and their properties (Deutekom et al., 1992).

In the BriCor road widening project, the subsoil consists of soft, lightly overconsolidated clayey and peaty material. Before construction of the old embankment in former times, the soft soil was partly excavated and replaced by sandy soil. The new embankment, however, was directly constructed on the soft subsoil, without applying soil-improvement. This resulted in large settlements of the original surface level of the order of 2.5 m. In order to reduce the lateral deformations, the embankment widening was constructed according to the so-called *Gap method*. In this method a small embankment is built beside the existing embankment and the gap in between is filled up successively until the final height is reached.

In a numerical analysis by Couvreur and Vermaut (1992) a comparison was made between the gap method and the conventional method of constructing the embankment layer-by-layer. They concluded that the gap method indeed reduces the horizontal deformations, although the differences are not spectacular. In their calculations the Mohr-Coulomb model was used to simulate the behaviour of all soil layers. In the current study a comparison is made between the deformations as predicted by the Mohr-Coulomb model and the Plaxis Cap model in order to investigate the influence of the constitutive model.

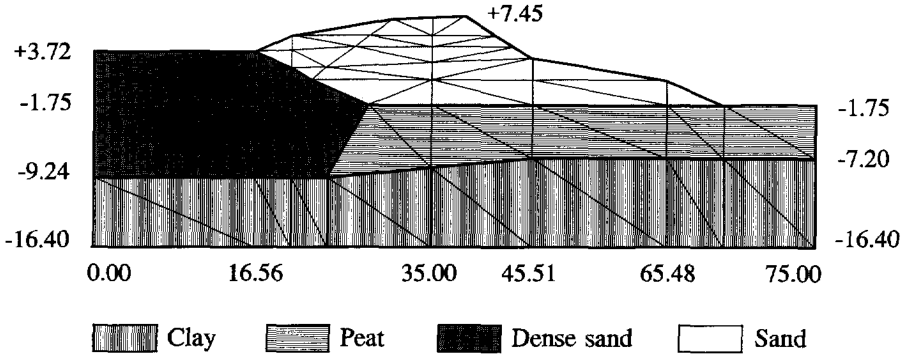

Figure 6.10 Finite element model of the embankment widening project

Figure 6.10 shows a finite element model of the problem under consideration with an indication of the different soil types. High-order 15-noded elements were used, as available in the Plaxis finite element code. The bottom of the mesh corresponds to a layer of stiff material on which the soft soil layers are situated. In reality, the distinction between the clay and the peat layer is not too clear. The left side of the plot indicates the old embankment, consisting of dense sandy material. The new embankment also consists of sandy material. The overheight of soil is needed to arrive at about the same level as the old embankment after the extreme settlement of the subsoil.

As most deformation is concentrated in the soft soil layers, these layers are given most attention. In one calculation, the soft soil layers are modelled by the Mohr-Coulomb model and in another calculation by the Plaxis Cap model. In both calculations the sandy layers are modelled by the Mohr-Coulomb model.

Extensive laboratory tests were performed on the soil samples taken from the in-situ soft soil layers (Van et al., 1991). These results were used to determine the material properties, from which the model parameters are derived as input for the finite element calculations. An overview of the parameters is given in Table 6.3. Considering the type of loading and the purpose of the calculation, attention will be focused in the following on the determination of the stiffness parameters.

The aim of the calculation is to evaluate the horizontal displacements of the original surface level 1000 days after construction of the embankment widening. From the available laboratory test data, an equivalent modified compression index was derived for a time span of 1000 days. This resulted in a λ^* of 0.15 for the clay layer and 0.20 for the peat layer.

Table 6.3. Model parameters for clay and peat layers

	Mohr-Coulomb		Plaxis Cap		
Symbol	Clay	Peat	Clay	Peat	Unit
γ_{dry}	14.0	11.0	14.0	11.0	kN/m^3
γ_{wet}	15.5	12.5	15.5	12.5	kN/m^3
κ^*			0.03	0.04	-
λ^*			0.15	0.20	-
G	155	75			kPa
ν	0.40	0.40	0.20	0.20	-
c	6.0	5.0	6.0	5.0	kPa
φ	20	23			°
α			0.59	0.68	-
M			1.23	1.38	-

The ratio of compression and swelling index is assumed to be 5.0 for both layers. On evaluating the average shear modulus to be used in the Mohr-Coulomb model, it was verified that both models would give the same settlements in one-dimensional compression, considering a representative column of subsoil. For each layer, the shear modulus was evaluated from the formula that follows from Hooke's law for one-dimensional compression:

$$G = \frac{1-2\nu}{2-2\nu} \frac{\Delta\sigma_{yy}}{\Delta\varepsilon_{yy}} \tag{6.3}$$

The new embankment comprises 9 m high sandy material with an effective weight of 17 kN/m^3. This gives a vertical load on the subsoil $(= \Delta\sigma_{yy})$ of 153 kPa. The vertical strain increment $\Delta\varepsilon_{yy}$ can be evaluated from the Terzaghi's logarithmic compression law, which is similar to the logarithmic stress-strain relation as used in the Plaxis Cap model. Note that the subsoil is lightly overconsolidated, so that, in fact, a part of the load involves reloading, for which a much stiffer behaviour is observed.

In both calculations the sandy embankment material is modelled by the Mohr-Coulomb model with a constant shear modulus of 2100 kPa, Poisson's ratio of 0.33, friction angle of 31°, a cohesion of 2 kPa and no dilatancy.

It is important to install the proper stress situation at the beginning of the new embankment construction. Therefore a jump is made to the situation before the old embankment was present, i.e. a horizontal surface (Figure 6.11 stage 1). The vertical preconsolidation stress was assumed to be 25 kPa higher than the initial vertical stress. In the Plaxis finite element

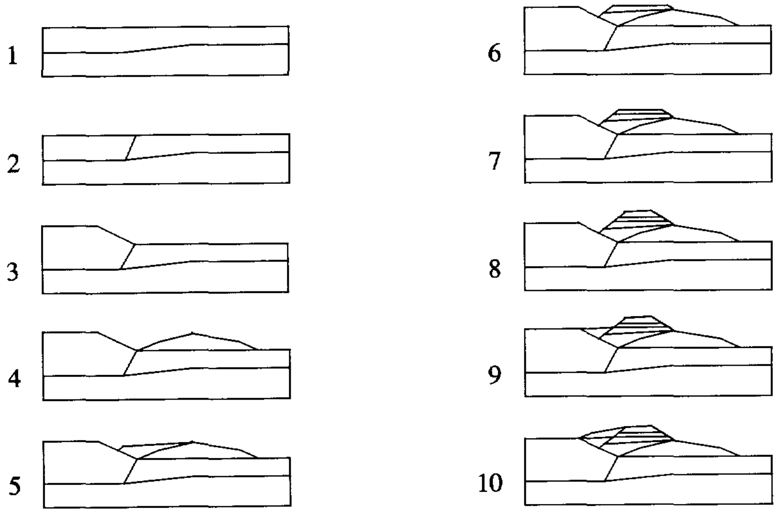

Figure 6.11 Construction stages for BriCor calculation

program this can simply be introduced by prescribing a so-called Pre-Overburden Pressure *POP*. For a constant positive *POP*, the local overconsolidation ratio *OCR* decreases with depth. The initial horizontal stress in an overconsolidated soil with horizontal surface can be estimated by considering one-dimensional elastic unloading from a state of normal consolidation:

$$\sigma_{xx}^{0} = K_0\, \sigma_{yy}^{0} - POP \left[K_0 - \frac{\nu}{1-\nu} \right] \tag{6.4}$$

After installation of the initial stress field, part of the peat layer was replaced by sand (stage 2) and the old embankment was constructed (stage 3). So far, calculations were performed using small strain theory. Displacements were reset back to zero after stage 3. This is the starting point for the construction of the new embankment.

The new embankment was constructed according to the gap method by means of several construction stages (stage 4 to 10). As considerable deformations were expected, an Updated Lagrangean analysis was performed in these stages, to account for the changes of the geometry during the calculation. All calculations were done under drained conditions, as all excess pore pressures are assumed to have disappeared after 1000 days. The results of both calculations are shown in Figures 6.12, 6.13 and 6.14.

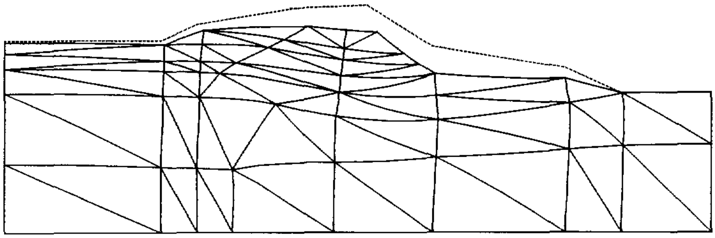

Figure 6.12. Deformed mesh (soft soil layers modelled with Plaxis Cap model) Deformations correspond to mesh scale.

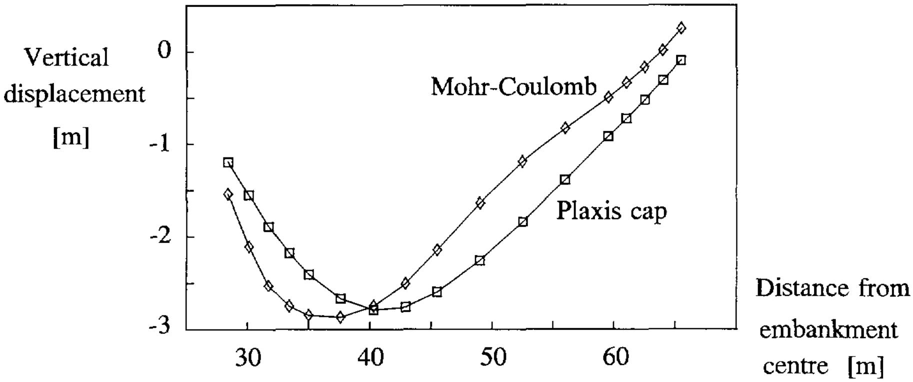

Figure 6.13. Comparison of vertical displacements at original soil surface

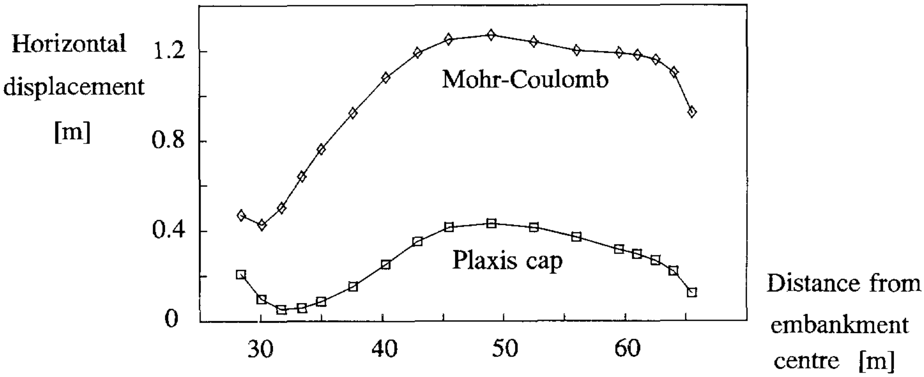

Figure 6.14. Comparison of horizontal displacements at original soil surface

Both models give approximately the same vertical settlements as indicated in Figure 6.13. This validates the choice of the shear modulus in the Mohr-Coulomb modelling from a viewpoint of one-dimensional compression. However, the horizontal displacements differ considerably. The calculation using the Plaxis Cap model gives the smallest horizontal displacements; the Mohr-Coulomb model predicts twice as large horizontal displacements. Field measurements indicate small horizontal displacements that agree quite well with the results of the Plaxis Cap model.

The overprediction of horizontal displacements by the Mohr-Coulomb model may be understood by considering pure shear. Indeed, the present embankment problem is governed by compression, but, in addition, shearing stresses will occur to promote horizontal displacements. For pure shearing we have:

Mohr-Coulomb $\Delta\gamma_{xy} = \Delta\sigma_{xy} \, / \, G_1$ (6.5a)

Plaxis Cap $\Delta\gamma_{xy} = \Delta\sigma_{xy} \, / \, G_{2\text{-}3}$ (6.5b)

In this respect reference is made to Section 4.4 were a tangential shear modulus was derived from the Plaxis Cap model for different stress paths. In the above relations G_1 is the low average shear modulus as derived for the Mohr-Coulomb model from one-dimensional compression. $G_{2\text{-}3}$ is the high modulus as obtained from a stress path with $\dot{p} = 0$, i.e. in between path 2 and path 3 of Figure 4.6a. The Plaxis Cap response to pure shear is most accurate as it is based on a more-or-less correct shear modulus. In contrast, the Mohr-Coulomb model predicts far too much shearing, as it involves the low G_1-shear modulus as needed for a proper prediction of vertical settlements.

For this project it was important to know the horizontal displacements inside the old embankment as this may cause fissures in the asphalt pavement. In general, horizontal displacements are very important for neighbouring structures such as piles, foundations, pipelines, etc. A wrong prediction of horizontal displacements can lead to loss of function of structures or to unnecessary expense to protect these structures. In such cases it is important to use a constitutive model that predicts the correct horizontal displacements.

7 LOCAL SOFTENING PLASTICITY

Rock, concrete and dense soils exhibit material softening under many conditions of loading. Here a material is said to undergo material softening when the second-order work is negative, i.e. $\dot{\underline{\sigma}}^T \dot{\underline{\varepsilon}} < 0$ in terms of rates of stress and strain. For rock and concrete it is a logical phenomenon as the micro-structural response to stress involves fissuring and thus weakening of the material. The behaviour of densely packed sand beyond peak strength generally shows a mild softening behaviour, which cannot be explained by cracking, but rather by dilation due to particle rearrangement. For dense clays, both fissuring and dilation would seem to be the cause of material softening.

In some soil tests, softening is quite severe, as one observes both material softening and geometrical softening due to bulging, necking or shear-banding. Indeed, material softening tends to induce such non-homogeneous deformations and thus geometrical softening. For general experimental evidence, the reader is referred to Read & Hegemier (1984). Note that the expression *geometrical softening* is used here rather than *structural softening* as for instance used by Schreyer & Chen (1986). This is because, in the current study, fissuring and cracking are considered to be material softening. On deriving constitutive models from experimental data, material softening needs to be isolated from geometrical softening as otherwise such models would obtain an overdose of material softening.

In geomaterials, softening behaviour is usually accompanied by the forming of a shear-band, i.e. a narrow band in which high deformation gradients occur. In sands one observes, for example, shear-bands with a well-defined thickness. Several researchers have reported shear-band thicknesses of the order of ten times the average grain size; see among others Desrues (1984) and Mühlhaus & Vardoulakis (1987). In clays and rock-like materials, the softening region is usually initiated by the development of a particular crack pattern, which may finally result in a shear-band mechanism. In this study the attention is focused rather on shear-band mechanisms than on crack forming.

From a mechanical point of view, the forming of shear-bands is the result of material instability. Indeed, material instability is obtained for a negative hardening modulus, as obtained in a softening model. However, apart from softening behaviour, the use of a non-associated flow rule may contribute to material instability as well, as clearly indicated by Rudnicki & Rice (1975).

In this Chapter softening is introduced by means of a Cam-Clay model, which will be described qualitatively. By focusing the attention on softening rather than hardening, this Cam-Clay model reduces to the simpler Drucker-Prager softening model. Both the Drucker-Prager model and the even simpler Von Mises softening model will be described in detail.

These two relatively simple models will be used in finite element calculations in order to show the breakdown of the classical approach of local plasticity when softening is introduced in the constitutive equations.

7.1 The Advanced Cam-Clay model

The Modified Cam-Clay model, as described in Section 4.1, is a model that includes softening behaviour for particular stress paths. As mentioned in the introduction to Section 4.1, the softening is generally overpredicted in that model. In order to simulate a more realistic softening behaviour, the so-called Hvorslev surface was introduced, i.e. a Mohr-Coulomb type yield criterion with a constant friction angle and hardening-softening on the cohesion. On combining the Hvorslev surface with a Modified Cam-Clay yield cap, one obtains a modern Cam-Clay model as described by Atkinson & Bransby (1978). Combined with proper flow rules, as presented in the following, one obtains the Advanced Cam-Clay model. Note that the addition *Advanced* has not been used in previous publications, but is introduced here.

The Advanced Cam-Clay model contains two yield functions and corresponding plastic potential functions. The first set of functions is valid for stress states where $p \geq \frac{1}{2}\, p_c$, and the second set of functions is valid for $p \leq \frac{1}{2}\, p_c$. It is obvious that the two yield functions should intersect at $p = \frac{1}{2}\, p_c$.

$$f_1 = \frac{q^2}{M^2} + p\,(p - p_c) \qquad g_1 = f_1 \qquad \text{for} \qquad p \geq \tfrac{1}{2}\, p_c \qquad (7.1a)$$

$$f_2 = q - \alpha\,(p + c\,\cot\varphi) \qquad g_2 = q - \beta\, p \qquad \text{for} \qquad p \leq \tfrac{1}{2}\, p_c \qquad (7.1b)$$

The first yield function f_1, and its associated plastic potential function g_1, relate to the Modified Cam-Clay model. The second yield function and its non-associated plastic potential relate to a Drucker-Prager model, i.e. the Hvorslev surface in stress space. Both yield functions are fully coupled and intersect at the Critical State Line (CSL). The cohesion c is considered to be a state-dependent variable and is directly related to the preconsolidation pressure p_c. It can easily be verified that:

$$c = \frac{M - \alpha}{2\,\alpha\,\cot\varphi}\, p_c \qquad (7.2)$$

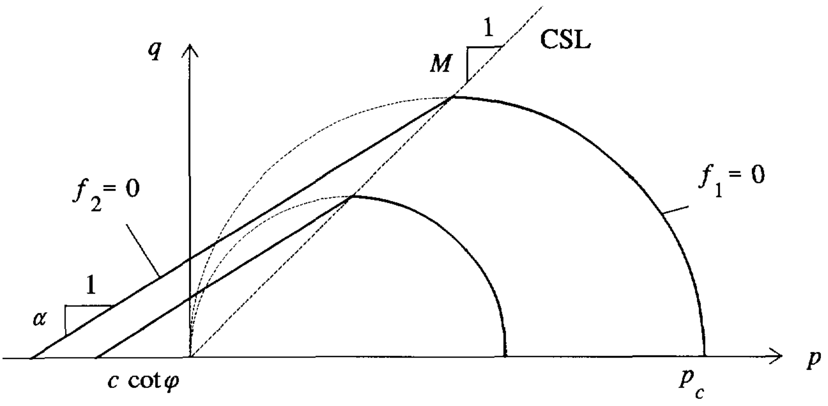

Figure 7.1 Yield locus of Advanced Cam-Clay model in (p,q)-plane for two different preconsolidation stresses

Figure 7.1 shows a plot of the yield locus in (p,q)-plane for two different values of p_c and corresponding c. The parameter M is the tangent of the CSL and relates the ultimate deviatoric stress q in Critical State to the mean stress p, i.e. when the material has reached a state of critical density due to plastic deformation. Hence, M can be regarded as an overall friction constant. It should be noted that the parameter M in the current model also determines the value of K_0 that results from the simulation of an oedometer test, but as in the Modified Cam-Clay model the value of M is based rather on the shear strength in Critical State than on K_0. Hence, the current model has the same shortcomings with respect to the modelling of one-dimensional compression as mentioned for the Modified Cam-Clay model in Section 4.2.

The parameter α represents the dependence of the shear strength on the mean stress and can thus also be regarded as a friction constant. It should be noted that the value of α is always smaller than the value of M.

The stress-dependent stiffness is formulated by means of a power law as described in Section 2.4 and involves a reference shear modulus G^{ref} corresponding to a reference pressure p^{ref}, and a power m (Equation 2.31). The hardening / softening rule of the Advanced Cam-Clay model relates the preconsolidation stress p_c to the volumetric plastic strain ε_v^p. Similar to the Plaxis Cap model of Section 4.3, the hardening rule obeys the same power law as the stress-dependent shear modulus. Note that in the current model the cap is part of an ellipse that crosses the **origin** of the stress space. This means that the hardening / softening rule is formulated in the exact isotropic preconsolidation pressure p_c and not in the stress measure p_c^* as used in the hardening rule of the Plaxis Cap model.

In the current model, an increase in the preconsolidation pressure p_c is associated with an increase in cohesion c and vice versa, as can be seen from Equation 7.2. For normally consolidated materials, stress paths with dominant isotropic loading are accompanied by compaction, i.e. an increase in volumetric plastic strain. Indeed, compaction is associated with an increase in cohesion. On the other hand, deviatoric loading on heavily overconsolidated materials is accompanied by dilation. Hence, the material becomes looser and this implies a degradation of the cohesive strength. This effect is fundamental for Cam-Clay type models.

7.2 A Drucker-Prager softening model

When considering deviatoric loading and shear deformation of heavily overconsolidated clays or rock-like material, the cap-hardening phenomenon is irrelevant, at least when adopting Cam-Clay type models. According to these models, the yield cap has been shifted far away by a former overburden pressure and a highly cohesive geomaterial remains. Hence, for rock-like material including heavily overconsolidated clays, it is sufficient to consider the softening Hvorslev surface only; the yield-cap plays no role at all.

This study is not meant to describe the softening behaviour of geomaterials in full detail, but attention is focused rather on the essentials of the softening phenomenon and on the numerical consequences. For this reason, the Hvorslev yielding is described by a Drucker-Prager model and not by the more accurate Mohr-Coulomb model.

A further simplification is made in the sense that the power m in the Advanced Cam-Clay model, similar to in Equations 4.32 and 4.34 of the Plaxis Cap model, is fixed at 0. This results in a constant stiffness modulus and a linear softening rule. The latter implies a linear relationship between the dilation and the cohesion softening, which can be formulated in rate form as:

$$\dot{c} = h' \, \dot{\varepsilon}_v^p \tag{7.3}$$

The softening rule 7.3 describes a linearly decreasing cohesion with decreasing volumetric plastic strain. Note that the volumetric strain rate is defined as positive for compression (see Section 2.1) and thus negative for dilation. As the cohesion decreases, the apex of the Drucker-Prager cone will move towards the origin of the principal stress space. On assuming a dilatant material with $\beta > 0$, this model predicts cohesion softening and no hardening at all.

For the formulation of the general stress-strain relation, most of the general equations from Section 3.1 on perfect plasticity are used. In fact, Equations 3.1 to 3.6 remain valid for softening plasticity. However, the consistency condition 3.7 is now replaced by:

$$\frac{\partial f^T}{\partial \underline{\sigma}} \dot{\underline{\sigma}} + \frac{\partial f}{\partial c} \dot{c} = 0 \tag{7.4}$$

Substitution of Equations 3.2 and 3.5 and the softening rule 7.3 into the above relation, gives an expression for the rate of the plastic multiplier:

$$\dot{\lambda} = \frac{1}{d+h} \frac{\partial f^T}{\partial \underline{\sigma}} \underline{\underline{D}}^e \dot{\underline{\varepsilon}} \tag{7.5}$$

The scalar d in this expression is similar to that in Section 3.1 and h is the softening modulus, which, in the current model, is defined as:

$$h = h' \beta \frac{\partial f}{\partial c} \qquad\qquad \frac{\partial f}{\partial c} = - \alpha \cot\varphi \tag{7.6}$$

Backsubstitution of Equation 7.5 into Equation 3.5 and successively into Equation 3.2 gives the full stress-strain relation:

$$\dot{\underline{\sigma}} = \left(\underline{\underline{D}}^e - \frac{1}{d+h} \underline{a} \, \underline{b}^T \right) \dot{\underline{\varepsilon}} \tag{7.7}$$

The vectors $\underline{a}$ and $\underline{b}^T$ were already defined in Equation 3.11. The above elastoplastic material matrix is linear, but generally non-symmetric due to the non-associated flow rule. In the next section attention is focused on the cohesion softening. Friction and dilation are neglected, so that one arrives at a Von Mises softening model.

7.3 A Von Mises softening model

The Von Mises model can be regarded as a Drucker-Prager model without friction. Indeed, the shear strength does not depend on the mean stress and is identical for compression and extension. The Von Mises model originates from metal plasticity, but it is also used to simulate the undrained behaviour of clay in a total stress analysis. In this section the model will be extended with linear softening in order to analyse the numerical consequences of softening.

The yield function of the Von Mises model can be formulated as:

$$f = q - 2\,c \tag{7.8}$$

Under conditions of a triaxial loading test the above yield criterion predicts the same failure load as the Tresca yield criterion, i.e. Mohr-Coulomb without friction. In order to obtain the same failure load as the Tresca yield criterion in a plane strain test, the factor 2 in the above yield function should be replaced by $\sqrt{3}$. For a verification of these factors the reader is referred to Chen (1975) or to Section 3.4 of this thesis.

The flow rule is associated so that the plastic potential function is equal to the yield function. The Von Mises model is unable to describe plastic volume strain such as compaction and dilation. All plastic deformation relates to deviatoric straining. Hence, the volumetric plastic strain ε_v^p cannot be used to control the cohesion softening. In order to formulate a proper softening rule for the current model, Equation 7.3 is reformulated as:

$$\dot{c} = -\,h'\,\dot{\kappa} \tag{7.9}$$

In this relation κ is the hardening parameter, which is generally defined as:

$$\dot{\kappa} = \sqrt{\frac{2}{3}\left((\dot{\varepsilon}^p_{xx})^2 + (\dot{\varepsilon}^p_{yy})^2 + (\dot{\varepsilon}^p_{zz})^2 + \frac{1}{2}\,(\dot{\gamma}^p_{xy})^2 + \frac{1}{2}\,(\dot{\gamma}^p_{yz})^2 + \frac{1}{2}\,(\dot{\gamma}^p_{zx})^2 \right)} \tag{7.10}$$

On evaluating the plastic strain components in the above expression according to the general formulation of plastic strains (Equation 3.5), it can be verified that, in the current model, the hardening parameter κ is equal to the plastic multiplier λ. Elaboration of the consistency condition and backsubstitution in the general stress-strain relation gives a similar expression as given in Equation 7.7. However, the hardening modulus h, as used in Equation 7.7, is defined, for the current model, as:

$$h = -\,2\,h' \tag{7.11}$$

Again, in order to correspond to the Tresca model under plane strain conditions, the factor 2 in the above relation should be replaced by $\sqrt{3}$. The current model is used in the next section to analyse the numerical consequences of softening.

7.4 Breakdown of the classical approach of local softening plasticity

The models presented in this chapter were derived according to the local plasticity formulation that is generally used for hardening models. This formulation is, in the current study, referred to as the *classical approach* and this term is introduced to emphasise the difference with new formulations as described in Chapter 8. In previous studies (Bazant, 1976) it has been shown that the use of softening models according to the classical approach of local plasticity results in severe mesh-dependence. Not only will the size of the elements influence the results, but also the orientation of the elements (mesh alignment). In this study it will be shown that there is another inconvenience that results from the use of softening models according to the classical approach, namely, a poorly converging and unstable equilibrium iteration process.

Both the Von Mises softening model and the Drucker-Prager softening model, as described above, were implemented in a finite element program using the implicit integration scheme of Section 5.3. In the following, some results of finite element calculations are presented. The calculations are performed with a varying number of high-order 15-noded triangular elements using 12-point Gaussian integration. Please note that the type of elements does not affect the consequences resulting from the numerical modelling. In fact, when using, for instance, 6-noded elements with 3-point Gaussian integration one also obtains mesh-dependent results and poorly converging equilibrium iterations.

For the equilibrium iterations, an elastic stiffness matrix is used in an accelerated initial stress procedure (Vermeer & Van Langen, 1989). An automatic load stepping procedure (Van Langen, 1991) is used throughout the calculations.

7.4.1 Biaxial test problem

The first example is a plane strain uniaxial loading test (biaxial test) on purely cohesive material, which softens after the ultimate shear strength is reached. The Von Mises softening model is used to simulate the material behaviour. The sample height is 250 mm and the width is 100 mm. The interaction at the bottom of the sample is considered to be rough (fully fixed). The vertical sides are free to move in any direction. An increasing vertical displacement is imposed at the top side, whilst the reaction force is monitored. The horizontal displacements at the top of the mesh are coupled in order to simulate the influence of a rough top platen. The self-weight of the material is ignored. The geometry and model parameters are shown in Figure 7.2.

Von Mises softening

Shear modulus $G = 1000$ kPa
Poisson's ratio $\nu = 0.3$
Initial cohesion $c_0 = 10$ kPa
Hardening modulus $h = 50\sqrt{3}$ kPa

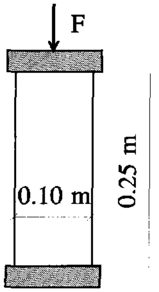

Figure 7.2 Model parameters and geometry of biaxial test

The initial cohesion is 10 kPa. In order to trigger a shear-band, a 10% reduced initial cohesion is applied to one Gauss-point at about a quarter of the height at the right-hand side. The above geometry was discretized in a finite element mesh with 12, 24, 48 and 96 elements respectively, as shown in Figure 7.3.

During the calculations, it was observed that the iteration process did not run as smoothly as a non-softening plasticity calculation usually does. As soon as a shear band has developed, the global stiffness, i.e. the increment of the reaction force divided by the displacement increment, should be constant because of the linear softening rule. However, the calculations showed a varying global stiffness. This is partly caused by an unstable failure mechanism in the sense that the direction and thickness of the shear-band altered during the calculations.

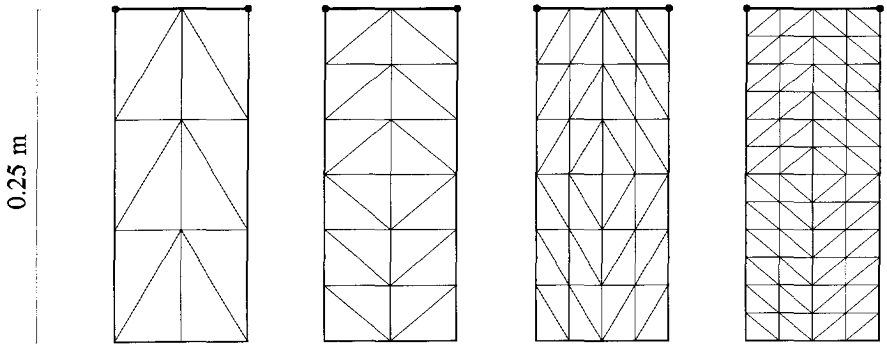

Figure 7.3 Different finite element meshes for biaxial test on cohesive material
a. 12 elements b. 24 elements c. 48 elements d. 96 elements

An example of an altering mechanism is shown in Figures 7.4 and 7.5 corresponding to the 24-element mesh. On comparing the plots b and c with the element mesh as shown in Figure 7.3b, it can be seen that the shear-band thickness is smaller if it coincides with an element side, and wider if it crosses an element. In the example underneath, the failure mechanism is indeed triggered by the point with reduced initial cohesion. However, in the case of the 48-element calculation, the failure mechanism is formed at a place that is different from the point with reduced cohesion.

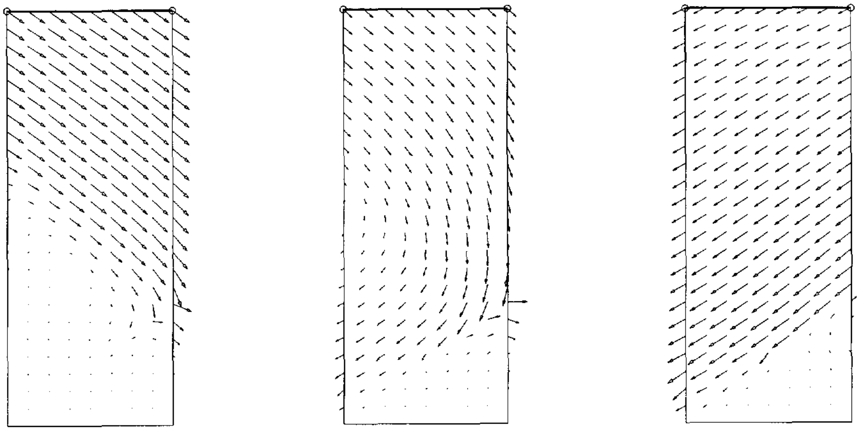

Figure 7.4 Incremental displacements showing alternating mechanism for mesh with 24 elements. a. Step 15 b. Step 20 c. Step 25

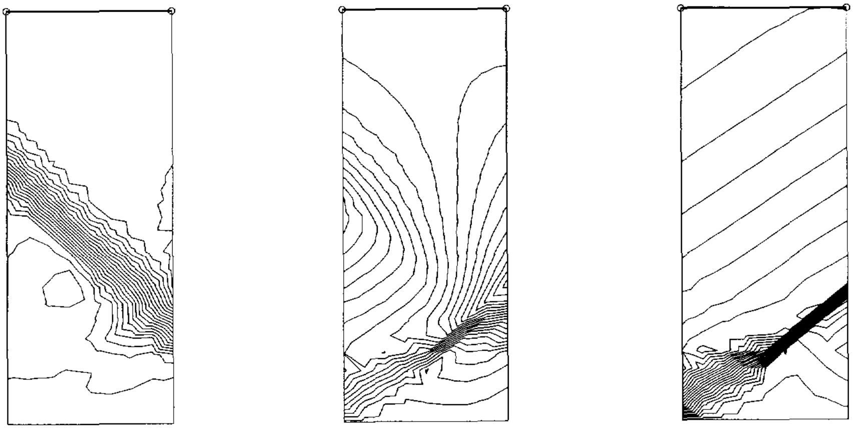

Figure 7.5 Contour lines of incremental displacements as shown in Figure 7.4
a. Step 15 b. Step 20 c. Step 25

In order to visualize the problems with the iteration process, a comparison is made in Figure 7.6 between results with the classical approach of softening plasticity and results obtained with a regularization method, as will be considered in the following chapters. The figure clearly shows the irregular step size and varying global stiffness obtained with the classical approach, whereas the second plot shows a much smoother curve with a reduced number of steps of about equal size. Note that the step size is chosen automatically, depending on the convergence speed in the iteration process (Van Langen & Vermeer, 1990). From this it can be concluded that the convergence in the classical approach is much worse than when applying a regularization.

Figure 7.7 shows the Force-Displacement curves of the four calculations with different meshes. A marker is drawn for every fifth calculation step. Up to the peak, the curves are virtually equal, but the behaviour after the peak differs considerably. There is definitely no convergence towards a particular softening slope when increasing the number of elements. The highest amount of softening occurs for the smallest shear-band thickness, which is obtained with the finest mesh. In that case, the Force-Displacement curve shows a so-called snap-back behaviour.

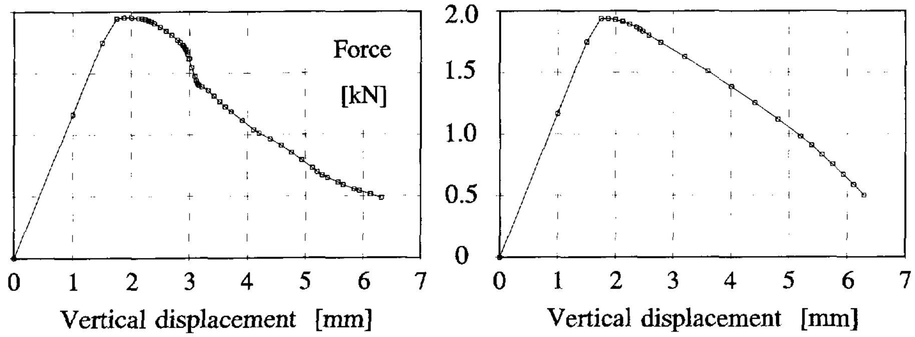

Figure 7.6 Comparison of Force-Displacement curves for biaxial test (24 element mesh)
a. Softening plasticity according to the classical approach
b. Softening plasticity with regularization method

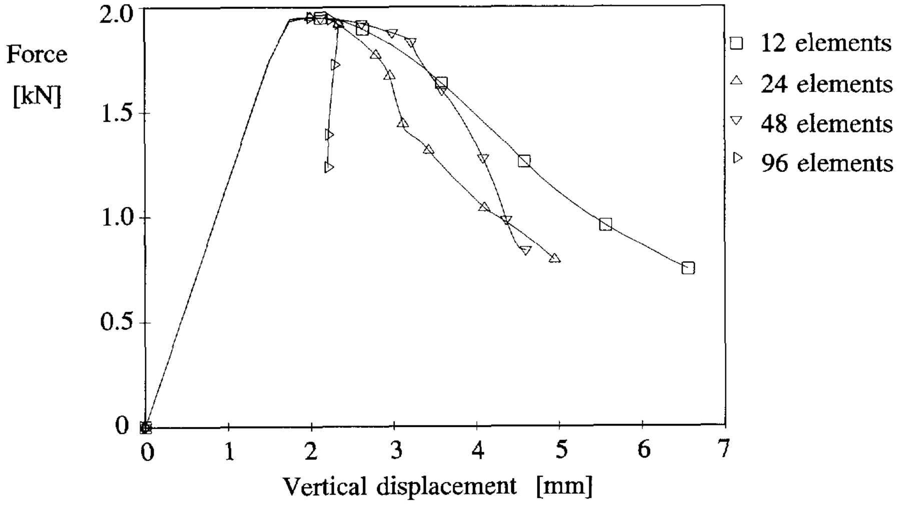

Figure 7.7 Force-Displacement curves of biaxial test problem for different meshes

7.4.2 Steep embankment slope

The second example is a steep embankment slope in frictional soil with some cohesive strength. The material behaviour is simulated with the Drucker-Prager softening model. There is no external load. The applied load is the self-weight of the material, which is increased as in a centrifuge test. The bottom of the mesh is fixed. The right-hand side can move in vertical direction and the horizontal direction is fixed because of considerations of symmetry. The remaining sides are free to move in any direction. The geometry and model parameters are listed in Figure 7.8.

Drucker-Prager softening

γ = 16 kN/m^3
G = 1000 kPa
ν = 0.4
c_0 = 10 kPa
φ = 20° (α = 0.58)
ψ = 10° (β = 0.30)
h = 200 kPa

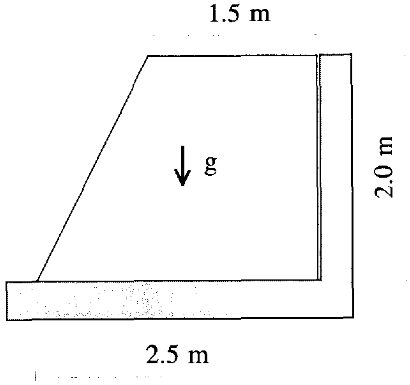

Figure 7.8 Model parameters and geometry of embankment

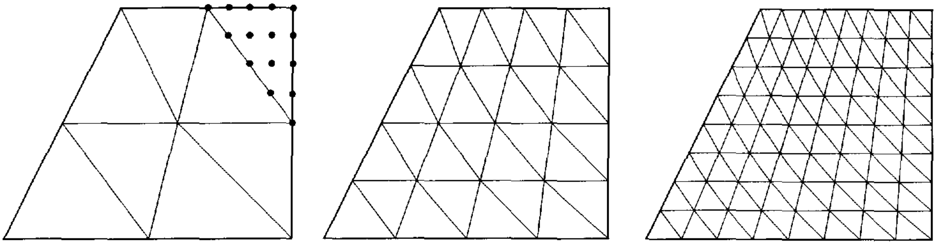

Figure 7.9 Three finite element meshes for embankment

The geometry is modelled by finite element meshes with 8, 32 and 128 elements respectively as shown in Figure 7.9. The tolerated global equilibrium error during the iteration process is 2% of the applied load. The computational results are plotted in Figure 7.10, which shows the gravity factor against the displacement of the embankment toe. The gravity factor is the multiplication factor for the material weight.

Apart from the difference in post-failure behaviour, Figure 7.10 clearly shows a difference in peak load between the three meshes. This means that, even if one is only interested in the pre-failure behaviour, mesh-dependence makes computational results doubtful. Indeed, on determining factors of safety on the basis of a peak load, one will be completely misled by results as indicated in Figure 7.10.

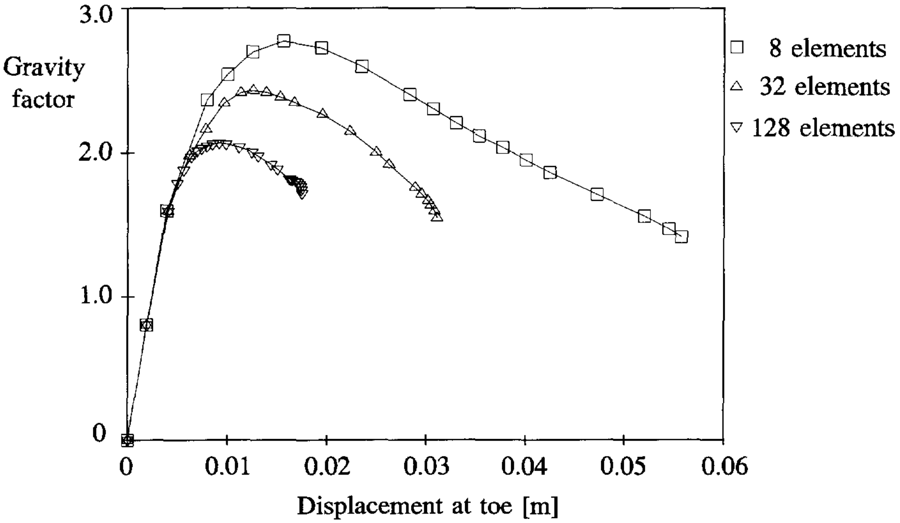

Figure 7.10 Load-displacement curves of embankment for different meshes

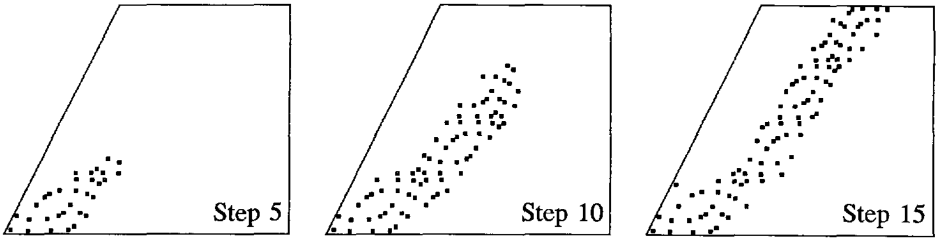

Figure 7.11 Development of plastic points for 32-element mesh

The mesh-dependence of the peak load can be explained by the fact that the localization zone develops gradually. Figure 7.11 shows that plasticity starts at the toe of the embankment and develops slantingly upwards to the top. When the plastic zone has just reached the top, the toe has already been softening for some time. As a result, the actual cohesion in the lower part may have reduced to the low residual value, whilst the actual cohesion in the upper part may still have its high initial value. The precise distribution of actual cohesion will depend on the softening that has occurred during the development of the plastic zone.

In a fine mesh, the deformation gradient across the plastic zone is sharp. This causes a large dilatancy effect and induces severe softening. As a result, the difference in cohesion between the top and the toe is considerable. For a coarse mesh it can be argued that the difference in cohesion is not too much. Hence, when using a fine mesh, integration of the shear strength along the localization zone gives a lower value than when using a coarse mesh. As a result, the peak load is lower in a finer mesh. It is mentioned here that in the 128-element mesh the peak load was passed even before the plastic zone had reached the top, i.e. before a full failure mechanism had developed.

It should be noted that the difference in peak load is **not** a result of the particular choice the of softening model. On choosing the simpler Von Mises softening model instead of Drucker-Prager softening, a similar effect will occur. In that case, however, the softening is not induced by dilatancy but by deviatoric plastic straining.

In addition to the mesh-dependence, it was also observed in the current example that, particularly after peak load, the convergence of equilibrium iterations was very poor. This is reflected in the curves for the 32-element mesh and the 128-element mesh in Figure 7.10. In these curves the markers, which indicate the load steps, clearly concentrate at the end. Hence, the step size decreases more and more towards the end. In fact, for the lower curve the calculation had to be stopped because of divergence of equilibrium iterations.

7.5 Conclusions on local softening plasticity

The two examples, one with the simple classical Von Mises softening model and one with the non-associated Drucker-Prager softening model, show that the computational results are strongly mesh-dependent. The mesh-dependence is not only manifest in the post-failure regime, but, for some particular problems, also in the pre-failure regime and the peak load. Moreover, it was observed that the equilibrium iterations deteriorate as soon as softening occurs. As yet, the latter phenomenon has not been reported by other researchers and therefore it merits some further comments. The phenomenon is definitely not related to the implementation of the model in the computer code, as it was observed that calculations with a non-negative hardening modulus show perfect convergence. Hence, this phenomenon relates to the use of softening, at least within the classical approach of local softening plasticity.

From the above observations it is concluded that the classical approach of plasticity is insufficient when using softening models in numerical applications.

8 REGULARIZATION TECHNIQUES FOR SOFTENING MODELS

Classical models for softening plasticity suffer from the drawback that any width of the localization zone is theoretically admissible, whereas experiments show a distinct relationship with a micro-structural length scale. Application of classical softening models in a numerical analysis results in severe mesh-dependence, as concluded in the previous chapter. This is due to the lack of a physical length scale so that this role is taken over by the numerical discretization. Moreover, it was observed that convergence towards a state of equilibrium using iterative procedures deteriorates when softening occurs. In the mathematical sense, the cause of these problems is the fact that the partial differential equation changes type in the transition from non-softening to softening, so that the boundary value problem becomes ill-posed. In the case of a dynamic analysis, wave velocities become imaginary, as already mentioned by Hadamard (1903). On applying so-called regularization techniques, the problems related with the use of softening models do not occur. At the beginning of this chapter an overview is presented of existing regularizations. In the remainder, attention is focused on a particular type of regularization, the non-local approach. Restriction is made in this chapter to a one-dimensional description.

8.1 Overview of existing regularization techniques

Classical softening models need to be extended in such a manner that they render a distinct thickness of shear-bands, rather than any value that happens to be favoured by the particular mesh being used in a numerical simulation. Such extensions of classical models are called regularizations.

One way of regularization is to include viscosity in the constitutive model. The use of viscoplastic (rate dependent) models as a regularization was, among others, discussed by Sandler & Wright (1984). Indeed, for dynamic problems the inclusion of viscosity might restore well-posedness. For relatively slow processes, i.e. near-static problems, the amount of viscosity which is required to retain well-posedness becomes unrealistically high. Hence, the results of such problems become doubtful, either because of mesh-dependence or because of the artificial viscosity. For purely static applications the viscoplastic regularization is not effective at all, so that in the current study, where only static problems are considered, this type of regularization is not taken into account.

Another way of regularization is based on the Cosserat continuum theory. This theory was originally introduced by Cosserat & Cosserat (1909). In addition to the displacement degrees-of-freedom that exist in the classical continuum theory, rotational degrees-of-freedom ω_j

appear in the Cosserat theory. The definition of shear strains is modified and involves the rotations ω_j. The spatial derivatives of rotations, i.e. curvatures κ_{ij}, enter the strain vector. The stress vector is extended with so-called couple-stresses m_{ij}. A relationship between the curvatures and the couple-stresses is included in the material matrix. This relationship involves an internal length parameter l. In addition to the equilibrium conditions, as formulated for the classical continuum theory, the Cosserat theory involves conditions for rotational equilibrium. As a result, extra boundary conditions, either on the rotation or on the couple-stress, are required to solve the boundary-value problem. In the general case when the couple-stresses are non-zero, the stress tensor becomes unsymmetric $(\sigma_{xy} \neq \sigma_{yx})$.
After some periods of varying popularity, the Cosserat theory was successfully applied by Mühlhaus (1986), who indicated its effectiveness as a regularization technique. Since then, several researchers have investigated the Cosserat theory for softening problems; see, among others, Vardoulakis (1989) and De Borst (1990). In a recent comparative study by Sluys (1992) it was concluded that this theory is only effective if shear deformation plays a dominant role. Besides, when doing finite element analyses, the internal length l must be large enough with respect to the element size to create a substantial influence of the "Cosserat-effect" and thus to become an effective regularization.

On reviewing regularizations, Sluys (1992) obtains by far the best results for another type of regularization: a strain-gradient model. One of the first researchers who included strain-gradients in the constitutive relation as a regularization method was Aifantis (1984), but the application of strain-gradients in continuum mechanics had already been described by Mindlin (1965). In a strain-gradient model higher-order spatial derivatives of strains are added to a particular part of the constitutive relation. Most of these models include a second-order gradient of the hardening parameter κ in the plasticity model; see among others Vardoulakis & Aifantis (1989). Some researchers consider a fourth-order gradient term as well (Zbib & Aifantis, 1989). In the classical theory of plasticity, as described in Section 3.1, one obtains a direct relationship between rates of stress and strain, i.e. between $\underline{\dot{\sigma}}$ and $\underline{\dot{\varepsilon}}$. On using a strain-gradient model one obtains a relationship between rates of stress and strain and the Laplacian of the hardening parameter, i.e. a relationship between $\underline{\dot{\sigma}}$, $\underline{\dot{\varepsilon}}$ and $\nabla^2 \dot{\kappa}$. The fact that the hardening parameter depends on the unknown plastic strain rates forms a serious difficulty when implementing such a model in a finite element code. Sluys (1992) overcomes this problem by introducing the hardening parameter κ as an extra independent variable in addition to the displacement components. In fact, the spatial derivatives of κ are introduced as variables as well, which results from the requirement of continuity of the Laplacian. This gives a significant expansion of degrees-of-freedom in a finite element analysis.

Based on the conclusions of Sluys (1992) it would seem that the strain-gradient method is a highly attractive regularization method for softening plasticity. However, the numerical implementation of such a model requires complex extensions of existing finite element codes, as described by Sluys (1992). Note that complex procedures can be avoided by adopting suitable approximations of the hardening parameter in terms of total strains instead of plastic strains. In this study an attempt was made to arrive at a simplified implementation by means of a direct calculation of the gradient terms. Indeed, this method is relatively easy to implement and appears to give proper mesh-independent results for some cases, but the procedure suffers from numerical scatter and is not robust enough for general applications.

The final type of regularization considered here is the non-local theory, which was not reviewed by Sluys (1992). In a fully non-local model a relation is established between average stresses and average strains. In early years, Eringen gave non-local formulations for elasticity (1972) as well as for plasticity (1981). Later, Bazant et al. (1984) formulated a non-local theory based on an imbricate model. Pijaudier-Cabot & Bazant (1987) and co-workers have extensively used the non-local theory in combination with damage models. Instead of considering a fully non-local stress-strain relationship, it is convenient to consider only a particular strain measure as non-local, whereas general stresses and strains remain local (Bazant et al, 1987). This enables a near-local treatment of the constitutive relation. In plasticity theory, such a model is obtained by formulating the hardening parameter as a non-local quantity. A disadvantage of such non-local models, as mentioned by De Borst and Mühlhaus (1991), is that elaboration of Prager's consistency condition for the determination of the plastic multiplier results in an integro-differential equation. Indeed, this would give complex numerical procedures, but the procedures can again be simplified by adopting suitable approximations of the hardening parameter in terms of total strains instead of plastic strains, as will be shown in Section 9.1.

On expanding a non-local model in Taylor series and omitting high-order derivatives, one obtains a strain-gradient model (Mühlhaus & Aifantis, 1991). Hence, a strain-gradient model can be seen as a particular case of a non-local model.

Besides these regularization methods, i.e. viscous models, Cosserat theory, strain-gradient and non-local models, there are some other simplified methods to provide mesh-independent softening behaviour. One of these methods is the technique as proposed by Pietruszczak & Mroz (1981). In their method they accept that the shear-band thickness is given by the numerical discretization, i.e. the element size, and they apply a multiplication factor in the softening rule, which is defined as the area of an element over the area of the shear-band. Other researchers have proposed the use of interface elements to model the localization zone (Charlier, 1992). In order to model the width of the localization accurately, special techniques on element level were introduced, as for instance finite elements with localization modes (Leroy et al., 1987) and adaptive remeshing techniques (Pastor et al., 1991). The latter method implies a continuous redistribution of elements in such a way that a very fine grid remains in zones where deformation is concentrated.

Indeed, all these techniques can provide a more-or-less predictable softening behaviour, but in a mathematical sense the boundary-value problem remains ill-posed. As a result, these methods will not solve the problem of poor convergence of iterative procedures. Nevertheless, some of these techniques can be combined with effective regularization methods in order to provide a regularization with a high degree of practical applicability.

Non-local theory:

In general, a fully non-local model is based on average stresses σ_{ij}^*, and average strains ε_{ij}^*, where

$$\sigma_{ij}^* = \frac{1}{A} \int\int\int w(x_n') \, \sigma_{ij}(x_n + x_n') \, dx_1' \, dx_2' \, dx_3' \tag{8.1}$$

$$\varepsilon_{ij}^* = \frac{1}{A} \int\int\int w(x_n') \, \varepsilon_{ij}(x_n + x_n') \, dx_1' \, dx_2' \, dx_3' \tag{8.2}$$

x_n' is a local coordinate with $n = 1, 2$ or 3. The symbol w denotes a weighting function, usually taken as the error function, and

$$A = \int\int\int w(x_n') \, dx_1' \, dx_2' \, dx_3' \tag{8.3}$$

A fully non-local model is obtained by introducing a relationship between average stress rates and average strain rates. The relationship between average stress and local stress complies with the relationship between macroscopic stress and microscopic stress for granular bodies. Thornton (1979), Christoffersen et al. (1981) and others have given definitions of the form:

$$\sigma_{ij}^* = \frac{1}{V_r} \int_{V_r} \sigma_{ij} \, dV \tag{8.4}$$

where V_r is a so-called representative volume; a small sphere around the material point considered. Hence, the macroscopic stress is an average of the more rapidly varying microscopic stress. Equation 8.1 simply reduces to Equation 8.4 when assuming a block-type function $w(x_n')$ with $w = 1$ in the interior of V_r and $w = 0$ outside the representative sphere. Similarly, ε_{ij}^* and ε_{ij} can be conceived as macroscopic strain and microscopic strain respectively. The distinction between macroscopic and microscopic quantities becomes manifest in the case of localized deformation. It is basically because of this clear physical background that preference is given in this study to the non-local theory.

Instead of a well-defined area of influence, as expressed by a block-type weighting function, it is more reasonable to assume that the non-local character of a constitutive relationship fades away for larger distances. This effect can be expressed by a particular choice of the weighting function. A suitable function that represents this property is the error function.

$$w(r) = \frac{1}{l\sqrt{\pi}}\, e^{-\left(\frac{r}{l}\right)^2} \tag{8.5}$$

In this function r is the distance from any material point to the point where the average is taken, and l is an internal length parameter, which is related to the width of the localization zone. In theory, even far remote points contribute to the average, but in practice the influence is restricted to points within a distance of only a few times the internal length. For example, the contribution of a point at distance $r = 2\, l$ is only 1.83% of the contribution of the central point and the influence of a point at distance $r = 3\, l$ is about 0.1%. Other functions with this property exist, such as goniometric functions, but the difference in the resulting average is small.

8.2 The existing non-local softening plasticity model

For the sake of simplicity, the existing non-local theory of plasticity is applied to a one-dimensional tension bar of infinite length $(-\infty < x < \infty)$. Only one local stress component σ and one local strain component ε are taken into account. The non-local formulation is restricted to the softening rule. The relations for the one-dimensional elastoplastic behaviour are given below:

$$\dot{\varepsilon} = \dot{\varepsilon}^e + \dot{\varepsilon}^p \qquad \text{(basic rule of elastoplasticity)} \tag{8.6}$$

$$\dot{\sigma} = E\, \dot{\varepsilon}^e = E\, (\dot{\varepsilon} - \dot{\varepsilon}^p) \qquad \text{(elastic stress-strain relation)} \tag{8.7}$$

$$f = \sigma - \sigma_t \qquad \text{(yield function)} \tag{8.8}$$

E is Young's modulus of elasticity and σ_t is the tensile strength, which obeys a simple linear non-local softening rule:

$$\dot{\sigma}_t = -h\, \dot{\varepsilon}^* \tag{8.9}$$

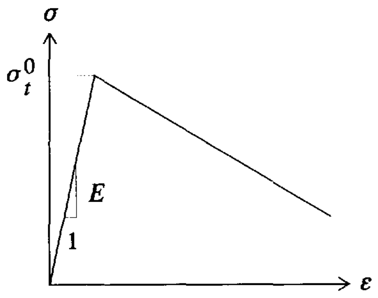

Figure 8.1 One-dimensional stress-strain relation

In this relation h is the softening modulus. The softening is controlled by an auxiliary non-local strain rate $\dot{\varepsilon}^*$. In accordance with Bazant et al. (1987), the non-local strain rate is defined as:

$$\dot{\varepsilon}^*(x) = \frac{1}{A} \int_{-\infty}^{\infty} w(r)\ \dot{\varepsilon}^p(x+r)\ dr \tag{8.10}$$

The weighting function $w(r)$ is chosen as the error function as defined in Equation 8.5. The value A represents the integral of the weighting function over the domain, as defined in Equation 8.3.

The aim of the non-local model is to obtain a well-posed boundary value problem, resulting in mesh-independency and good convergence of numerical procedures. However, to the author's experience, one-dimensional calculations using the existing non-local model in this form still resulted in localization in a single point. Hence, the results were not objective with respect to the schematization. Moreover, the convergence during the iteration process was very poor. Two-dimensional calculations gave slightly better results, but full mesh-independence was not obtained. A qualitative explanation will be given below for the fact that the current non-local formulation is not effective as a regularization method for one-dimensional applications.

Consider again a one-dimensional softening tension bar with a small imperfection, i.e. a small section where the initial tensile strength σ_t^0 is slightly lower than in the rest of the bar. Due to this fact, at the onset of plasticity the plastic strain is concentrated in this weak zone as shown in Figure 8.2a. Note that the precise shape of the plastic strain is of no importance, but the simple block function in Figure 8.2a is considered for convenience.

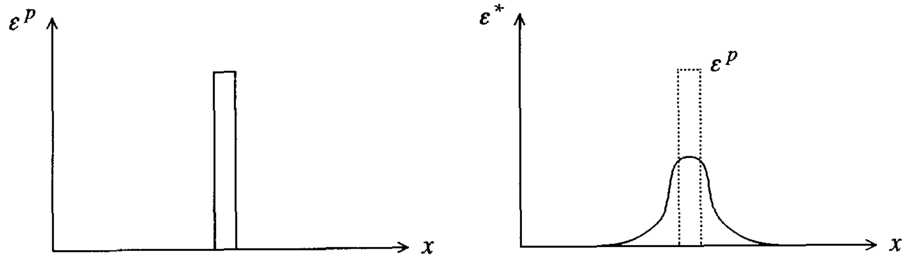

Figure 8.2 Distribution of strain in a bar with an imperfection
a. Plastic strain at the onset of plasticity
b. Non-local strain that follows from ε^p

The non-local strain ε^* is a redistribution of the plastic strain ε^p, which always results in a smoother distribution.

For the distribution of the plastic strain as considered in Figure 8.2a the non-local strain looks like a Gaussian curve as visualised in Figure 8.2b. The exact shape is influenced by the choice of the weighting function. In general, the maximum will be in the centre of the imperfection. According to the non-local softening rule, the material will soften mostly in this centre point. As a consequence, the plastic strain is more and more concentrated in the centre point and cannot spread in order to become a fully developed localization zone. If the non-local strain were such that the maximum extended to the edges of the plastic zone, the material would soften in a wider range and the plastic strain would spread to become a full localization zone. These considerations led to the formulation of a modified non-local plasticity model, which is presented in the next section.

8.3 A modified non-local softening plasticity model

In this modified non-local formulation a new non-local strain rate is introduced which consists of a local and a purely non-local part. It will be shown that this new formulation is indeed effective and does not suffer from the problems that occur in the existing non-local formulation.

For the case of the one-dimensional tension bar, as introduced in the previous section, the new non-local strain rate can be written as:

$$\dot{\varepsilon}^*(x) = (1-\alpha)\,\dot{\varepsilon}^p(x) + \frac{\alpha}{A}\int_{-\infty}^{\infty} w(r)\,\dot{\varepsilon}^p(x+r)\,dr \tag{8.11}$$

In this formulation α is a new parameter, the value of which can be chosen more-or-less arbitrarily. Note that for $\alpha = 0$ the classical (local) theory is obtained. For $\alpha = 1$ the above expression is equal to the non-local formulation as given in Equation 8.10. Hence, based on the considerations at the end of the previous section, the current formulation cannot be effective for $\alpha = 1$. As α is increased, one makes sure that zones of low plastic strains ε^p get higher non-local strains ε^*. At the same time zones of high plastic strains get lower non-local strains upon an increasing α.

To illustrate the effect of α, the imperfection of Figure 8.2a is considered again. The weighting function in Equation 8.11 is again taken as the error function according to Equation 8.5. For $\alpha = 1$, the block-type distribution of ε^p results in the Gaussian-type distribution of Figure 8.2b for ε^*. The distribution of the non-local strain for $\alpha > 1$ is plotted in Figure 8.3a. It can be seen that ε^* has a maximum at the edges of the plastic zone. As a result, at these points the highest amount of softening occurs. This induces a converging redistribution of plastic strains in such a way that the non-local strain will finally be constant over a particular width, as plotted in Figure 8.3b. Hence, an effective non-local regularization is obtained for $\alpha > 1$. Note that $\alpha < 1$ cannot be effective, so that this case is not taken into consideration at all.

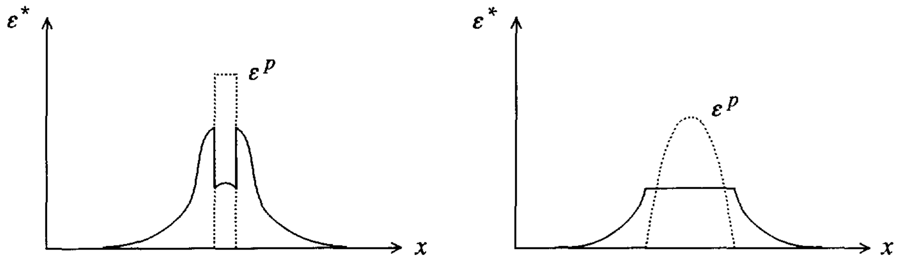

Figure 8.3 Distribution of non-local strain in the modified non-local method for $\alpha > 1$
a. Initial distribution b. Final distribution

8.4 Analytical solution for the modified non-local model

In this section it will be shown that the modified non-local model allows for an analytical solution. It is important to note that the analytical solution given here is directly based on the non-local formulation and not on a differential approximation as presented by Bazant and Zubelewicz (1988). The analytical solution confirms the observation that for the existing non-local formulation (or $\alpha = 1$ in the modified non-local formulation) the localization zone reduces to a point.

Consider now necking of the tension bar in which the plastic strain rate is formulated as:

$$\dot{\varepsilon}^p(x) = -\frac{\dot{\sigma}}{h}\,(1 + \cos x') \qquad\qquad x' = \frac{2\,\pi\,x}{L} \tag{8.12}$$

with $-\infty < x < \infty$ and L being the width of the localization zone. In fact, necking is a type of geometrical softening, but it can conveniently be modelled using a one-dimensional (material) softening model. In reality, a neck will occur very locally for $-L/2 \leq x \leq L/2$ and outside this zone the plastic strain vanishes. However, for convenience, periodic necking is considered with Equation 8.12 valid for any value of x. It will be shown that this periodic necking is an analytical solution of the modified non-local model.

The expression for the plastic strain rate as given in Equation 8.12 substituted into Equation 8.11 with the weighting function of Equation 8.5 gives:

$$\dot{\varepsilon}^*(x) = -\frac{\dot{\sigma}}{h}\left[(1-\alpha)\,(1+\cos x') + \frac{\alpha}{A}\int_{-\infty}^{\infty}\frac{1}{l\sqrt{\pi}}\,e^{-\left(\frac{r}{l}\right)^2}\big(1 + \cos(x'+r')\big)\,dr\right] \tag{8.13}$$

where $r' = 2\pi r\,/\,L$. In the integral the cosine can be split into two parts using the standard goniometric rule $\cos(x'+r') = \cos x' \cos r' - \sin x' \sin r'$. Hence, Equation 8.13 becomes:

$$\dot{\varepsilon}^* = -\frac{\dot{\sigma}}{h}\left[1 - \alpha + (1-\alpha)\cos x' + \frac{\alpha}{A}\int_{-\infty}^{\infty}\frac{1}{l\sqrt{\pi}}\,e^{-\left(\frac{r}{l}\right)^2}dr \,+ \right. \tag{8.14}$$

$$\left. + \frac{\alpha}{A}\cos x'\int_{-\infty}^{\infty}\frac{1}{l\sqrt{\pi}}\,e^{-\left(\frac{r}{l}\right)^2}\cos r'\,dr - \frac{\alpha}{A}\sin x'\int_{-\infty}^{\infty}\frac{1}{l\sqrt{\pi}}\,e^{-\left(\frac{r}{l}\right)^2}\sin r'\,dr\right]$$

The integrals in the above expression have a particular form. According to Gröbner & Hofreiter (1961) the integrals can be evaluated as:

$$\int_{-\infty}^{\infty} \frac{1}{l\sqrt{\pi}}\, e^{-\left(\frac{r}{l}\right)^2} dr = A = 1 \tag{8.15a}$$

$$\int_{-\infty}^{\infty} \frac{1}{l\sqrt{\pi}}\, e^{-\left(\frac{r}{l}\right)^2} \cos r' \; dr = e^{-\left(\frac{\pi l}{L}\right)^2} \tag{8.15b}$$

$$\int_{-\infty}^{\infty} \frac{1}{l\sqrt{\pi}}\, e^{-\left(\frac{r}{l}\right)^2} \sin r' \; dr = 0 \tag{8.15c}$$

Substitution of Equations 8.15 into Equation 8.14 gives:

$$\dot{\varepsilon}^*(x) = -\frac{\dot{\sigma}}{h}\left[1 + (1-\alpha)\cos x' + \alpha \cos x' \, e^{-\left(\frac{\pi l}{L}\right)^2}\right] \tag{8.16}$$

In order to obtain a stable localization zone, the amount of softening should be constant and maximal within the range $-L/2 \leq x \leq L/2$. This is obtained if the non-local strain rate $\dot{\varepsilon}^*$ is constant within the localization zone, i.e. independent from x, which means that the derivative with respect to x should be zero:

$$\frac{d\dot{\varepsilon}^*(x)}{dx} = -\frac{\dot{\sigma}}{h}\left[-(1-\alpha)\frac{2\pi}{L}\sin x' - \alpha\frac{2\pi}{L}\sin x' \, e^{-\left(\frac{\pi l}{L}\right)^2}\right] = 0 \tag{8.17}$$

Elaboration of Equation 8.17 yields an expression for the width of the localization zone L, which appears to be a function of α:

$$L = \frac{\pi\, l}{\sqrt{\ln(\alpha) - \ln(\alpha - 1)}} \tag{8.18}$$

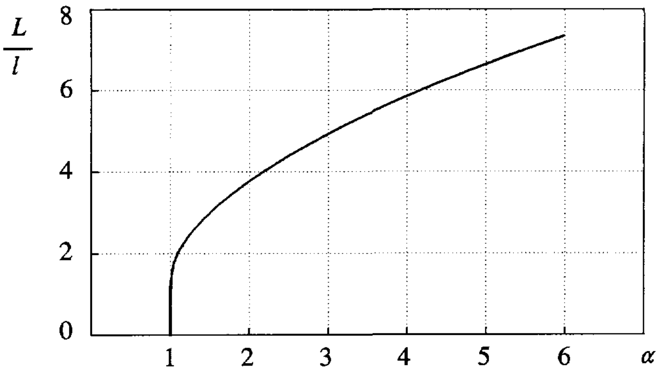

Figure 8.4 Width of the localization zone as a function of α

The relation between L and α is plotted in Figure 8.4. From this relation it can be seen that α must be greater than 1 in order to have a well-defined finite width. In the limiting case of α approaching unity, the width of the localization zone reduces to zero. In the limiting case of α going to infinity, the width of the localization zone also goes to infinity.

$$\lim_{\alpha \downarrow 1} L(\alpha) = 0 \qquad \lim_{\alpha \to \infty} L(\alpha) = \infty \tag{8.19}$$

Hence, the existing non-local theory $(\alpha = 1)$ does not produce a solution to the necking problem. One needs a factor α as used in the modified theory presented here. For $\alpha > 1$ the theory incorporates a sound analytical solution for the necking problem.

Preliminary conclusion: the fact that the modified non-local theory allows for an analytical solution of the necking problem creates some confidence in this approach. It is surprising that the analytical solution is relatively independent of the particular value of the constant α being used. Indeed, on changing its value one can also change the value of the internal length parameter l in such a manner that the width of the neck remains constant. Many combinations of α and l will give the same neck, as can be seen from Equation 8.18. At the same time such combinations theoretically give the same strain distribution within the neck. As a consequence, all these combinations of α and l also provide the same rate of elongation in a tension test. On using the analytical solution to evaluate the rate of elongation, one obtains for a bar with a single neck:

$$\dot{L}_{bar} = \int \dot{\varepsilon}\, dx = \int (\dot{\varepsilon}^e + \dot{\varepsilon}^p)\, dx = \dot{\sigma} \left[\frac{L_{bar}}{E} - \frac{L}{h} \right] \tag{8.20}$$

8.5 Discussion of the analytical solution

In reality, localization will only occur in a single neck and not in periodic necks as considered in the analytical solution. In the following it will be evaluated to what extent the analytical solution, as given in Equation 8.12 and the corresponding width of the localization zone, as given in Equation 8.18, apply to real non-periodic necking.

To this end the relationship 8.11 between the non-local strain rate and the plastic strain rate is considered. In fact, this relationship can be conceived as an averaging procedure. The averaging procedure is visualised in Figure 8.5. In this plot the large curves represent the periodic plastic strain rate ε^p, as defined by Equation 8.12. The smaller curve is the weighting function w, as defined by Equation 8.5. The non-local strain is largely determined by the product between w and ε^p. Let us first consider a point near the centre of the neck as illustrated in Figure 8.5a. Here the non-local strain of point A is determined by the shaded plastic strains. Plastic strains outside the shaded area have hardly any influence. Hence, for near-centre points, such as point A in Figure 8.5a, the periodicity of the analytical solution has hardly any influence. For near-edge points the situation is different. Consider for example point B as indicated in Figure 8.5b. Again, the influence zone is indicated by shaded plastic strains. Point B is positioned in the same neck as point A, but not entirely determined by the plastic strains within this neck. Indeed, a smaller part of the shaded area is located in another neck on the left-hand side. Hence, near-edge points in single necks will differ from near-edge points in periodic necks. As a consequence, single necks will not exactly match the periodic necks considered here. It can be argued that single necks will be somewhat narrower than periodic necks, but differences will be smaller when larger values of α are considered. Indeed, for a given internal length l, the width of necks increase as α is increased. As a consequence, the w-curves in Figure 8.5 become small with respect to the ε^p-curves.

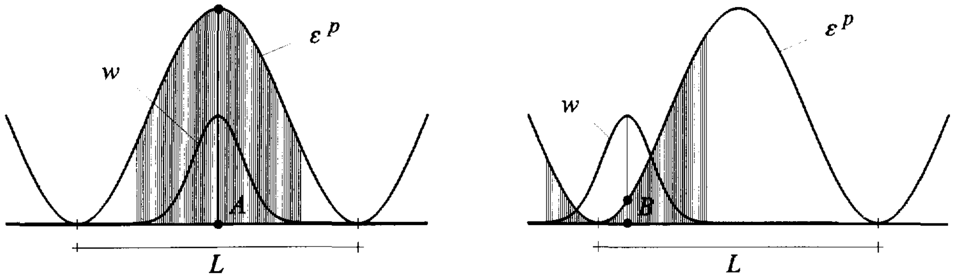

Figure 8.5 Plastic strain rate for periodic necking and weighting function w, for computation of non-local strain rate ε^*.

a. Weighting function for near-centre point

b. Weighting function for near-edge point.

8.6 Comparison with the strain-gradient theory

The strain-gradient theory is another effective regularization technique to provide well-posedness in softening problems. According to the gradient theory the auxiliary strain rate $\dot{\varepsilon}^*$ can be formulated as:

$$\dot{\varepsilon}^*(x) = \dot{\varepsilon}^p(x) + \frac{l_g^2}{4} \frac{d^2\dot{\varepsilon}^p(x)}{dx^2} \tag{8.21}$$

l_g is an internal length parameter; the subscript g has been added in order to emphasise the difference with the non-local theory.

Similar to the modified non-local theory, the strain-gradient theory also allows for an analytical solution of the necking problem (De Borst & Mühlhaus, 1991). In fact, the analytical solution is identical to the solution as given in Section 8.4, and Equation 8.12 applies to the strain-gradient theory as well. However, in this case the solution is also exact for a single neck. The width of the localization zone is found to be:

$$L_g = \pi\, l_g \tag{8.22}$$

Considering the results as presented by De Borst & Mühlhaus (1991) and the intensive study by Sluys (1992), it can be concluded that the strain-gradient model is indeed effective as a regularization technique. In fact, the strain-gradient theory would be very satisfying if its numerical implementation were not so awkward. Comparison of Equation 8.22 with equation 8.18 shows that both theories give the same width of the localization zone when using:

$$l = l_g \sqrt{\ln\left[\frac{\alpha}{\alpha - 1}\right]} \qquad \text{or} \qquad \alpha = \frac{\exp(l^2 / l_g^2)}{\exp(l^2 / l_g^2) - 1} \tag{8.23}$$

As it remains a powerful regularization technique, a comparison is made it with the modified non-local theory. From Equation 8.23 it follows that the internal length parameter l, as used in the modified non-local model, is not equal to the internal length l_g, as used in the strain-gradient model. Only for the special case of $\alpha \approx 1.58$ do both parameters coincide.

The strain-gradient theory might be conceived as an approximation of the non-local theory. Indeed, on expanding the non-local strain rate as defined by Equation 8.10 in a Taylor series around $r = 0$, one obtains

$$\dot{\varepsilon}^*(x) = \frac{1}{A}\int_{-\infty}^{\infty}\frac{1}{l\sqrt{\pi}}\,e^{-\left(\frac{r}{l}\right)^2}\,\dot{\varepsilon}^p(x)\,dr + \frac{1}{A}\int_{-\infty}^{\infty}\frac{r}{l\sqrt{\pi}}\,e^{-\left(\frac{r}{l}\right)^2}\,\frac{d\dot{\varepsilon}^p(x)}{dx}\,dr +$$

$$+\frac{1}{A}\int_{-\infty}^{\infty}\frac{r^2}{2\,l\sqrt{\pi}}\,e^{-\left(\frac{r}{l}\right)^2}\,\frac{d^2\dot{\varepsilon}^p(x)}{dx^2}\,dr + \frac{1}{A}\int_{-\infty}^{\infty}\frac{r^3}{6\,l\sqrt{\pi}}\,e^{-\left(\frac{r}{l}\right)^2}\,\frac{d^3\dot{\varepsilon}^p(x)}{dx^3}\,dr + \ldots \tag{8.24}$$

Every odd derivative term falls off in this Taylor expansion, and it follows that:

$$\dot{\varepsilon}^*(x) = \dot{\varepsilon}^p(x) + \frac{l^2}{4}\,\frac{d^2\dot{\varepsilon}^p(x)}{dx^2} + \textit{higher-order derivatives} \tag{8.25}$$

The difference between Equation 8.25 and Equation 8.21 is just the higher-order derivatives. In general, Taylor expansions give accurate approximations after a few terms. For this reason researchers are inclined to think that the higher-order derivatives in Equation 8.25 are negligible. However, from the fact that the strain-gradient model is effective and the non-modified non-local model is not, it can already be concluded that the higher-order derivative terms in Equation 8.25 have an important influence and that they are certainly not negligible.

It is concluded that the modified non-local theory and the strain-gradient theory provide very similar solutions to the necking problem, although internal length parameters play somewhat different roles. However, for the special choice of $ln(\alpha) - ln(\alpha\text{-}1) = 1$ $(\alpha \approx 1.58)$, their internal length parameters are equivalent.

8.7 One-dimensional numerical implementation

Finite element application of the modified non-local softening model involves an incremental approach where an iterative procedure is used to satisfy the equilibrium condition. To be sure about convergence, an elastic stiffness matrix is used in an accelerated initial stress procedure (Vermeer & Van Langen, 1989). The writer has great doubts about the use of a tangent stiffness matrix for the current non-local model. An exact formulation of the tangent matrix is virtually impossible. An approximated tangent matrix based on the assumption that the non-local strain rate can be approximated by the local plastic strain rate, yields a stiffness matrix that would produce much too soft a structural response. Performing equilibrium iterations with such a matrix tends to give convergence problems. An elastic stiffness matrix does definitely not suffer from these problems and has therefore been adopted.

The calculation procedure is similar to ordinary local finite element calculations that involve initial stress-type procedures. An essential subroutine is the computation of stress increments for given strain increments. Therefore this topic will be described in full detail.

Time integration of Equations 8.7 and 8.9 respectively yields:

$$\Delta\sigma = E\,(\Delta\varepsilon - \Delta\varepsilon^p) \tag{8.26}$$

$$\Delta\sigma_t = -h\,\Delta\varepsilon^* \tag{8.27}$$

In the case of elastic behaviour, the plastic strain increment and the non-local strain increment are zero. For plastic behaviour, the non-local strain increment $\Delta\varepsilon^*$ is obtained by time integration of Equation 8.11. Substitution of the plastic strain increment $\Delta\varepsilon^p$ by $\Delta\varepsilon - \Delta\varepsilon^e$ gives:

$$\begin{aligned}\Delta\varepsilon^*(x) = {} & (1-\alpha)\left(\Delta\varepsilon(x) - \Delta\varepsilon^e(x)\right) + \\ & + \frac{\alpha}{A}\int_{-\infty}^{\infty}\frac{1}{l\sqrt{\pi}}\,e^{-\left(\frac{r}{l}\right)^2}\left(\Delta\varepsilon(x+r) - \Delta\varepsilon^e(x+r)\right)dr\end{aligned} \tag{8.28}$$

In a one-dimensional application the elastic strain increment $\Delta\varepsilon^e$ can be directly calculated from the applied stress increment. Hence, the non-local strain increment is related with the total strain increment $\Delta\varepsilon$ rather than with the plastic strain increment $\Delta\varepsilon^p$. For a homogeneous bar the elastic strain increment is constant, which gives:

$$\frac{1}{A}\int_{-\infty}^{\infty}\frac{1}{l\sqrt{\pi}}\,e^{-\left(\frac{r}{l}\right)^2}\Delta\varepsilon^e(x+r)\,dr = \Delta\varepsilon^e(x) \tag{8.29}$$

Hence, the non-local strain increment can be written as:

$$\Delta\varepsilon^*(x) = \Delta\varepsilon^p(x) - \alpha\,\Delta\varepsilon(x) + \frac{\alpha}{A}\int_{-\infty}^{\infty}\frac{1}{l\sqrt{\pi}}\,e^{-\left(\frac{r}{l}\right)^2}\Delta\varepsilon(x+r)\,dr \tag{8.30}$$

Using this equation, one computes the non-local strain in a material point from a given distribution of physical strain. Hence, the entire strain distribution must be known before any non-local strain can be computed.

For a material point in plastic state which is subject to loading, the change of stress is such that the new state of stress complies with the yield condition. As a result, the value of the yield function is zero at the end of the time-step i:

$$f(\sigma^i) = 0 \qquad \sigma^i = \sigma_t^i \tag{8.31}$$

where

$$\sigma^i = \sigma^{i-1} + \Delta\sigma \qquad \sigma_t^i = \sigma_t^{i-1} + \Delta\sigma_t \tag{8.32}$$

Substitution of the Equations 8.32 for the current stress and tensile strength into Equation 8.31, with the help of Equations 8.26, 8.27 and 8.30, yields an expression for the plastic strain increment:

$$\Delta\varepsilon^p = \frac{1}{E-h}\left[\sigma^{i-1} - \sigma_t^{i-1} + (E-\alpha h)\,\Delta\varepsilon + \frac{\alpha h}{A}\int_{-\infty}^{\infty}\frac{1}{l\sqrt{\pi}}\,e^{-\left(\frac{r}{l}\right)^2}\Delta\varepsilon(r)\,dr\right] \tag{8.33}$$

Note that this expression for the plastic strain increment is exact, even in the case of a transition from elastic to plastic behaviour. In case the material point was already in plastic state at the end of the previous time-step, the term $\sigma^i - \sigma_t^{i-1}$ in the above expression is cancelled.

Backsubstitution of the plastic strain increment into Equation 8.26 gives the final stress increment. The calculation of the stress increment is summarized in Table 8.1 on the next page.

Table 8.1 Calculation of stress increment for a given strain increment

```
$\Delta\sigma = E\,\Delta\varepsilon$
$f = \sigma^{i-1} + \Delta\sigma - \sigma_t^{i-1} - \alpha h \Delta\varepsilon + \frac{\alpha h}{l\sqrt{\pi}} \int_{-\infty}^{\infty} e^{-\left(\frac{r}{l}\right)^2} \Delta\varepsilon(r)\, dr$
if $f > 0$ then
    $\Delta\varepsilon^p = \frac{f}{E - h}$
    $\Delta\sigma = \Delta\sigma - E\,\Delta\varepsilon^p$
    $\Delta\sigma_t = -h\Delta\varepsilon^p + \alpha h \Delta\varepsilon - \frac{\alpha h}{l\sqrt{\pi}} \int_{-\infty}^{\infty} e^{-\left(\frac{r}{l}\right)^2} \Delta\varepsilon(r)\, dr$
end if
$\sigma^i = \sigma^{i-1} + \Delta\sigma$
$\sigma_t^i = \sigma_t^{i-1} + \Delta\sigma_t$
```

8.8 Numerical versus analytical solution

Again the necking problem for a tension bar is considered, but now the problem is solved numerically. One of the aims is to verify mesh-independence of the modified non-local theory. Hence the problem is to be solved for various meshes with different finesses. The second aim is to verify whether or not the analytical solution is approximately retrieved; both for the width of the neck and for the rate of elongation of the tension bar. To investigate this in detail, two combinations of α and l will be considered which should give the same localization width of $L = 31.42$ mm. The calculations are fully determined by the data as listed in Table 8.2.

Table 8.2 Data of the one-dimensional tension bar

Length of bar	L_{bar}	= 100 mm
Young's modulus	E	= $20 \cdot 10^6$ kPa
Softening modulus	h	= $2 \cdot 10^6$ kPa
Initial strength	σ_t^0	= $2 \cdot 10^3$ kPa
Amplification factor	α	= 2.000 and 6.763
Internal length	l	= 8.326 and 4.000
Number of elements	N	= 5, 15, 35 and 75

High-order 5-noded line elements are used, but lower-order line elements could be used as well. Calculations are done with four Gaussian integration points per 5-noded element. For all calculations a neck was triggered by means of a small perturbation; the tensile strength of the most central Gaussian integration point was reduced by 0.1 percent. The extension of the bar is simulated by applying prescribed displacements at the bar ends.

Computed load-displacement curves are shown in Figure 8.6. From Figure 8.6a it is observed that four different meshes give exactly the same curve. For the second series of calculations only the very coarse mesh produces deviating results, as can be seen from Figure 8.6b. Hence an excellent degree of mesh-independence is found. On comparing Figures 8.6a and 6b, it is also observed that both sets of α and l give virtually identical results, as expected from the analytical solution. Except for the coarsest mesh in Figure 8.6b, all calculations show a softening slope $\Delta\sigma/\Delta u$ of about $93 \cdot 10^3$ kPa/mm, as follows from the analytical solution.

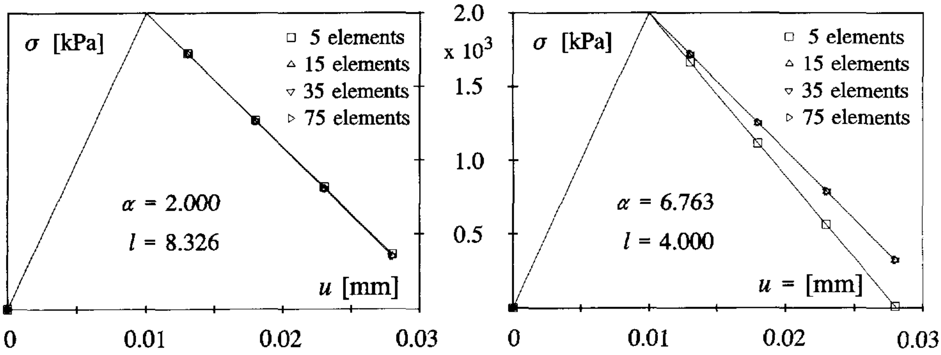

Figure 8.6 Stress-displacement curves of softening bar for different numbers of elements
a. Relatively small α-value b. Relatively large α-value

Computed distributions of plastic strain increments are shown in Figure 8.7. These data demonstrate again mesh-independence. Very pronounced strain localizations are observed and the lengths of these necks can simply be measured. For the computations with $\alpha = 2.000$, a length of about 25 mm was measured (Figure 8.7a) and a length of about 29 mm is found when applying a large value of $\alpha = 6.763$ (Figure 8.7b). The last one approaches the analytical solution of $L = 31.42$ mm. The latter is in line with the argument in Section 8.5, that larger α-values will give closer approximations of the analytical solution.

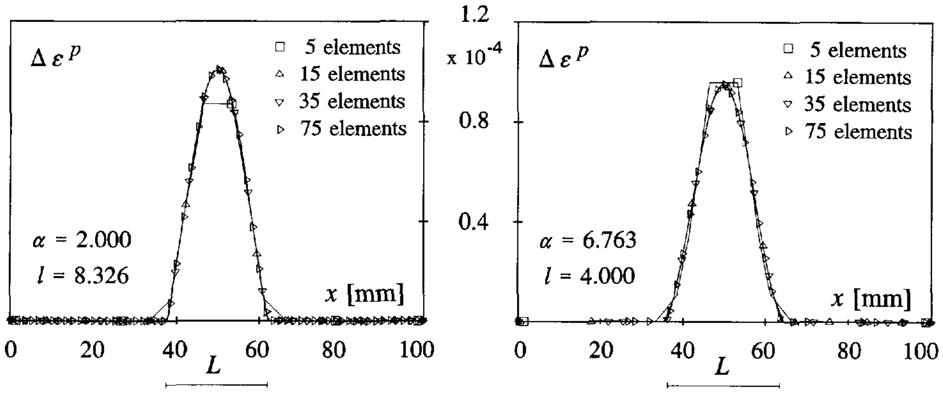

Figure 8.7 Plastic strain increments of softening bar for different numbers of elements
a. Relatively small α-value b. Relatively large α-value

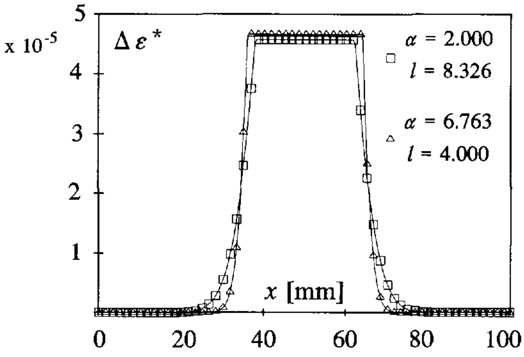

Figure 8.8 Distribution of non-local strain increment (75 elements)

Figure 8.8 shows distributions of the non-local strain measure ε^*. Here the analytical solution indicates a block function. The best approximation of this block function is again obtained for the higher value of the factor α, as expected from the discussion in Section 8.5.

9 IMPLEMENTATION OF REGULARIZATION TECHNIQUE

In this chapter the modified non-local regularization method, as described in the previous chapter, is extended to general three-dimensional applications. It is shown that the method overcomes the problems of mesh-dependency and poor convergence, as indicated in Chapter 7. Moreover, a practical solution is given to avoid the use of very small elements, as needed for a realistic modelling of localization zones.

9.1 A Drucker-Prager non-local softening model

The Drucker-Prager softening model, as described in Section 7.2, is extended with the non-local method of the previous chapter. To this end the softening rule, as given by Equation 7.3, is changed to obtain:

$$\dot{c} = h' \, \dot{\varepsilon}_v^{p\,*} \tag{9.1}$$

where

$$\dot{\varepsilon}_v^{p\,*}(x_n) = (1-\alpha)\, \dot{\varepsilon}_v^p(x_n) + \frac{\alpha}{A} \int\!\!\int\!\!\int w(x_n')\, \dot{\varepsilon}_v^p(x_n + x_n')\, dx_1'\, dx_2'\, dx_3' \tag{9.2}$$

$$A = \int\!\!\int\!\!\int w(x_n')\, dx_1'\, dx_2'\, dx_3' \tag{9.3}$$

x_n' is a local coordinate with $n = 1, 2$ or 3 and w denotes the weighting function, in which the internal length parameter l is included.

The difference between Equation 9.1 and the similar Equation 7.3 is the volumetric plastic strain, which is non-local in the current formulation. Elaboration of the full non-local stress-strain model using the softening rule 9.1 will result in an integro-differential equation, as mentioned by De Borst & Mühlhaus (1991). This problem can be avoided by using suitable approximations of the non-local strain rate 9.2. Now, a later approximation is anticipated by rewriting Equation 9.2 in the form:

$$\dot{\varepsilon}_v^{p\,*} = \dot{\varepsilon}_v^p + \alpha \left[\frac{1}{A} \int w\, \dot{\varepsilon}_v^p \, dV - \dot{\varepsilon}_v^p \right] \tag{9.4}$$

Apart from a rearrangement of terms, a shorter notation is introduced. In this form, the non-local formulation resembles the gradient formulation as expressed in Equation 8.21. The term in brackets can be well compared with the second-order gradient in Equation 8.21. It is known from gradient theory that the second-order gradient term is negative at the point under consideration, whereas it is positive at a distance of the order of the internal length from the point considered. This effect induces a redistribution of plastic strains. The term in brackets in Equation 9.4 has a similar influence and the factor α can be regarded as an amplification factor.

In elastoplastic behaviour, the plastic strains usually dominate the elastic strains, so that the plastic strains can be approximated by the total strains. On applying this approximation to the volumetric plastic strain rates in brackets in Equation 9.4, the non-local volumetric plastic strain rate $\dot{\varepsilon}_v^{p\,*}$ can be approximated by:

$$\dot{\varepsilon}_v^{p\,*} \approx \dot{\varepsilon}_v^p + \alpha \left[\frac{1}{A} \int w \, \dot{\varepsilon}_v \, dV - \dot{\varepsilon}_v \right] \qquad (9.5)$$

Note that in the case of a uniformly distributed elastic volumetric strain field, the elastic components are equal, as in Equation 8.29, and cancel each other out. Under these circumstances the above Equation 9.5 is exact. However, such a situation rarely occurs in practical applications, so that Equation 9.5 should be regarded as an approximation.

Elaboration of the elastoplastic stress-strain relation using the above approximation of the non-local volumetric plastic strain rate in the cohesion softening rule, leads to a regular expression which is formulated as:

$$\underline{\dot{\sigma}} = \left[\underline{\underline{D}}^e - \frac{1}{d+h} \, \underline{a} \, \underline{b}^T \right] \underline{\dot{\varepsilon}} - \frac{\alpha \, h'}{d+h} \, \underline{a} \, \frac{\partial f}{\partial c} \left[\frac{1}{A} \int w \, \dot{\varepsilon}_v \, dV - \dot{\varepsilon}_v \right] \qquad (9.6)$$

at least, when plasticity occurs according to the definition in Equation 3.6b.

The vectors $\underline{a}$ and $\underline{b}^T$ were defined earlier in Equation 3.11 and the softening modulus h was already defined in Equation 7.6.

9.2 Numerical integration and implementation of the non-local model

The above stress-strain relationship can simply be integrated using the implicit integration scheme of Section 5.3. Apart from the calculation of the trial stresses $\underline{\sigma}^{tr}$ as formulated in Equation 5.17 (second part), an auxiliary cohesion c^{tr} must be calculated according to:

$$c^{tr} = c^{i-1} + \alpha \, h' \left[\frac{1}{A} \int w \, \Delta\varepsilon_v \, dV - \Delta\varepsilon_v \right] \tag{9.7}$$

Using this value, the new stress state can be explicitly formulated as:

$$\underline{\sigma}^{i} = \underline{\sigma}^{tr} - \frac{\left\langle f(\underline{\sigma}^{tr}, c^{tr}) \right\rangle}{d + h} \, \underline{\underline{D}}^{e} \left[\frac{\partial g}{\partial \underline{\sigma}} \right]^{i} \tag{9.8}$$

The second term is only taken into account if the value of the yield function, based on $\underline{\sigma}^{tr}$ and c^{tr}, is larger than zero, as implied by the McCauley brackets $\langle \, \rangle$. The above equation is similar to Equation 5.21 for local plasticity, except that the yield function is evaluated with the auxiliary cohesion.

In the case of plastic behaviour, i.e. when $f(\underline{\sigma}^{tr}, c^{tr}) > 0$, the cohesion is updated according to:

$$c^{i} = c^{i-1} + \Delta\lambda \, h' \left[\frac{\partial g}{\partial p} \right]^{i} + \alpha \, h' \left[\frac{1}{A} \int w \, \Delta\varepsilon_v \, dV - \Delta\varepsilon_v \right] \tag{9.9}$$

where $\Delta\lambda$ is defined as:

$$\Delta\lambda = \frac{f(\underline{\sigma}^{tr}, c^{tr})}{d + h} \tag{9.10}$$

Considering the numerical implementation of the model, only minor changes are required compared with the local Drucker-Prager model. Note that the new stress state can be calculated in a local process without iteration, provided that the non-local contribution $\int w \, \Delta\varepsilon_v \, dV \, / \, A$, as required for the cohesion softening, is known for each stress point. This local process is summarized in the scheme on the next page.

```
$\underline{\sigma}^{tr} = \underline{\sigma}^{i-1} + \underline{\underline{D}}^{e} \Delta \underline{\varepsilon}$        (Equation 5.17)
calculate $c^{tr}$        (Equation 9.7)
calculate $f(\underline{\sigma}^{tr}, c^{tr})$        (Equation 3.3)
if $f > 0$ then
    calculate $d$ and $h$        (Equation 3.9 / 7.6)
    $\Delta\lambda = \frac{f(\underline{\sigma}^{tr}, c^{tr})}{d + h}$        (Equation 9.10)
    $\underline{\sigma}^{i} = \underline{\sigma}^{tr} - \Delta\lambda \, \underline{\underline{D}}^{e} \left[ \frac{\partial g}{\partial \underline{\sigma}} \right]^{i}$        (Equation 9.8)
    calculate $c^{i}$        (Equation 9.9)
end of if
```

The non-local contribution $\int w \, \Delta\varepsilon_v \, dV \, / \, A$ is calculated from the strain increments in the integration points. According to the finite element method, the strain increments follow from the displacement increments in the nodes, as formulated in Equation 5.10. The integral as mentioned above is evaluated for all integration points:

$$\frac{1}{A} \int w \, \Delta\varepsilon_v \, dV = \frac{\sum_{i=1}^{n} V_i \, w_i \, \Delta\varepsilon_{v_i}}{\sum_{i=1}^{n} V_i \, w_i} \tag{9.11}$$

where n is the number of integration points, V_i is the representative volume of integration point i and w_i is the value of the weighting function according to Equation 8.5. The latter depends on the internal length l as well as the distance r between integration point i and the integration point under consideration.

In fact, the current non-local model is easy to implement in existing finite element programs. Moreover, the above procedure can be extended to more complex softening models such as the Advanced Cam-Clay model of Section 7.1.

9.3 Shear-banding in purely cohesive material

In addition to the Drucker-Prager non-local softening model, as described in the previous section, a non-local Von Mises softening model can be formulated. A detailed model description will be omitted, but the Von Mises model is used in some calculations to show the effectiveness of the modified non-local method for softening problems. This is done by means of a recalculation of the biaxial test problem of Section 7.4.1. As the problem is fully documented in Section 7.4.1, attention is focused here on the non-local quantities.

In Chapter 8 an expression was derived for a one-dimensional situation in which the width of the localization zone L is related to the internal length l and the amplification factor α. It is assumed that this expression is also valid for the shear-band thickness in two-dimensional applications, such as the current biaxial test problem. A realistic shear-band will usually be very small and requires a very fine grid in a numerical analysis. However, in order to prove the effectiveness of the current regularization method, it is not necessary to model a realistic shear-band thickness. Hence, a much wider band can be accepted here.

In the current example, the internal length l is taken such that the positive influence of the non-local method is guaranteed for the coarsest mesh being used. The amplification factor α can, in principle, be selected arbitrarily, provided that it is larger than 1.0. In the current example, it is chosen for an amplification factor $\alpha = 2.0$ and an internal length $l = 0.02$ m. With these values Equation 8.18 would suggest a shear-band thickness of 0.075 m.

Calculations were performed for the four different element meshes as shown in Figure 7.3. In contrast to the calculations with local softening plasticity, the current calculations run smoothly, i.e. fast convergence of the iteration process and barely changing (automatic) step sizes. Figure 9.1 presents the Force-Displacement curves of the biaxial test problem. The curves match very well. There is no significant mesh dependence and the softening branch is almost a straight line. It is remarkable that the softening branch tends to increase after quite some softening has occurred. This may indicate a slightly changing localization zone.

Figure 9.2 shows the contour lines of displacement increments as obtained from the softening branch for a force of about 1.4 kN. The numerical results, as shown in Figure 9.2, indicate a more-or-less homogeneous shear-band thickness of about 0.06 m, independent of the element size and the orientation of elements. Indeed, the observed thickness is smaller than the theoretical value, but this is in line with the one-dimensional results for $\alpha = 2.0$, as discussed in Section 8.8. The orientation of the shear-band, i.e. the inclination angle θ, is about 45 degrees, as expected from theory (e.g. Vermeer, 1990). As softening proceeds, the orientation θ tends to decrease a little, which may explain the slightly increasing softening branch as mentioned before. This type of behaviour is not observed for real soil behaviour.

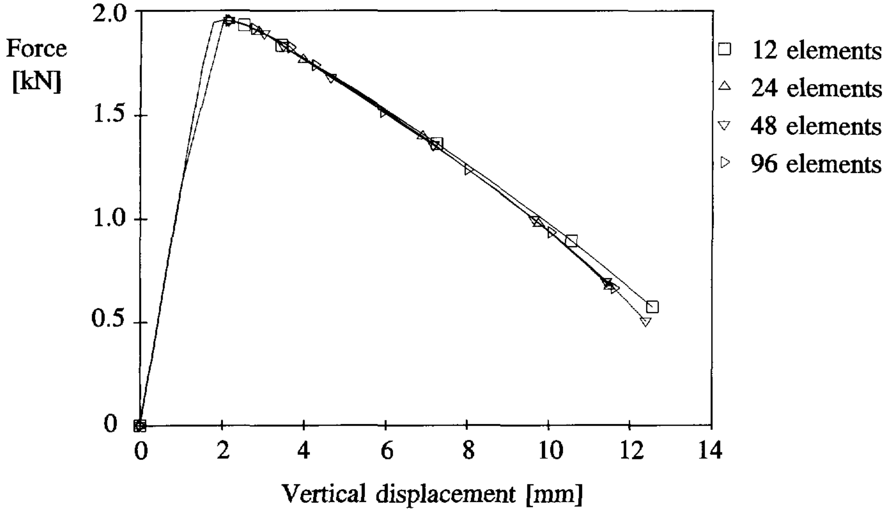

Figure 9.1 Force-Displacement curves from biaxial test problem with non-local model

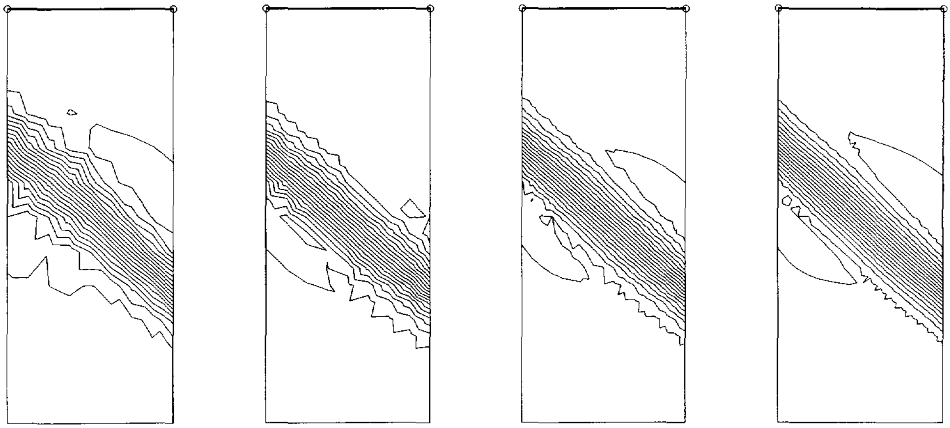

Figure 9.2 Contour lines of displacement increments for biaxial test in softening branch
a. 12 elements b. 24 elements c. 48 elements d. 96 elements

More details on the shear-band orientation will be given in the next section, where frictional material is considered. The current example shows that the non-local model gives mesh-independent results and good convergence of iterative procedures. On using a coarse mesh of only 12 triangular elements, the solution is already fairly accurate, because the results from the 96-element mesh are not so different. It should be noted here that high-order 15-noded elements were used with full 12-point Gaussian integration. The size of the elements, as used in the 12-element mesh, is of the order of the shear-band thickness. On using larger element sizes, say twice the shear-band thickness, the influence of the non-local term is too low to provide an effective regularization. This could be improved slightly by using 16-point or even 25-point Gaussian integration, but, as a rule, the lower limit for the element size is advised to be at least the shear-band width. Using lower-order elements gives an even stronger requirement for the element size with respect to the shear-band thickness.

From a convergence point of view, the amplification factor $\alpha = 2.0$ seems to be well-suited for two-dimensional applications, although the shear-band thickness is smaller than Equation 8.18 suggests. Without presenting any figures, it can be mentioned here that even better results can be obtained by using a larger amplification factor. This was observed in a calculation in which $\alpha = 5.0$ was used in combination with a smaller internal length $l = 0.011$ m, such that the resulting shear-band thickness is similar, at least according to Equation 8.18. Indeed, the softening branch in the resulting Force-Displacement curve shows an even more regular step-size distribution and approximates a straight line well. However, the observed shear-band thickness is still too small compared with the theoretical value resulting from Equation 8.18.

9.4 Shear-banding in rock-like material

Considering rock-like materials, one may observe high friction angles up to 40 degrees (Vermeer & De Borst, 1984) together with a relatively high cohesion for the intact rock. In biaxial tests on rock-like materials, thin shear-bands are observed and the collapse modes very closely resemble those of soil. An extensive study on shear-banding in soft rock was recently published by Tillard (1992). Within a shear-band, there is an increase of volume, which breaks down the cohesive ties. The material friction, however, remains more-or-less the same. The Drucker-Prager non-local softening model, as described in Section 9.1, can serve as a first approximation for the behaviour of rock-like material.

Again, the biaxial test problem, as described in Section 7.4.1, is calculated. In the current calculations the Drucker-Prager non-local softening model of Section 9.1 is used. The model parameters, as listed in Table 9.1, are chosen arbitrarily, but not unrealistically considering a rock-like material. In order to avoid the use of very small elements, the internal length parameter is taken much higher than the value that is required to obtain a realistic shear-band thickness. The amplification factor α is taken as 2.0.

Table 9.1 Model parameters for biaxial test of rock-like material

Drucker-Prager softening			
Shear modulus	G	$= 1{\cdot}10^6$ kPa	
Poisson's ratio	ν	$= 0.3$	
Initial cohesion	c_0	$=$ 20 kPa	
Friction angle	φ	$= 40°$	$(\alpha = 1.08)$
Dilation angle	ψ	$= 10°$	$(\beta = 0.30)$
Softening modulus	h	$= 2{\cdot}10^4$ kPa	

Figure 9.3 shows the Force-Displacement curve of the biaxial test. The curves match reasonably well. The 48-element mesh shows a minor deviation from the other curves, but the inclination is about equal. This mesh also requires by far the most calculation steps. As the results of the 96-element mesh are again in line with the coarser meshes, the deviations as observed in the 48-element mesh should be considered as a bad coincidence.

Figure 9.4 shows the contour lines of the displacement increments as obtained from the softening branch for a force of about 5.2 kN. The observed shear-band thickness is equal to the shear-band thickness of about 0.06 m as observed in the previous example (Section 9.3). The orientation θ, however, is somewhat larger and corresponds well to the formula given by Roscoe (1970): $\theta = 45° + \psi / 2$.

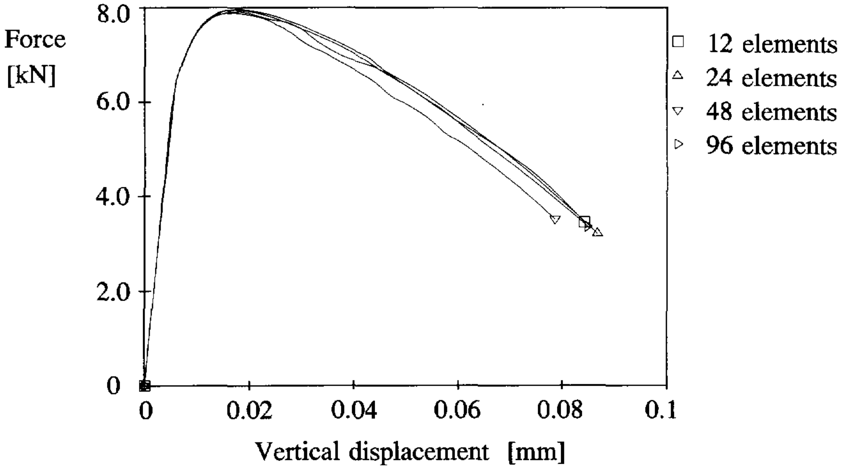

Figure 9.3 Force-displacement curves from biaxial test on rock-like material

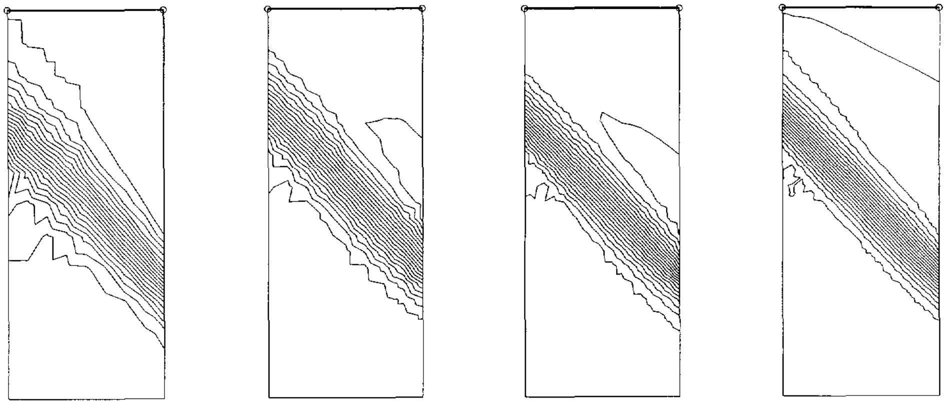

Figure 9.4 Contour lines of displacement increments for biaxial test on rock-like material
a. 12 elements b. 24 elements c. 48 elements d. 96 elements

Calculations for highly frictional materials tend to be more cumbersome than for materials with a low friction angle (De Borst & Vermeer, 1984). For the present non-local model the situation would seem better, because no real difficulties were encountered here when using $\varphi = 40°$. However, as yet, experience is restricted to biaxial tests and it cannot be concluded that the current model can handle high friction angles without difficulties in any type of problem. On examining Figure 9.3 in detail, it can be seen that the Force-Displacement curves are not as smooth as those presented in Figure 9.1 for friction less material, but without any doubt, results are fully mesh-independent. The results can further be improved by using a larger amplification factor together with a smaller internal length, as discussed in the previous section.

For a material with a friction angle of 40 degrees, a comparison was made of the shear-band orientation for a dilation angle of 10° and 25° respectively. Figure 9.5 presents the incremental displacement fields of both cases. The orientation θ is significantly larger when using the larger dilation angle, and corresponds again to the Roscoe solution (57.5°). Moreover, it was found that on increasing the friction angle without changing the dilation angle, the orientation remains the same. From this observation it can be concluded that for the current Drucker-Prager softening model, the shear-band orientation is determined by the dilation angle according to the Roscoe solution, $\theta = 45° + \psi / 2$. Vermeer (1990) has indicated that the Roscoe solution applies generally to coarse sands, where the influence of stress discontinuities is negligible. In the current numerical model there are no stress discontinuities, except for small residual stresses. From that point of view it is logical and reasonable that the Roscoe solution is found in the numerical model.

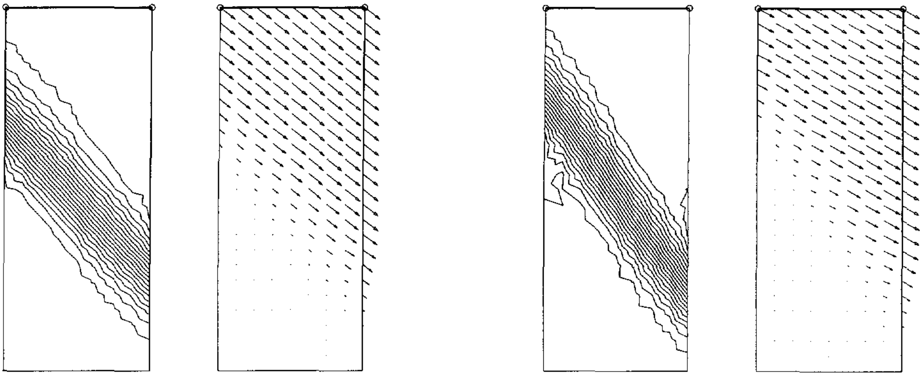

Figure 9.5 Comparison of shear-band orientation for $\varphi = 40°$ and different dilation angles

a. $\psi = 10°$ b. $\psi = 25°$

9.5 Softening scaling to improve practical applicability

The modified non-local method is, as any other regularization technique, only effective if the grid size is in any direction at most the size of the shear-band thickness. In the numerical model, the shear-band thickness is related with the internal length parameter, whereas from a physical point of view, the shear-band thickness is related with the average grain size, at least for granular materials (Mühlhaus & Vardoulakis, 1987). For geomaterials, the real shear-band thickness is generally very small with respect to the dimension of the geometry that is modelled in a numerical analysis. In principle, shear-bands can occur everywhere in the geometry. This leads to the conclusion that realistic calculations of most geotechnical problems can only be made if thousands of extremely small elements are used, which will make calculations very expensive and time consuming. Therefore, a more practical solution is desired.

A step in this direction is made by the use of adaptive remeshing techniques, as developed by Löhner et al. (1986), Zienkiewicz & Zhu (1987), and successfully applied for shear-band problems by Pastor et al. (1991). In this method a finite element mesh is continuously remeshed according to a specific refinement functional. This functional is defined such that, on remeshing, small elements are formed in zones of relatively large deformations and larger elements are formed in zones of relatively small deformations. Note that the use of adaptive remeshing does not abolish the need for an effective regularization technique. Indeed, with adaptive remeshing, the total number of elements is largely reduced compared with an extremely fine mesh throughout the whole geometry, but still a lot of elements are required to model a shear-band accurately. Moreover, the remeshing procedure is quite complicated and requires a lot of "administration". The latter point is particularly true when considering practical geotechnical applications, where soil properties tend to vary from one layer to another. Nevertheless, adaptive remeshing is a promising method which may be developed to become a powerful tool for practical geotechnical applications.

In this thesis a very simple method is proposed to predict the appropriate softening behaviour for practical applications, using relatively large element sizes. The method is called *softening scaling* and is based on the technique as proposed by Pietruszczak & Mroz (1981). Instead of striving for modelling the real shear-band thickness, a much larger non-physical shear-band thickness is adopted, which is the minimum shear-band thickness that can accurately be resolved by the given finite element mesh. Therefore an auxiliary internal length parameter l_{mesh} is introduced, defined as:

$$l_{mesh} = \mu \sqrt{\min(A_i)} \qquad \text{(for } i=1 \text{ to } n\text{)} \qquad \text{(2-D applications)} \qquad (9.12a)$$

$$l_{mesh} = \mu \sqrt[3]{\min(V_i)} \qquad \text{(for } i=1 \text{ to } n\text{)} \qquad \text{(3-D applications)} \qquad (9.12b)$$

Here A_i and V_i are, respectively, the area and the volume that are covered by element i and n is the number of elements. The factor μ, which is used to optimize the non-physical shear-band thickness, is influenced by numerical aspects such as the type of elements being used and the number of integration points. For the modified non-local method, μ is also influenced by the amplification factor α. Without giving further details, a proper value for μ is suggested here for the modified non-local method using 15-noded elements:

$$\mu = \sqrt{\ln(\alpha) - \ln(\alpha - 1)} \;/\; \pi \qquad (\mu = 0.15 \text{ for } \alpha = 5) \qquad (9.13)$$

In addition, a softening scaling factor is introduced, defined as

$$\eta = \frac{l_{mesh}}{l} \qquad (9.14)$$

where l is the physical internal length, i.e. the value that will give the real shear-band thickness. The global softening behaviour depends linearly on the shear-band thickness and on the softening modulus. The softening increases with decreasing shear-band thickness and with increasing softening modulus. Hence, on using the auxiliary internal length parameter instead of a realistic internal length and simultaneously multiplying the softening modulus by the softening scaling factor, one obtains, in principle, a similar softening behaviour as when using realistic values for l and h.

Such a recalculation of parameters can automatically be done in a finite element program. In combination with the previously described non-local method, a robust and objective calculation procedure is obtained for softening plasticity. In this way a user can concentrate on the input of realistic parameters without worrying about numerical difficulties. However, it should be realized that the observed shear-band thickness is not realistic.

Finite element calculations tend to become more accurate when using a finer mesh. This general principle is lost when using softening plasticity without regularization, as shown in Chapter 7. On using the modified non-local regularization method with softening scaling, as described in this thesis, this general principle of the finite element method is retained. It should be noted that the use of softening scaling is not purely associated with non-local regularization, as it can be used in combination with other effective regularization methods as well.

9.6 Non-local softening and scaling in slope stability problem

In this final application it will be shown that similar softening behaviour can be obtained for different meshes when using non-local softening together with the scaling method as described in the previous section. Therefore a slope stability problem, similar to the one in Section 7.4.2, is calculated using a mesh of 18 elements and 72 elements. For the current application, model parameters are chosen to be different from Section 7.4.2. Considering sandy clay, one may observe a realistic shear-band thickness of the order of a few millimeters, say 5 mm. An amplification factor of $\alpha = 5.0$ was chosen. An appropriate internal length would be $7 \cdot 10^{-4}$ m. The real softening modulus is arbitrarily chosen as 1 kPa.

Table 9.2 Model parameters for slope stability problem

Drucker-Prager softening				
Dry weight	γ	=	16 kN/m^3	
Shear modulus	G	=	1000 kPa	
Poisson's ratio	ν	=	0.3	
Initial cohesion	c_0	=	10 kPa	
Friction angle	φ	=	35 °	($\alpha = 0.98$)
Dilation angle	ψ	=	5 °	($\beta = 0.15$)
Softening modulus	h	=	1 kPa	

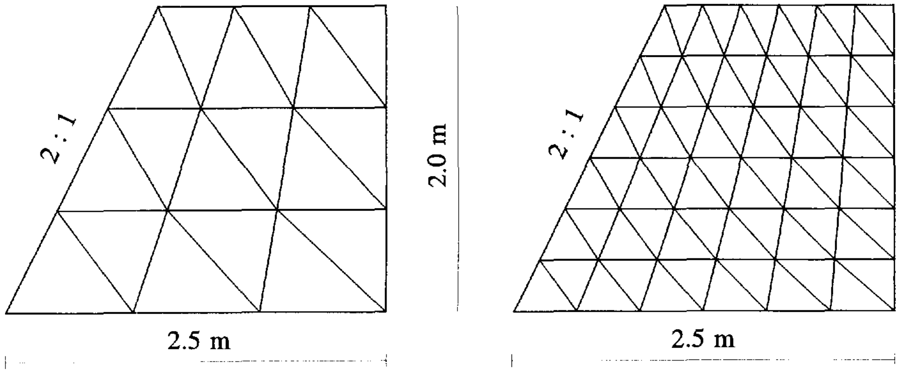

Figure 9.6 Finite element meshes in slope stability analysis of softening material
a. 18-element mesh b. 72-element mesh

Considering the 18-element mesh, the minimum element area is 0.20 m^2. Using Equation 9.12a with help of Equation 9.13 gives an auxiliary internal length l_{mesh} = 0.07 m. This gives a softening scaling factor of 100. Hence, the applied softening modulus in the numerical model for the 18-element mesh is 100 kPa. In the 72-element mesh, the minimum element area is 0.05 m^2. The resulting auxiliary internal length and the softening scaling factor are half the values as obtained for the 18-element mesh. The shear-band thickness that is expected from Equation 8.18 is 0.47 m for the 18-element mesh and 0.93 m for the 72-element mesh.

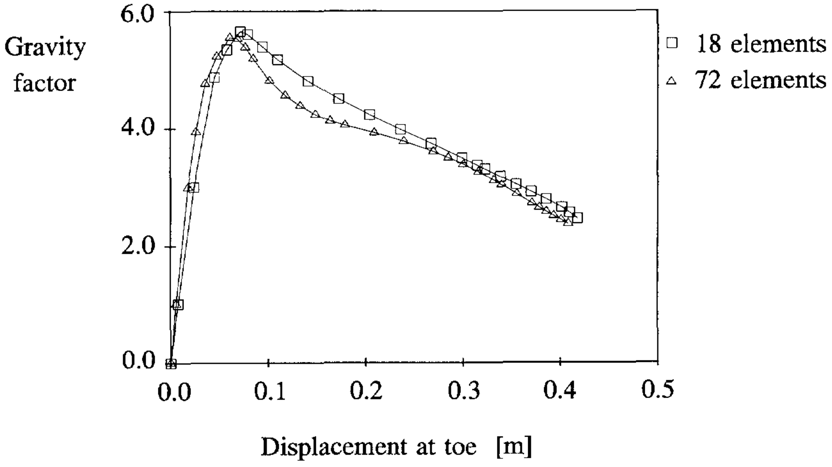

Figure 9.7 Force-Displacement curve for slope stability problem

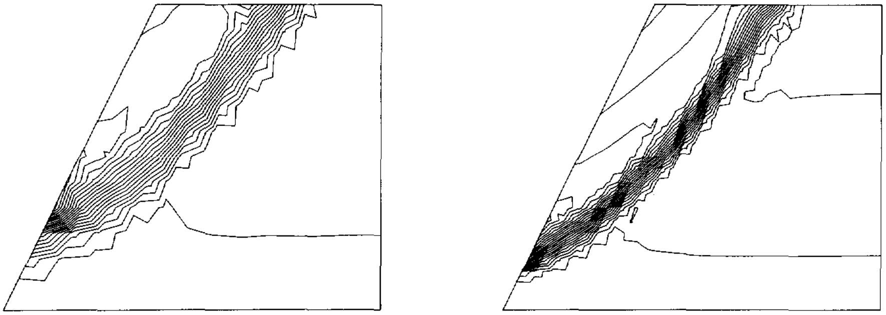

Figure 9.8 Contour lines of displacement increments indicating a shear-band
a. 18-element mesh b. 72-element mesh

Figure 9.7 presents the Force-Displacement curves of both calculations. Although the curves do not completely coincide, the results are fully acceptable from a practical point-of-view. In contrast with the results as presented in Section 7.4.2, the current results give a mesh-independent peak load. This peak load is higher than in Section 7.4.2, because a larger friction angle was adopted here.

Figure 9.8 shows a difference in the shear-band thickness of a factor 2. This is induced by the difference in the auxiliary internal length parameter. The shear-band thicknesses, as measured from the plots, agree well with the theoretical values. The location and orientation of the shear-band in both calculations is similar.

Although it can be concluded that the method of softening scaling gives acceptable results from a practical viewpoint, care should be taken with coarse meshes. In such a case, a wide shear-band occurs, which may be highly influenced by geometrical effects or boundary conditions. As a result, no full objectivity with respect to the finite element discretization is obtained. For relatively fine meshes, the modelled shear-band thickness is small, and geometrical effects will hardly influence the results.

10 CONCLUSIONS AND RECOMMENDATIONS

The use of a simple power law to formulate the elastic stiffness modulus as a function of the stress level is incorrect from a viewpoint of energy. A model based on a (complementary) strain-energy function does not have this anomaly, but the applicability of such a model is limited. The complementary strain-energy function of Vermeer (1980) is applicable for modelling the (elastic) behaviour of sand, but it cannot be generalized to account for a linear relationship between stiffnesses and stress level, as needed for Cam-Clay type models. Neither is the complementary strain-energy function of Molenkamp (1988), in its original form, suitable for Cam-Clay type models. Therefore an extension of this model is proposed such that stiffnesses proportional with the stress level can be accounted for.

For elastoplastic models, in which only one yield function contributes to plastic straining, the elastoplastic material matrix can be obtained by elaboration of the consistency condition. For models in which more than one yield function contributes to plasticity, the proper elastoplastic material matrix can be obtained by repeating the single yield function procedure for all active yield functions successively. This new method is simpler than the existing method in which a set of equations must be solved before the matrix can be formed.

For practical applications, the Mohr-Coulomb model is a widely accepted model to simulate the behaviour of geomaterials. Generally, this model describes failure more accurately than the Drucker-Prager model, but for particular conditions the Drucker-Prager model can be tuned such that it predicts a similar failure load as the Mohr-Coulomb model. In this respect a formulation is elaborated for the Drucker-Prager parameters for the case of plane strain, in which the effect of dilatancy is included. In order to further improve the practical applicability of the Mohr-Coulomb model, it is proposed here to extend this model with a stress-dependent stiffness modulus, a tension cut-off and a dilatancy cut-off. The extended model is named the Advanced Mohr-Coulomb model.

The Modified Cam-Clay model does not correctly predict the K_0-path in one-dimensional compression. This anomaly is improved in the Plaxis Cap model. In the latter model, both failure and K_0-path can be tuned independently with different model parameters. A further improvement can be obtained by formulating a Mohr-Coulomb like failure surface for the Plaxis Cap model instead of the Drucker-Prager type failure surface. The latter extension is not considered in this study and is a subject for further development. An important conclusion from the use of (cap) hardening models is that the observed stiffness behaviour does not only depend on the stress level but also on the stress path.

For the stress integration of the Plaxis Cap model three different situations are discussed in detail. For elastic behaviour an exact integration scheme is proposed. It is recommended that an initial strain method for loading and an initial stress method for unloading be used. For cap yielding, a robust implicit integration scheme is proposed. For the (numerical) integration of the hardening rule, a midpoint rule performs the best, as far as speed and accuracy are concerned. Because of non-linearity, a local iteration process is inevitable. For the yield vertex, also a robust implicit integration scheme is proposed. By again using numerical integration of the hardening rule, a local iteration process can be avoided.

Concerning global equilibrium iterations, it is known that the use of a consistent tangent stiffness matrix drastically decreases the number of iterations required for a certain tolerated error. However, the range of calculation steps that properly lead to convergence was found to be much smaller than when using the elastic stiffness matrix. As a result, the step size must be taken much smaller in order to avoid divergence. In general, the total time needed for an average two-dimensional failure analysis was found to be longer than when using an elastic stiffness matrix with acceleration procedures (Vermeer & Van Langen, 1989). Hence, for practical applications it is recommended that an elastic stiffness matrix be used.

From the practical applications it can be concluded that the implementation of the Plaxis Cap model, as described in this thesis, is indeed robust and performs well. Using hardening plasticity does not always produce better results than using perfect plasticity. For some practical applications similar results can be obtained for both categories of geomaterial models. Hardening plasticity is in favour when successive compression and distortion is expected or when stress points are successively subject to compressive and deviatoric stress paths. Moreover, in order to predict lateral deformations correctly in quasi vertical loading problems, the use of a hardening model is required.

Softening behaviour of overconsolidated clay as well as rock-like material can be described as a first approximation with a Drucker-Prager linear softening model. This model can be extended to the highly non-linear Advanced Cam-Clay model, as described by Atkinson & Bransby (1978). A first approach to a mathematical formulation of this model is given in this thesis, but a full formulation and numerical implementation is a subject of further research. Numerical analyses with local softening plasticity do not only cause mesh-dependency, as mentioned in several publications, but poor convergence of equilibrium iterations as well. For the numerical analysis of softening behaviour, the use of a regularization method is definitely required.

The non-local theory is a regularization method with a clear physical background. Existing non-local models, in which the softening parameter is treated as a pure non-local quantity, distributed according to the error function, do not give a proper regularization in one-dimensional applications. The modified non-local method, as introduced in this thesis, in which a different formulation of the softening parameter is utilized, does give a proper regularization. For the one-dimensional case of necking in a tension bar, an exact analytical solution exists which is directly based on the non-local formulation.

The modified non-local method can easily be applied to the Drucker-Prager softening model and implemented in a general three-dimensional finite element program. The method is robust, gives mesh-independent results and provides proper convergence of equilibrium iterations. The amplification factor α, as used in the definition of the non-local softening parameter, must be larger than 1. Based on current experience, a value of 5.0 is recommended, but a more detailed investigation is required. This is a topic for further research. Shear-band analyses of biaxial test problems indicate that the current non-local model gives a shear-band orientation according to Roscoe's solution. The amount of softening linearly depends on the shear-band thickness. For a good performance of the non-local method, the (15-noded) element size in each direction must be smaller than the shear-band thickness. In order to avoid the use of many extremely small elements in practical applications, one could use the method of softening scaling, as proposed in this thesis, based on earlier work of Pietruszczak & Mroz (1981). In this method, the softening behaviour is modelled sufficiently accurately, but the shear-band thickness is not realistic.

REFERENCES

Adachi T., Oka F. (1982), Constitutive Equations for Normally Consolidated Clay based on Elasto-Viscoplasticity. Soils & Foundations 22, No. 4, pp. 57-70.

Aifantis E.C. (1984), Microscopic Processes and Macroscopic Response. In: Mechanics of Engineering Materials (eds. Desai, Gallagher). pp. 1-22.

Atkinson J.H., Bransby P.L. (1978), The Mechanics of Soils. McGraw-Hill, London.

Bazant Z.P. (1976), Instability, Ductility, and Size Effect in Strain-Softening Concrete. ASCE J. Eng. Mech., Vol. 102, pp. 331-334.

Bazant Z.P., Belytschko T.B., Chang T.P. (1984), Continuum Theory for Strain-Softening. ASCE J. Eng. Mech., Vol. 110, No. 12, pp. 1666-1692.

Bazant Z.P., Lin F.B., Pijaudier-Cabot G. (1987) Yield Limit Degradation; Nonlocal Continuum Model with Local Strain. In: Proc. Int. Conf. Computational Plasticity, Barcelona (eds. Owen, Hinton, Onate), pp. 1757-1780.

Bazant Z.P., Zubelewicz A. (1988), Strain Softening Bar and Beam: Exact Nonlocal Solution. Int. J. Solids & Struct., Vol. 24, No. 7, pp. 659-673.

Borja R.I., Lee S.R. (1990), Cam-Clay Plasticity, Part I: Implicit Integration of Elasto-Plastic Constitutive Relations. Comp. Meth. Appl. Mech. Eng., No. 78, pp. 49-72.

Boulon M., Foray P. (1986), Physical and Numerical Simulation of Lateral Shaft Friction along Offshore Piles in Sand. In: Proc. III Int. Conf. on Numerical Methods in Offshore Piling. Nantes, France, pp. 127-147.

Brakel J., Coppens M., Maagdenberg A.C., Risseeuw P. (1982), Stability of Slopes Constructed with Polyester Reinforcing Fabric, Test Section at Almere - Holland. In: Proc. II Int. Conf. on Geotextiles (eds. J.P. Giroud, S.M. Warner), Las Vegas, USA, pp. 727-732.

Brinkgreve R.B.J., Vermeer P.A. (1992) On the Use of Cam-Clay Models. In: Proc. IV Int. Symposium on Numerical Models in Geomechanics (eds. G.N. Pande, S. Pietruszczak). Balkema, Rotterdam, Vol. 2, pp. 557-565.

Brinkgreve R.B.J., Vermeer P.A., Vos E. (1994), Constitutive Aspects of an Embankment Widening Project. In: Advances in Understanding and Modelling the Mechanical Behaviour of Peat (eds. E. den Haan, R. Termaat, T.B. Edil). Balkema, Rotterdam, pp. 143-158.

Burland J.B. (1965), The Yielding and Dilation of Clay. (Correspondence). Géotechnique, Vol. 15, pp. 211-214.

Burland J.B. (1967), Deformation of Soft Clay. Dissertation. Cambridge University.

Chan D.H., Morgenstern N.R. (1989), An Effective Stress Approach to Undrained Analysis. In: Proc. III Conf. on Numerical Models in Geomechanics (eds. S. Pietruszczak, G.N. Pande). Elsevier Science Publishers, London, pp. 740-750.

Charlier R. (1992), Modelling of Shear-Band Localisation Using Interface Elements. In: Proc. IV Int. Symposium on Numerical Models in Geomechanics. (eds. G.N. Pande, S. Pietruszczak). Balkema, Rotterdam, pp. 357-365.

Chen W.-F. (1975), Limit Analysis and Soil Plasticity. Elsevier, Amsterdam.

Christoffersen J., Mehrabadi M.M., Nemat-Nasser S. (1981), A Micromechanical Description of Granular Material Behavior. J. Appl. Mechanics, Vol. 48, No. 2, pp. 339-344.

Cosserat E., Cosserat F. (1909), Théorie des Corps Deformables. Herman et Fils, Paris.

Couvreur J.F., Vermaut M. (1992), Toepassing van Numerieke Modellen bij Wegverbreding op Slappe Ondergrond. Delft University of Technology, Geotechnical Laboratory report no. 343.

Crisfield M.A. (1987), Consistent Schemes for Plasticity Computation with the Newton-Raphson Method. In: Proc. Int. Conf. on Computational Plasticity (eds. D.R.J. Owen, E. Hinton, E. Onate). Pineridge Press, Swansea, U.K., pp. 133-159.

De Borst R. (1990), Simulation of Localisation Using Cosserat Theory. In: Proc. II Int. Conf. Computer Aided Analysis and Design of Concrete Structures (eds. N. Bicanic, H.A. Mang). Pineridge Press, Swansea, U.K., pp. 931-944.

De Borst R., Mühlhaus H.B. (1991), Computational Strategies for Gradient Continuum Models with a View to Localisation of Deformation. Proc. IV Int. Conf. on Nonlinear Engineering Computations (eds. N. Bicanic, P. Marovic, D.R.J. Owen, V. Jovic, A. Mihanovic). Pineridge Press, Swansea, U.K., pp. 239-260.

De Borst R., Mühlhaus H.B., Pamin J., Sluys L.J. (1992), Computational Modelling of Localisation of Deformation. Proc. III Int. Conf. Computational Plasticity. (eds. D.R.J. Owen, E. Onate, E. Hinton). Pineridge Press, Swansea, U.K., pp. 483-508.

De Borst R., Vermeer P.A. (1984), Possibilities and Limitations of Finite Elements for Limit Analysis. Géotechnique, Vol. 34, pp. 199-210.

Desrues J. (1984), La localisation de la Déformation dans les Matériaux Granulaires. Dissertation. Institut National Polytechnique de Grenoble.

Deutekom J.R., Dekker J., Janse E. (1992), Proefvak BRICOR - Meetrapprot, Eindrapport. Delft Geotechnics - Dept. of Soil Structures, Report CO-300992/24, part I.

Drucker D.C., Prager W. (1952), Soil Mechanics and Plastic Analysis or Limit Design. Quart. Appl. Math. Vol. 10, No. 2, pp. 157-165.

Duncan J.M., Chang C.-Y. (1970), Nonlinear Analysis of Stress and Strain in Soils. ASCE J. of the Soil Mech. and Found. Div. Vol. 96, pp. 1629-1653.

Eringen A.C. (1972), Nonlocal Polar Elastic Continua. Int. J. Engineering Science, 10, pp. 1-16.

Eringen A.C. (1981), On Non-local Plasticity. Int. J. Engineering Science, 19, pp. 1461-1474.

Fung Y.C. (1965), Foundations of Solid Mechanics, Prentice-Hall, New Jersey, USA.

Goldscheider M. (1984), True Triaxial Tests on Dense Sands. In: Constitutive Relations for Soils (Eds. G. Gudehus, F. Darve, I. Vardoulakis), Balkema, Rotterdam.

Gröbner W., Hofreiter N. (1961), Integraltafel. Erster Teil, Unbestimmte Integrale. Zweiter Teil, Bestimmte Integrale. Springer-Verlag, Wien.

Hadamard J. (1903), Leçons sur la Propagation des Ondes et les Equations de l'Hydrodynamique. Chap. 6, Hermann, Paris.

Hill R. (1950), The Mathematical Theory of Plasticity, Oxford University Press, London, U.K.

Jaky J. (1944), The Coefficient of Earth Pressure at Rest. (in Hungarian). Magyar Mernok es Epitesz Egylet Koslonye, pp. 355-358.

Koiter W.T. (1953), Stress-Strain Relations, Uniqueness and Variational Theorems for Elastic-Plastic Materials with Singular Yield Surface. Quart. Appl. Math. 11, pp. 350-354.

Koiter W.T. (1960), General Theorems for Elastic-Plastic Solids. In: Progress in Solid Mechanics, Vol. 1 (Eds. Sneddon and Hill). North Holland Publishing Co., Amsterdam, pp. 165-221.

Kondner R.L. (1963), Hyperbolic Stres-Strain Response: Cohesive Soils. ASCE J. of the Soil Mech. and Found. Div. Vol. 89, pp. 115-143.

Labanieh S. (1984), Modélisations Non-Linéaires de la Rhéologie des Sables et Applications. Dissertation. Institut National Polytechnique de Grenoble.

Ladd C.C., Foott R., Ishihara K., Schlosser F. (1977), Stress-Deformation and Strength Characteristics. In: Proc. IX Int. Conf. Soil Mechanics and Foundation Engineering, Tokyo, pp. 421-494.

Lade P.V. (1977), Elastoplastic Stress-Strain Theory for Cohesionless Soil with curved Yield Surfaces. Int. J. Solids & Struct., Vol. 13, pp. 1019-1034.

Lasry D., Belytschko T. (1988), Localization Limiters in Transient Problems. Int. J. Solids & Struct., Vol. 24, No. 6, pp. 581-597.

Leroy Y., Nacar A., Needleman A., Ortiz M. (1987), A Finite Element Method for Localization Analysis. In: Advances in Inelastic Analysis, ASME. (eds. S. Nakazwa, K.J. William) Vol. 88, pp. 97-106.

Löhner R., Morgan K., Zienkiewicz O.C. (1986), Adaptive Grid Refinement for the Compressible Euler Equations. In: Accuracy Estimates and Adaptive Refinements in Finite Element Computations (eds. I. Babuska et al.). pp. 281.

Mandel J. (1965), Généralisation de la Théorie de Plasticité de W.T. Koiter. Int. J. Solids & Struct., Vol. 1, pp. 273-295.

McMeeking R.M., Rice J.R. (1975), Finite-Element Formulations for Problems of Large Elastic-Plastic Deformation. Int. J. Solids & Struct., Vol. 11, pp. 601-616.

Mindlin R.D. (1965), Second Gradient of Strain and Surface Tension in Linear Elasticity. Int. J. Solids & Struct., Vol. 1, pp. 417-437.

Molenkamp F. (1988), A Simple Model for Isotropic Non-Linear Elasticity of Frictional Materials. Int. J. Num. Anal. Meth. Geomech., Vol. 12, pp. 467-475.

Molenkamp F. (1992), Application of Non-Linear Elastic Model. Int. J. Num. Anal. Meth. Geomech., Vol. 16, pp. 131-150.

Mühlhaus H.B., (1986), Scherfugenanalyse bei Granularem Material im Rahmen der Cosserat-Theorie. Ingen. Archiv, Vol. 56, pp. 389-399.

Mühlhaus H.B., Aifantis E.C. (1991), A Variational Principle for Gradient Plasticity. Int. J. Solids & Struct., Vol. 28, pp. 845-857.

Mühlhaus H.B., Vardoulakis I. (1987), The Thickness of Shear-Bands in Granular Materials. Géotechnique, Vol. 37, pp. 271-283.

Ohde J. (1939), Zur Theorie der Druckverteilung im Baugrund. Der Bauingenieur, Vol. 20, pp. 451-459.

Ortiz M., Simo J.C. (1986), An Analysis of a New Class Integration Algorithm for Elastoplastic Constitutive Relations. Int. J. Num. Meth. Eng., Vol 23 No. 3., pp. 353-366.

Owen D.R.J., Hinton E. (1980), Finite Elements in Plasticity; Theory and Practice. Pineridge Press, Swansea, U.K.

Pastor M, Peraire J., Zienkiewicz O.C. (1991), Adaptive Remeshing for Shear-Band Localization Problems. Ingen. Archiv, Vol. 61, pp. 30-39.

Pietruszczak S., Mroz Z. (1981), Finite Element Analysis of Deformation of Strain-Softening Materials. Int. J. Num. Meth. Eng., Vol. 17, pp. 327-334.

Pijaudier-Cabot G., Bazant Z.P. (1987), Nonlocal Damage Theory. ASCE J. Eng. Mech. 113, pp. 1512-1533.

Read H.E., Hegemier G.A. (1984), Strain Softening of Rock, Soil and Concrete - A Review Article. Mechanics of Materials, Vol. 3, pp. 271-294.

Riks E. (1979), An Incremental Approach to the Solution of Snapping and Buckling Problems. Int. J. Solids & Struct., Vol. 15, pp. 529-551.

Roscoe K.H. (1970), The Influence of Strains in Soil Mechanics. Géotechnique, Vol. 20, No. 2, pp. 129-170.

Roscoe K.H., Burland J.B. (1968), On the Generalized Stress-Strain Behaviour of "Wet" Clay. In: Engineering Plasticity, (eds. Heyman, Leckie). Cambridge University Press, pp. 535-609.

Roscoe K.H., Schofield A.N., Thurairajah A. (1965), Correspondence, Géotechnique, Vol. 15, pp. 127-130.

Rudnicki J.W., Rice J.R. (1975), Conditions for the Localization of Deformation in Pressure-Sensitive Dilatant Materials. J. Mech. Phys. Solids, Vol. 23, pp. 371-394.

Sandler I.S., Wright J.P. (1984), Summary of Strain-Softening. In: Theoretical Foundation for Large-Scale Computations of Nonlinear Material Behavior (ed. S. Nemat-Nasser). Proc. of DARPA-NSF workshop, Evanston, Ill, Oct. 1983. Martinus Nijhoff Publishers, The Netherlands, pp. 285-296.

Schmidt B. (1966), Earth Pressure at Rest Related to Stress History. Can. Geotech. J., Vol. 3, No. 4, pp. 239-242.

Schofield A., Wroth P. (1968), Critical State Soil Mechanics. McGraw-Hill, London.

Schreyer H.L., Chen Z. (1986), One-Dimensional Softening with Localization. J. Appl. Mech., Vol. 53, pp. 791-797.

Schultze E, Moussa A. (1961), Factors Affecting the Compressibility of Sand. Proc. V Int. Conf. Soil Mechanics and Foundation Engineering, Paris I, pp. 335-340.

Sloan S.W., Randolph W.F. (1982), Numerical Prediction of Collapse Loads Using Finite Element Methods. Int. J. Num. Anal. Meth. Geomech., Vol. 6, pp.47-76.

Sluys L.J. (1992), Wave Propagation, Localisation and Dispersion in Softening Solids. Dissertation. Delft University of Technology.

Smith I.M., Griffith D.V. (1982), Programming the Finite Element Method, Second Edition. John Wiley & Sons, Chisester, U.K.

Terzaghi K. (1925), Erdbaumechanik auf Bodenphysikalischer Grundlage. Franz Deuticke, Leipzig und Wien.

Thornton C. (1979), The Conditions for Failure of a Face-Centered Cubic Array of Uniform Rigid Spheres. Géotechnique, Vol. 29, No. 4, pp. 441-459.

Tillard D. (1992), Etude de la Rupture dans les Géomateriaux Cohésifs. Application à la Marne de Beaucaire. Dissertation. Université Joseph Fourier, Genoble.

Van Langen H., Vermeer P.A. (1990), Automatic Step Size Correction for Non-Associated Plasticity Problems. Int. J. Num. Meth. Eng., Vol. 29, pp. 579-598.

Van Langen H. (1991), Numerical Analysis of Soil-Structure Interaction. Dissertation. Delft University of Technology.

Van M.A., Venmans A.A.M., Janse E. (1991), Standaard Proevenserie op Veen en Klei van het Proefvak BRICOR. Report CO-318460/20, Delft Geotechnics - Department of Soil Structures, Delft.

Vardoulakis I. (1989), Shear-Banding and Liquefaction in Granular Materials on the Basis of a Cosserat Continuum Theory. Ingen. Archiv, Vol. 59, No. 2, pp. 106-114.

Vardoulakis I., Aifantis E.C. (1989), Gradient Dependent Dilatancy and its Implications in Shear-Banding and Liquefaction. Ingen. Archiv, Vol. 59, No. 3, pp. 197-208.

Vermeer P.A. (1979), A Modified Initial Strain Method for Plasticity Problems. In: Proc. III Int. Conf. Numerical Methods in Geomechanics. Balkema, Rotterdam, pp. 377-387.

Vermeer P.A (1980), Formulation and Analysis of Sand Deformation Problems. Dissertation. Delft University of Technology.

Vermeer P.A. (1990), The Orientation of Shear-Bands in Biaxial Tests. Géotechnique, Vol. 40, No. 2, pp. 223-236.

Vermeer P.A., De Borst R. (1984), Non-Associated Plasticity for Soils, Concrete and Rock. Heron, Vol. 29, No. 3.

Vermeer P.A., Van Langen H. (1989), Soil Collapse Computations with Finite Elements. Ingen. Archiv, Vol. 59, pp. 221-236

Vermeer P.A. (1991), PLAXIS - Finite Element Code for Soil and Rock Plasticity, Version 4.0, Balkema, Rotterdam.

Wroth C.P., Houlsby G.T. (1985), Soil Mechanics - Property Characterization and Analysis Procedures. In: Proc. XI Int. Conf. Soil Mechanics and Foundation Engineering. Balkema, Rotterdam. Vol. 1, pp. 1-55.

Wroth C.P., Zytynski M. (1978), Finite Element Computations Using an Elasto-Plastic Soil Model for Geotechnical Problems of Soft Clay. In: Proc. IX Int. Conf. Soil Mechanics and Foundation Engineering. MAA Publishing Company, Taipei. pp. 193-243.

Zbib H.M., Aifantis E.C. (1989), A Gradient Dependent Flow Theory of Plasticity: Application to Metal and Soil Instabilities. Appl. Mech. Reviews, Vol. 42, No. 11, pp. 295-304.

Zienkiewicz O.C. (1967), The Finite Element Method in Structural and Continuum Mechanics. McGraw-Hill, London, U.K.

Zienkiewicz O.C. (1971), The Finite Element Method in Engineering Science. McGraw-Hill, New York.

Zienkiewicz O.C., Zhu J.Z. (1987), A Simple Error Estimator and Adaptive Procedure for Practical Engineering Analysis. Int. J. Num. Meth. Eng., Vol. 24, pp. 337-357.

SYMBOLS AND SIGN CONVENTION

$\underline{\underline{B}}$: Strain interpolation matrix
c : Cohesion
C_u : Undrained shear-strength
$\underline{\underline{D}}^e$: Elastic material matrix representing Hooke's law
e : Void ratio
E : Young's modulus
f : Yield function
$\underline{f}$: Vector with discrete force components
g : Plastic potential function
h : Hardening / softening modulus
G : Shear modulus
$\underline{\underline{I}}$: Identity matrix
K : Bulk modulus
K_0 : Coefficient of lateral earth pressure
$\underline{\underline{K}}$: Global stiffness matrix
l : Internal length parameter
L : Length
L : Width of localization zone
m : Power in stress-dependent stiffness relation
M : Tangent of Critical State Line
$\underline{\underline{M}}$: Material stiffness matrix
$\underline{\underline{N}}$: Matrix with interpolation functions
OCR : Overconsolidation ratio
p : Isotropic stress or mean stress
Positive for pressure; negative for tension
p_c : Isotropic preconsolidation stress
Positive for pressure
POP : Pre overburden pressure
q : Equivalent shear stress
$\underline{s}$: Normalized stress direction vector
$\underline{t}$: Vector with boundary traction components
$\underline{u}$: Vector with displacement components
$\underline{v}$: Vector with discrete displacement components
w : Weighting function
W_c : Complementary strain energy function

α : Amplification factor in non-local strain measure
α : Drucker-Prager friction constant
β : Drucker-Prager dilation constant
γ : Soil weight
$\underline{\varepsilon}$: Vector with Cartesian strain components
Normal components positive for extension; negative for compression
ε_s : Equivalent shear strain
ε_v : Volumetric strain
Positive for compression; negative for extension
η : Softening scaling factor
κ : Swelling index
κ^* : Modified swelling index
λ : Plastic multiplier
λ : Compression index
λ^* : Modified compression index
ν : Poisson's ratio
$\underline{\sigma}$: Vector with Cartesian stress components
Normal components positive for tension; negative for pressure
σ_c : Vertical preconsolidation stress
Negative for pressure
φ : Friction angle
ψ : Dilation angle
ω : Numerical integration constant
$\omega = 0$: explicit ; $\omega = 1$: implicit

Only rectangular Cartesian coordinates are considered. A single underscore is used to identify a vector and a double underscore is used for matrices. A small dot above a symbol indicates the time-derivative (rate) of a particular quantity.

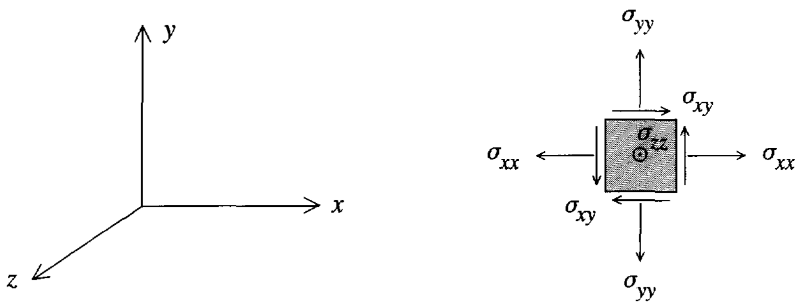

General three-dimensional coordinate system and sign convention for stresses:

SUMMARY IN DUTCH (Samenvatting)

Nederlandse titel: Materiaalmodellen voor Grond en Numerieke Analyse van Softening

Met de brede toepassing van computers worden geotechnische constructies steeds vaker door middel van eindige-elementenberekeningen geanalyseerd. Een wezenlijk onderdeel in deze benadering is het materiaalmodel, dat wil zeggen de toegepaste spanning-rek relatie die het grondgedrag weergeeft. In dit proefschrift worden enige materiaalmodellen beschreven en geëvalueerd met speciale aandacht voor de praktische toepasbaarheid. In aansluiting hierop worden verbeteringen voorgesteld.

Toepassing van conventionele materiaalmodellen met softeninggedrag, dat wil zeggen afname van de sterkte, leidt tot discretizatie-afhankelijke oplossingen en slechte convergentie van het evenwicht-iteratieproces. Door middel van regularizatiemethoden kunnen deze problemen worden verholpen. In dit proefschrift wordt een verbetering van een non-local regularizatiemethode voorgesteld en wordt de toepassing van de methode in eindige-elementenberekeningen beschreven.

Wanneer een grondconstructie in zeer geringe mate wordt ontlast en/of herbelast, zijn de daarbij optredende rekveranderingen nagenoeg reversibel. Een dergelijk gedrag kan worden beschreven door middel van elastische en pseudo-elastische modellen, welke in hoofdstuk 2 van dit proefschrift aan de orde komen. Voor een energetisch correcte beschrijving dienen elastische modellen te zijn gebaseerd op een zogenaamde strain-energy function, waarvan hier een tweetal wordt geanalyseerd. Voor klei en wellicht ook voor veen is het van belang dat de stijfheid evenredig is met het spanningsniveau, hetgeen in beide modellen onmogelijk is. Van één van deze modellen wordt daarom een uitbreiding voorgesteld, waarmee een stijfheid evenredig met het spanningsniveau wèl tot de mogelijkheden behoort.

Het optreden van irreversibele rekken kan worden beschreven door middel van elasto-plastische modellen. In hoofdstuk 3 wordt aan de hand van een tweetal bekende materiaalmodellen de basis van de plasticiteitstheorie beschreven. Speciale aandacht wordt besteed aan de formulering van vertices in het irreguliere Mohr-Coulomb vloeioppervlak. Daarnaast wordt getoond hoe het Drucker-Prager model voor plane strain situaties met dilatantie kan worden afgestemd op het Mohr-Coulomb bezwijkcriterium.

Naast het correct beschrijven van het bezwijkgedrag, is het van belang dat een materiaalmodel het gedrag in compressie correct weergeeft. Met name (quasi) ééndimensionale samendrukking is een in de praktijk veel voorkomende belastingsituatie. Hierbij treden er weliswaar irreversibele rekken op, maar van bezwijken is meestal geen sprake. Een dergelijk gedrag kan worden beschreven met een hardening model, waarvan Cam-Clay modellen een goed voorbeeld zijn. In hoofdstuk 4 wordt een beschrijving gegeven van het bekende Modified Cam-Clay model. Dit model heeft als nadeel dat de laterale gronddrukcoëfficiënt K_0 onjuist wordt weergegeven. In dit proefschrift wordt daarom een uitbreiding van het Modified Cam-Clay model geïntroduceerd, genaamd het Plaxis Cap model, welke bovengenoemd nadeel niet heeft. De relatie tussen K_0 en de modelparameters komt in dit hoofdstuk uiteraard uitvoerig aan de orde.

In hoofdstuk 5 wordt een algemene formulering gegeven van de eindige-elementenmethode voor deformatieberekeningen. Vanwege het niet-lineaire karakter van de modellen zijn er iteratieve procedures nodig om tot een evenwichtsysteem te komen. Het grootste deel van dit hoofdstuk behandelt de tijdsintegratie van spanningen en de numerieke implementatie van het in hoofdstuk 4 beschreven Plaxis Cap model. Voor het cap-hardening deel worden verschillende integratiemethoden geëvalueerd, waarbij de numerieke integratie op basis van de midpoint regel als beste wordt beoordeeld.

Het belang van hardening plasticiteit, zoals geformuleerd in Cam-Clay modellen, wordt geanalyseerd in hoofdstuk 6 aan de hand van een drietal berekeningen van praktijksituaties. Hierin worden de resultaten van berekeningen met het Plaxis Cap model vergeleken met die van eenvoudiger modellen. De conclusie van deze analyse is dat het gebruik van hardening modellen voordelen biedt in situaties waarbij er successievelijk compressie en distorsie optreedt, of in het geval van quasi ééndimensionale samendrukking waarbij horizontale deformaties een belangrijke rol spelen.

Hoofdstuk 7 geeft een beschrijving van enige materiaalmodellen met softening. Terwijl voor niet-softening modellen de eindige elementen oplossing bij toenemende verfijning van de discretizatie convergeert naar een eenduidige oplossing, leidt een conventioneel softeningmodel tot een oplossing die afhankelijk is van de discretizatie. Bovendien kunnen convergentieproblemen ontstaan tijdens het iteratieproces, waardoor het beoogde evenwichtsysteem moeizaam wordt bereikt. Dit laatste punt is in eerdere studies sterk onderbelicht, maar er wordt hier aangetoond dat dit een consequentie is van het gebruik van conventionele softeningmodellen. Voorbeelden illustreren dat resultaten van berekeningen met conventionele softeningmodellen onbetrouwbaar zijn.

Het probleem van de discretizatie-afhankelijkheid werd al in het midden van de jaren 70 geconstateerd, waarna diverse onderzoekers in de jaren 80 fundamentele oplossingen van dit probleem hebben voorgesteld, de zogenaamde regularizatiemethoden. Eén van deze methoden is de non-local theorie, waaraan een belangrijke impuls is gegeven door Bazant. In hoofdstuk 8 wordt echter aangetoond dat de bestaande non-local methode niet effectief is, en er wordt een nieuwe formulering voorgesteld. Om een goed inzicht te verkrijgen in de werking van de methode alsmede de invloed van non-local parameters, wordt er in hoofdstuk 8 uitgegaan van een puur ééndimensionale spanning-rek relatie met lineaire softening. De nieuwe formulering leidt tot een analytische oplossing voor het lokaal bezwijken van een trekstaaf.

In hoofdstuk 9 wordt beschreven hoe de non-local methode kan worden uitgebreid naar algemene toepassing in driedimensionale softeningmodellen. Na de formulering van een robuuste eindige-elementen implementatie, wordt er aangetoond dat, bij toepassing van deze methode op de in hoofdstuk 7 beschreven softening modellen, de genoemde discretizatie- en convergentieproblemen zich niet meer voordoen.

De conclusies van het onderzoek worden tenslotte weergegeven in hoofdstuk 10.

CURRICULUM VITAE

Naam	Ronald Bastiaan Johan Brinkgreve
Geboren	9 december 1965 te Doetinchem
sept. 1978 - juli 1984	Chr. Scholengemeenschap Blaise Pascal te Spijkenisse, afgesloten met het VWO diploma.
sept. 1984 - aug. 1989	Studie Civiele Techniek aan de Technische Universiteit Delft. Afstudeerrichting: Geotechniek. Afstudeerprojekt: Stabiliteitsanalyse van Bouwputten met E.E.M. Model.
aug. 1989 - feb. 1990	Medewerker aan de Technische Universiteit Delft, Sectie Geotechniek.
maart 1990 - feb. 1994	Onderzoeker-In-Opleiding aan de Technische Universiteit Delft, Sectie Geotechniek. Onderzoeksprojekt DCT92.1870 van de Stichting voor de Technische Wetenschappen (STW) i.s.m. Rijkswaterstaat (DWW) en Shell Research (KSEPL).